A Novel Method for the Continuous Separation of Microorganisms based on Electrical Properties

by

Michael D. Vahey
Bachelor of Science, Electrical and Computer Engineering
Carnegie Mellon University, 2004

Submitted to the Department of Electrical Engineering and Computer Science
in Partial Fulfillment of the Requirements for the Degree of

Master of Science
at the
Massachusetts Institute of Technology

January 20, 2006
[February 2006]

Author: _____
Department of Electrical Engineering and Computer Science
January 20, 2006

Certified by: _____
Joel Voldman
Thesis Supervisor

Accepted by: _____
Arthur C. Smith
Chairman, Department Committee on Graduate Theses

A Novel Method for the Continuous Separation of Microorganisms based on Electrical Properties

By

Michael D. Vahey

Submitted to the
Department of Electrical Engineering and Computer Science

January 20, 2006

in Partial Fulfillment of the Requirements for the Degree of
Master of Science

ABSTRACT

Increased throughput in the techniques used to engineer new metabolic pathways in unicellular organisms demands similarly high throughput tools for measuring the effects of these pathways on phenotype. For example, the metabolic engineer is often faced with the challenge of selecting the one genomic perturbation that produces a desired result out of tens of thousands of possibilities. This thesis proposes a separation method – iso-dielectric separation, or IDS – which separates microorganisms continuously based on their dielectric properties. This technology would enable high throughput screening of cells based upon electrically distinguishable phenotypes.

Iso-dielectric separation uses dielectrophoresis (DEP) and media with spatially varying conductivity to separate cells based upon their effective conductivity. Our target application is the separation of *Escherichia coli* based upon the amount of the intracellular polymer poly(hydroxybutyrate) that each cell contains. This thesis discusses the modeling, design, fabrication, and testing of an IDS device.

Thesis Supervisor: Joel Voldman
Title: NBX Assistant Professor of Electrical Engineering and Computer Science

ACKNOWLEDGEMENTS

Over the 18 months of this project's existence, I have been very fortunate to have the technical and emotional support of many very talented and generous people. First on this list is my advisor, Prof. Joel Voldman, whom I would like to thank on a number of different levels; for assembling an outstanding group of people, and letting me be a part of it; for always being available for advice and to talk things through; and for letting me play around with his clever ideas. I cannot imagine a more enjoyable project to work on, nor a nicer environment in which to work on it; I have Joel to thank for both.

This project would be enormously weaker were it not for the help of my fellow students, as well. From a technical standpoint, Salil Desai and Keith Tyo in particular have been enormously helpful. Without these two gentlemen and the beloved test particles they have graced me with, this thesis would be a lot shorter, and more than commensurately weaker. Also, thank you to the support staff of the Microsystems Technology Laboratory, especially Dave Terry and Paul Tierney, whose expertise got me through all of the fabrication steps in this thesis.

Of equally great value to me are all of the less explicit contributions each member of the Voldman group has made. I want to extend particular gratitude towards Nitzan Gadish, whose intelligence, helpfulness, humor, and general pleasantness made her a popular target for my inane ramblings. That she always – *always* - responded to my questions, comments, and distractions with the same qualities that brought them upon her in the first place is nothing less than heroic, and I am very grateful. Thanks, also, to the people who remain stuck with me; Salil, for (besides the vesicles) his fond memories of Pittsburgh, and his willingness to undertake things that I find terrifying; Katya, for her boundless enthusiasm, and for never backing down in an argument; Lily, for her infinite patience and for being a great resource on everything; Brian, for constantly raising the bar with his humor and hard work; Hsu-Yi, my contemporary in the group, for solidarity through all the trials of first-year graduate life; Adam, for his shared enthusiasm for conservation equations and for not laughing at my inability to run a marathon; and to all of the newest members of the group - Nick, Joseph, and Pat - whom I have enjoyed getting to know, and who – I am happy to say, though the feeling may not be mutual - are stuck with me for a particularly long time.

I would also like to thank all of my old friends and past mentors, for always seeing to it that I got where I needed to go, and had a pleasant time along the way. Finally, I thank my family, especially my parents, David and Linda, and my brother, Brian. It has been their unwavering support through the highs and lows of the past 23 years for which I owe the most.

TABLE OF CONTENTS

LIST OF FIGURES

LIST OF TABLES

NOMENCLATURE

Symbol	Description	Symbol	Description
σ	Electrical conductivity	c_i	Molar concentration (species i)
ε	Electrical permittivity	D_i	MolecularDiffusivity (species i)
R	Particle Radius	U	Mean fluid velocity
ω	Angular frequency	Pe	Peclet number
$\mathbf{p}$	Dipole moment	P	Pressure
$\mathbf{E}$	Electric field	μ	Fluid viscosity
$\underline{CM}$	Clausius-Mossotti Factor	φ	Electric potential
K_0	Re$\{CM\}$ at the IDP	V_0	Applied voltage
$\mathbf{e}_i$	Unit vector in the i^{th} direction	ρ_m	Mass density
$\mathbf{F}$	Force	ρ_e	Charge density
$\mathbf{J}$	Current Density	κ	Thermal conductivity
$\mathbf{v}$	Velocity	$\hat{c}_p$	Heat capacity per unit mass at constant pressure
Q	Volumetric flowrate	α	Thermal diffusivity
w	Chamber width	τ_e	Charge relaxation time
h	Chamber height	$\mathbf{g}$	Acceleration due to gravity
l	Chamber length	Re	Reynolds number
d	Electrode Spacing	T	Temperature
θ	Angle of electrodes with respect to channel axis	δ	Debye length
u_i	Electrical mobility (species i)	ζ	Zeta-Potential
z_i	Valence (species i)		

Note that this listing includes only the most frequently used symbols throughout this thesis. Symbols which are used only once are identified in the text. In general, bold face symbols denote vectors or tensors, while italic symbols denote scalars. Underlined symbols represent complex quantities; '~' on top of a symbol indicates that that quantity has been made dimensionless.

Chapter 1: Introduction

Many of the challenges faced in both fundamental biology and biotechnology are attributable to two characteristics common to all biological systems: the complexity of any individual organism, and the high variability between these individuals within a population. The former necessitates the collection of large quantities of data, while the latter obscures the relevant information within this data. This difficulty is exemplified in the area of genetic engineering, where combinatorial approaches are often employed in the effort of mapping genotype to phenotype [1]. In order to make a sufficiently large number of genomic perturbations practical, it is essential to have a high throughput means of not only introducing the perturbations, but also of quantifying their results. This research presents the modeling, design, fabrication, and testing of a device for performing the high throughput screens of microorganisms that would further enable the use of combinatorial approaches to genetic modification. In particular, we will emphasize the separation of the bacterial cell *Escherichia Coli* based upon production of intracellular polymer. In this chapter, we discuss the fundamental concepts underlying this method, labeled iso-dielectric separation (IDS), and our application to biomolecule production in *E. coli*, as well as where it fits in a larger context of existing methods. We conclude with an overview of the architecture we have selected for this first implementation of an IDS device.

1.1 Target Application and the Electrical Properties of Cells

The process by which the biologist seeks to map genetic information to phenotype is called genetic screening. Cell-based genetic screens can be roughly decomposed into three steps: alteration of the cell's genetic program, observation of the subsequent effects on phenotype, and isolation of those cells with phenotypic expressions of interest. This discussion and the work that follows focuses on the latter two steps: observation and isolation. The phenotypic expression we are interested in is the production of the polymer poly(hydroxybutyrate) (PHB) by *E. coli*. PHB is a subset of the poly-hydroxyalkanoates, plastics which are of interest for being biosynthetic, biocompatible, and biodegradable [2, 3]. The idea central to this thesis is that, since biomolecules within a cell tend to be more electrically insulating than the cytosol they displace, increased concentration of these molecules inside a cell will tend to decrease the overall electrical conductivity of that cell [4, 5]. This is essentially the starting point for the work described in this thesis. Given the efforts of our collaborators, Greg Stephanopolous and Keith Tyo in the department of Chemical Engineering, towards altering the genetic program of *E. coli* to create PHB, we pursue a method for observing and isolating the highest producers, based on electrical conductivity.

From an electrical perspective, the enormous chemical and biological complexity of a cell matters only to the extent that it can support the storage and motion of charge. This represents a mixed blessing to anyone interested in the electrical manipulation of cells, since substantially different biological systems may be nearly indistinguishable electrically. With iso-dielectric separation, we seek to exploit this implicit reductionism of electrical methods to separate cells generically, based on their production of generically insulating biomolecules. To understand our hypothesis, a brief discussion of the electrical properties of cells (or any heterogeneous system) is appropriate.

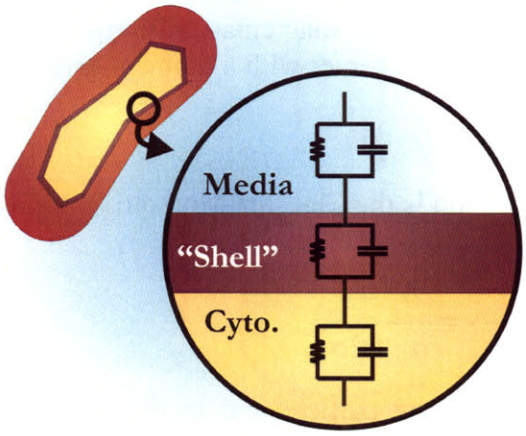

Figure 1-1: Lumped electrical model of a cell.

The many-layered, complex biological structure has been reduced to two homogeneous effective layers; one for the outer-most layers, and one for the cytoplasm.

Derivation of the electrical properties of a cell from first principles is a prohibitively difficult task. However, it is possible to homogenize the complex structure of the cell into different layers, the properties of which may then be determined experimentally [5, 6]. A very simple model for a bacterial cell obtained in this way is shown schematically in Figure 1-1. Here, we have lumped all of the outer-most structure into a single electrical layer (which we will call the "shell"), which surrounds the homogenized cytoplasm. Associated with the shell layer is an equivalent resistor-capacitor network. At low frequencies, where the shell capacitance looks like an open circuit, the equivalent resistance of the cell is given by combining the resistances of the shell and cytoplasm. At high frequencies, however, the impedance of the shell capacitance becomes very small, leaving only the cytoplasm to support a potential drop. If one were to calculate the electrical properties of this cell using a high frequency signal, they would measure in this case only the properties of the cytoplasm – either its conductivity, its permittivity, or a frequency-weighted combination of the two. The addition of some new component to the cytoplasm – PHB, for example – might be expected to alter what we measure for the cell's properties, provided that the measurement is taken at an appropriate frequency. We will discuss in greater detail what these frequencies are and how changes in a cell's phenotype affect its lumped electrical properties later. For the time being, this example serves only to illustrate what we mean by the electrical properties of a cell, and how we can use frequency to control what part of the cell we are probing.

1.2 Dielectrophoresis

Since we wish to select cells according to their dielectric properties, it is essential that we understand how particles behave in the presence of electrical fields. Specifically, we are interested in the physical phenomena collectively known as dielectrophoresis, or DEP. DEP has been used extensively as a means of manipulating cells by our group [7-9] and others [10, 11], and refers to the force exerted on the induced dipole moment of a polarizable particle in a non-uniform electric field. In this work, we will restrict our interest more specifically to spatially non-uniform electric fields. The relevant features of DEP, as related to IDS in particular and particle separations in general, can be illustrated by the simple example of a spherical particle placed in a uniform applied electric field (Figure 1-2). For generality, the field is assumed to be sinusoidal, with frequency ω. If the electrical properties of the particle are different from those of the media, the field will be distorted by the presence of the particle. This local change in the shape of the electric field is caused by charge induced at the interface between the media and the

sphere, and is aligned along the axis of the applied electric field. Solving for the electric field both inside and outside the particle reveals that it is mathematically equivalent to the field produced by an infinite dipole located at the sphere's center with a moment given by:

$$\mathbf{p} = 4\pi\varepsilon_m R^3 \,\mathrm{Re}\left\{\underline{CM}(\omega)\right\}\mathbf{E}_0 \tag{1-1}$$

Of primary importance to iso-dielectric separation is the Clausius-Mossotti factor, denoted as $\underline{CM}(\omega)$ and given by:

$$\underline{CM}(\omega) = \frac{\underline{\varepsilon}_p - \underline{\varepsilon}_m}{\underline{\varepsilon}_p + 2\underline{\varepsilon}_m} \cong \frac{\sigma_p - \sigma_m}{\sigma_p + 2\sigma_m} \tag{1-2}$$

where $\underline{\varepsilon}_{p,m}$ denote the complex permittivity of the particle and media, respectively, and are roughly equal to the conductivities at sufficiently low frequencies. This factor, the real part of which is bounded by -0.5 and 1.0, describes the electrical dependence of the particle's polarizability. When the electrical properties of the media and particle are equal, the particle is no longer polarized by an applied field.

When the applied field is uniform, as we have been considering so far, the polarization produces no net force. If, however, a small non-uniformity is introduced to the electric field, the dipole force to first-order becomes:

$$\mathbf{F} = \mathbf{p}\cdot\nabla\mathbf{E} \approx 4\pi\varepsilon_m R^3 \,\mathrm{Re}\left\{\underline{CM}(\omega)\right\}\mathbf{E}\cdot\nabla\mathbf{E} \tag{1-3}$$

$$\mathbf{F} = \mathbf{p}\cdot\nabla\mathbf{E} \approx 2\pi\varepsilon_m R^3 \,\mathrm{Re}\left\{\underline{CM}(\omega)\right\}\nabla E^2 \tag{1-4}$$

In going from (1-3) to (1-4), we have used the fact that the electric field is irrotational. When the CM factor vanishes, the DEP force will vanish as well, regardless of other parameters. It is this conductivity dependence of the DEP force that we exploit to perform separations.

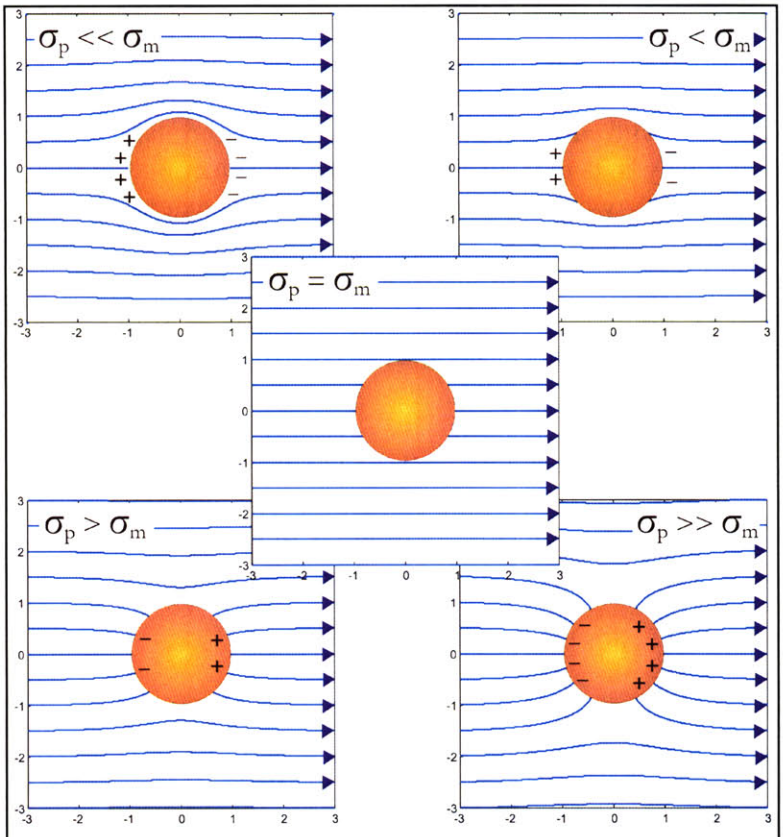

Figure 1-2: Polarization of a spherical particle.

A uniform applied electric field (blue lines) is disturbed by the presence of a particle with electrical properties different from those of the media. The change in electric field results from the accumulation of charge at the interface between the particle and the external media. For a relatively insulating particle, charge is supplied by the media, and the dipole moment is aligned *opposite* the applied (undisturbed) field. A relatively insulating particle provides charge, and has a dipole moment aligned with the applied field.

1.3 DEP Force and Sensitivities

The efficacy of DEP as a means of separating and trapping particles is perhaps now clear. Not only is the *magnitude* of the force dependent on both the particle's size (R^3) and dielectric properties ($\mathrm{Re}\{CM\}$), but it is possible to change the *direction* of the force as well, through the dielectric properties of the media. The dependence of polarizability on both size and electrical properties can provide challenges, however, when one is interested in performing separations which are dependent upon dielectric properties alone, as is the case in this project. If a population of particles is perfectly monodisperse, separation based on conductivity is trivial; subjecting particles to the same DEP force for the same amount of time will displace those with the highest (magnitude) CM factor the greatest distance. In populations containing a distribution of both sizes and electrical properties, the cubic dependence on size will almost always overwhelm the electrical contribution to the DEP force. Conductivity-specific separations must therefore cancel out, to the greatest possible extent, the size dependence of the DEP force.

One way to consider the relative sensitivity of the DEP force to size and electrical properties is to calculate it explicitly from equation (1-4). The change in radius, ΔR, necessary to produce a change in the DEP force identical to that produced by a given increment in particle conductivity, $\Delta\sigma_p$, is given by:

$$\Delta R = R\left[\frac{\sigma_m}{(\sigma_p + 2\sigma_m)(\sigma_p - \sigma_m)}\right]\Delta\sigma_p \qquad \textbf{(1-5)}$$

A straightforward but important conclusion can be drawn from this expression. Since insensitivity to size corresponds to large ΔR, we see that when the particle conductivity very nearly matches that of the media, the DEP force becomes much more sensitive to conductivity than to size. If we have two particles with arbitrarily different sizes and two distinct conductivities, we can separate them in a way that is insensitive to size by selecting the media conductivity to exactly match that of one of the two particle conductivities. By extension, if the particles have many different conductivities, insensitivity to size will require correspondingly many different media conductivities, as well as a means of assuring that each particle is brought in the vicinity of its matching conductivity. In IDS, a conductivity gradient is used to enhance sensitivity to the particles' electrical properties at the expense of sensitivity to size.

1.4 Existing Methods

Of course, DEP is not the only way to separate cells. Given the importance of separations as a fundamental operation in biology, it is not surprising that many separation methods have been developed for widely varying applications. In order to parse this enormous field of research, we limit discussion to the techniques, only some of which use DEP, most relevant to the problem at hand.

1.4.1 Chromatography

The most common technique for screening intracellular polymers is chromatography [12]. This involves the dissolution of a sample, collected from lysed cells, in a gas or liquid (mobile) phase, which is then passed through a stationary phase in which the components of the sample have differing solubilities. Two common variations are gas chromatography (G.C.) and High Performance Liquid Chromatography (H.P.L.C.). While G.C. and H.P.L.C. differ in choice of phases and instrumentation, the physical principle by which they operate is the same; because the components spend different amounts of time in the mobile and stationary phases, the rate at which they migrate will differ. In this way, molecules can be separated and quantified with very high sensitivities.

Chromatography, however, has some drawbacks. Since it is essentially a macro-scale technique, it requires large sample volumes (often tens of milliliters) and, in cases where the molecule of interest is internal to the cell, it requires the destruction of those cells. The requirement of large volumes, in addition to the time and expense it incurs, precludes gathering information regarding variability within a population; data for biomolecule production is inherently averaged over tens of millions of cells. A second drawback of chromatography is that it is specific to the class of molecule one is interested in. Changing the biomolecule generally means changing the assay. If one is interested in quantifying a cell's production of any generic biomolecule, a separation method that is similarly generic would simplify the development of assays.

1.4.2 Flow Cytometry

An alternate method for performing genetic screens based on phenotype is flow cytometry. In particular, we are interested in fluorescence-activated cell sorting, or FACS [13]. In this method, cells are labeled by a fluorescent stain and interrogated by a laser. If the laser is at a wavelength which causes the stain to emit light, this light can be collected to characterize each cell, and the cells may be sorted accordingly. Our collaborators have had considerable

success in screening *E. coli* for production of PHB in this way. Using a fluorescent probe (Nile Red) which binds preferentially to PHB, they are able to sort cells based on intensity of the light emitted by this probe, and thus PHB production. Unlike chromatography, FACS is non-destructive and continuous. However, it is still assay specific, in the sense that a new probe is required each time the biomolecule one is screening for changes. Furthermore, FACS is a serial process, sorting one cell at a time at rates of up to ~10^4-10^5 cells per second.

1.4.3 Gradient Separation Methods

In cases where the limitations of G.C. or H.P.L.C. are prohibitive, gradient separation methods are often enabling. These are broadly defined as techniques where a force depending on some property of a particle relative to that of its surroundings is combined with media in which the relevant property varies [14]. The gradients in media properties produce a force gradient which will be different for particles with different properties. If this force gradient is established in such a way that particles are directed to the point in which the force acting on them vanishes, a *stable* separation of the particles based upon the relevant property may be performed.

One example of a gradient separation method is density-gradient centrifugation (DGC) [15]. Here, the force and property exploited are gravity and density, respectively. If particles are suspended in a density gradient that increases in the direction of the gravitational field, the particles will migrate to the point in the gradient where their density matches that of their surroundings. In this case, the requirement for a stable separation is that the density gradient be collinear with the gravitational field, and that the range of the density gradient covers the densities of the particles of interest. A second gradient separation method is iso-electric focusing (IEF). The mode of operation is analogous to DGC, with the slight change that the property of interest (electrophoretic mobility, as controlled by surface charge) is now a complicated function of the media properties (pH, in IEF), rather than being identical to it, as was the case for density. The gravitational field is replaced with an electric field, and the gradient directed such that the particle of interest are directed to the pH at which their electrophoretic mobility vanishes. Neither DGC nor IEF are well-suited to the separation of *E. coli* based on biomolecule production; they are of interest not for their applicability to the problem at hand, but for the implications that they illustrate for generic gradient methods. Specifically, the common feature of these separation methods is the superposition of a media-dependent force on a media gradient. The exact dependence of the force on media/particle properties may be trivial (as in DGC) or quite complicated (as in IEF). We also see that the orientation of the field and gradient responsible for the separation determine whether or not the separation will be stable.

1.4.4 DEP Field-Flow Fractionation

A final separation method that I will discuss in some detail is dielectrophoretic field-flow fractionation (DEP-FFF) [16]. Traditionally, most DEP separation methods have been binary, selecting conditions under which one type of particle is attracted to electric field maxima (p-DEP), while others are repelled (n-DEP). DEP-FFF offers a significant improvement over these methods in its ability to separate multiple (two or more) subpopulations from a mixed sample of cells. In DEP-FFF, the sample of cells, confined to a narrow band, is injected into a microfluidic chamber with interdigitated electrodes along the bottom. The media and frequency of excitation of the electrodes is chosen so that the cells will be repelled from the chamber floor, via n-DEP. This DEP repulsion balances with the gravitational force at some equilibrium height, which will

generally depend on a particular cell's size, density, and polarizability. Once the cells have reached this static equilibrium, pressure-driven flow through the chamber is initiated. The fluid velocity varies with height above the electrodes so that particles which settle further from the electrodes (but below the half-height of the chamber) are carried more rapidly to the channel's outlet, where they may be collected.

In DEP-FFF, the property that is being selected for is a combination of density and polarizability, while the media gradient can be thought of as velocity. Just as in other gradient methods, the force (hydrodynamic drag) is a function of the media/particle properties, where we are generalizing media properties to include the rate at which the media moves. Where DEP-FFF differs from IEF and GDC follows from this generalization of media gradients to include dynamic properties; instead of separating cells *spatially* (i.e. at some point along a gradient of material properties), the separation is performed in *time*, with the consequence that the cells never reach an equilibrium point and sample collection must be carefully timed. This precludes the use of DEP-FFF, as described here, as a continuous separation method. A second distinction between DEP-FFF and GDC / IEF is less fundamental and more practical; while traditional gradient separation methods do not depend on the initial locations of the cells within the gradient, DEP-FFF does; cells must be confined to a narrow region with respect to the length of the channel, else their initial distribution will overwhelm any changes introduced by the flow fractionation. This, combined with effects of Brownian motion on the settling of small particles, makes DEP-FFF an experimentally intensive method for some applications.

We envision iso-dielectric separation as a separation method capable of overcoming some of the limitations of the existing techniques presented here. In keeping with this objective, any device for IDS should be continuous and non-destructive. To achieve this, we borrow the use of DEP from existing methods, but replace the dynamic velocity gradient of DEP-FFF with a gradient in electrical conductivity, a material property upon which the DEP force depends directly. A conductivity gradient across the width of a channel, combined with spatially non-uniform electric fields, could propel cells via the DEP force to a point at which their conductivity matches that of the media, and the propelling force vanishes. This, like GDC and IEF, would result in spatial - and thus continuous – separations. Building the analogy to IEF, we refer to this point as the iso-dielectric point, or IDP. In contrast to chromatography, IDS should also be capable of quantifying production on the level of single cells, as opposed to averages over large populations. Since conductivity is deterministically related to both IDP and intracellular biomolecule concentration, we can quantify biomolecule production by simply observing where cells are collected. This provides data for not only the average production of a population, but the variability of production as well. With this definition of IDS – continuous-flow, non-destructive separation of cells in a conductivity gradient with the potential for quantitative analysis at the level of individual cells – we proceed to consider the implementation of such a device.

1.5 General Constraints on Iso-Dielectric Separation

Our IDS device relies on the superposition of gradients in electric field intensity and fluid conductivity, thus requiring the integration of electrical and microfluidic structures. In choosing an architecture for IDS, we must assure that these two domains coexist functionally. At a minimum, we must be able to first create a conductivity gradient that is stable for the duration of the separation, and second, create an electric field that will direct all particles to the point in this gradient where the DEP force vanishes. The method by which we approach each of these tasks

is determined, in large part, by the characteristics of our IDS device, and its position within the broader field of separation methods.

Methods for creating concentration gradients in microfluidic channels are well-established. We will limit discussion to two classes of gradients: those stabilized by convection, and those made psuedosteady by exploiting disparate timescales for diffusive transport. Convection-driven gradients are maintained by the continual introduction of fresh solute concentrations carried by parallel laminar flow-streams into a channel, where the solute may then inter-diffuse. Psuedosteady gradients are often present in systems with two disparate length or volume scales, as exemplified by the canonical problem of diffusion across a thin membrane separating two well-mixed baths containing different concentrations of some chemical species. The implications of these two approaches on the features of an IDS device are substantial; since the particles to be separated are inextricable from the gradient in which they are suspended, the choice between convection-driven and psuedosteady gradients essentially amounts to the choice between IDS as a continuous or batch separation method.

Since we have decided to approach IDS as a continuous process, it follows that particles will be subjected to forces other than DEP – namely, hydrodynamic drag from the flow necessary to stabilize the conductivity gradient. With this as the case, IDS will never be absolutely insensitive to size: rather than settling at the point in the conductivity gradient where the particle's dielectric properties match those of the media, the particles will only approach this point to the extent that the imposed drag will allow. The sensitivity of the separation to electrical properties only is thus contingent on how minimal the effects of fluidic drag are. Alternatively, if we choose to implement IDS as a batch method, injecting cells into a convection-free, psuedosteady gradient, and allowing them arbitrarily long to converge on their respective IDPs, we will have excellent sensitivity, but potentially far lower throughput. It is within this context – the conflict between throughput and sensitivity - that the decision of how to establish the conductivity gradient is framed. Because this project was originally conceived to fill a niche similar to that in which DEP-FFF and HPLC have had much success, and to distinguish IDS from these existing technologies, we decided to pursue a continuous implementation of IDS. In the work described here, we restrict ourselves to a continuous approach, while noting that a batch implementation of IDS holds significant promise for future work.

Having considered the tradeoffs inherent in using convection-driven gradients, we shift our attention to the general electrical requirements of the system. We begin by considering the imposition of a current across a chamber of variable conductivity. This situation could be produced, for example, in a microfluidic T-mixer, in which the conductivity has been allowed to diffusive across the channel's width for some time, and is similar to geometries considered extensively in the literature [17-19]. Assuming, for simplicity, that the applied voltage is DC, conservation of charge requires:

$$\nabla \cdot \mathbf{J} = \mathbf{0} \quad \rightarrow \quad \frac{d}{dx}\left[\sigma(x)E_x(x)\right] = 0 \qquad \textbf{(1-6)}$$

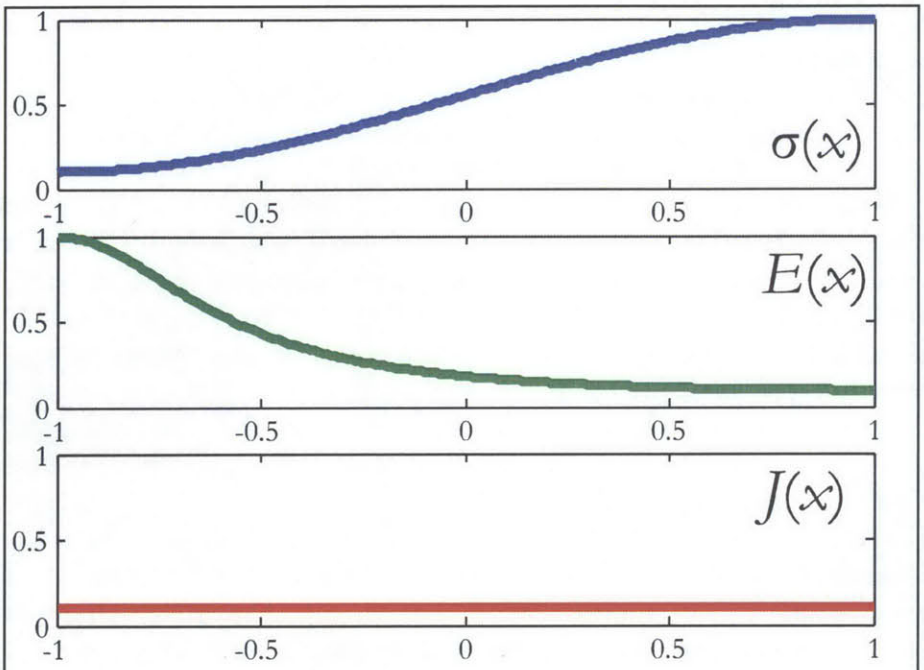

Figure 1-3: Coupling of electric field with conductivity

Conductivity, electric field, and current density typical for a T-mixer with an imposed transverse current density, in which the laminar streams have had several characteristic times to diffuse.

From this relationship, it is straightforward to show that, regardless of the precise form of the conductivity, $\sigma(x)$, the magnitude of the electric field will vary in the direction opposite that in which the conductivity varies. Figure 1-3 shows the conductivity, electric field (magnitude), and current density that would result from this configuration. Suppose now that particles of some conductivity within the range spanned by the media are injected into this chamber. A particle that is less conductive than its surroundings (subjected to n-DEP) would move towards the field minima and thus to higher conductivity, while a more conductive particle would be forced to regions of even lower media conductivity. Analogous to DGC in a density gradient oriented opposite the gravitational field, this would confound any attempt at IDS: all particles would diverge to the sides of the channel. From this, we conclude that the field and conductivity gradients must be collinear. Since this condition is contrary to what will happen naturally in the presence of non-uniform conductivity, it is necessary to shape the field geometrically.

Many different ways of shaping electric fields have been modeled and implemented in the literature, precluding a comprehensive discussion. Instead, we superficially divide these approaches into the two general categories considered most relevant for this project. The first technique creates spatially varying fields and a subsequent DEP force through the use of specially designed insulating boundaries, and is commonly referred to as insulator-based dielectrophoresis (iDEP) [20]. This approach essentially involves applying a potential across a path of variable shape or cross-section, comprised of an electrically insulating material. In order for charge to be conserved, the electric field must become stronger in regions where the conduction path is more highly constricted. A decreasing channel cross-section can be designed to compensate for increasing media conductivity; had the plots of Figure 1-3 used a channel with a height that decreased in the direction opposite that of the conductivity, it would be possible to achieve collinear field and conductivity gradients. While this allows for precise control of the magnitude and shape of field gradients, it has some significant drawbacks. First, a chamber with

variable cross-section will shape not only the electric field, but the velocity field as well. Since the separation is based on the variability of the DEP force with position, a spatially varying drag force would undermine IDS to an extent. A second drawback of shaping fields with insulating boundaries is that, in general, it requires electrodes separated by a distance comparable to the total size of the system. To achieve strong DEP forces, the electrodes must therefore be driven at very high (~kV) potentials. The instrumentation required to drive such a system is limited to very low frequencies, and thus would be restricted to probing only the outermost layers of a cell.

Rather than the boundaries, we choose to pattern the electrodes themselves to achieve high field gradients that are *locally* collinear with conductivity. An important caveat to the previous discussion of the need for collinear field and conductivity gradients is that they need only be collinear in the regions of the channel where the particles will be. Symmetric electrodes confined to a small region of the channel will see locally constant conductivity, and will produce a correspondingly symmetric region of electric field intensity, one half of which will be collinear with conductivity. If particles are confined to this half of the electrode structure, the anti-collinearity of the other half will not affect the separation. We therefore envision a DEP barrier, arranged at an angle with respect to the flow in which the particles to be separated are carried. If the particles are originally confined to relatively high conductivities, the confined electrodes will serve as an n-DEP barrier. The DEP force, resolved with drag from the fluid, will induce a transverse component to the particle's velocity. In this way, DEP can be used to carry particles towards decreasing conductivities. If the range for the conductivity gradient is chosen appropriately, it can be guaranteed that, at some point along the channel's width drag will overcome the compromised DEP barrier, and the particles will flow downstream unobstructed. This is our general architecture for IDS: a convection-stabilized conductivity gradient with particles confined to one side, combined with a DEP barrier across the channel's diagonal.

It is worth mentioning that this implementation of IDS is not perfectly analogous to DGC and IEF, the two gradient separation methods considered earlier. For these methods, it was found that the final position of a cell within the media gradient was independent of where the cell was initialized. In contrast, IDS requires that all particles be initialized at one extreme of the conductivity gradient, as a consequence of our decision to use only partially collinear field and conductivity gradients. In this sense, IDS may be considered more similar to DEP-FFF, where particles are initialized in a precise location prior to performing the separation. Of course, particles in IDS are localized along the transverse dimension, as opposed to the axial dimension, mitigating this challenge considerably. A more direct analog to IEF (iso-dielectric *focusing*, perhaps) could be implemented by the smoothly varying field gradients characteristic of iDEP architectures.

1.6 Device Overview

Figure 1-4 shows a schematic of the device. Solutions of two different conductivities are prepared and injected into the device. In one of the two solutions, either high or low conductivity, depending upon whether the separation is to use n-DEP or p-DEP, the particles to be separated are added. The two conductivities are split, mixed, and recombined in a diffusive mixer, creating a stepwise conductivity gradient prior to their introduction into the rectangular separation chamber. One or more pairs of electrodes arranged at the bottom of this chamber are used to exert a DEP force on the particles as they flow downstream. Drag and DEP forces combine to push the particles along the electrode barrier, in the direction of changing conductivity. Because the strength of the DEP barrier depends on the relative conductivities of

the particle and its environment, operating conditions can be chosen so that the barrier becomes sufficiently weak at some point along the chamber's width. For particles with different conductivities, the point at which the barrier is compromised will be different. Collecting particles from outlets sampling different intervals along the channel's width will produce populations that have been sorted according to their electrical properties.

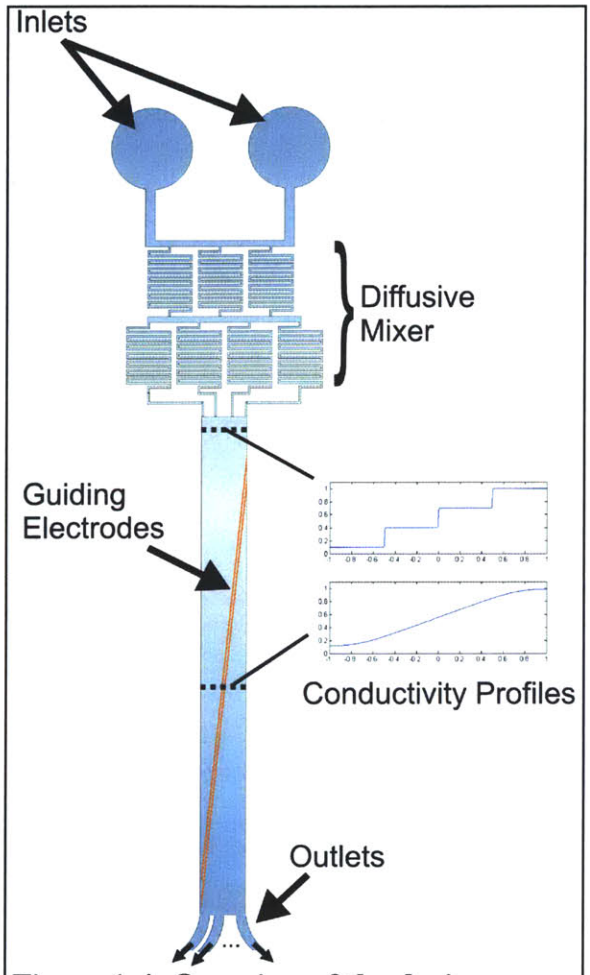

Figure 1-4: Overview of the device

Different media conductivities are introduced into a diffusive mixer which produces a smoothly varying gradient across the channel's width. Guiding electrodes steer particles along the conductivity gradient until the iso-dielectric point (IDP) is reached. Particles with different IDPs are then collected at different outlets.

1.7 Thesis Overview

The successful implementation of a device for IDS is contingent on satisfying several competing constraints. Accordingly, a large portion of this project has focused on understanding the physical behavior of the device from the perspectives of electrostatics and heat, mass, and momentum transport. In chapter 2, we discuss our approach to modeling in all of the relevant physical domains, including coupling, and the implications this modeling held for the device's design. Chapter 3 follows with a discussion of the implementation of the design, with an emphasis on the selection of materials and a process flow for microfabrication. The focus of chapter 4 is the design of schemes for packaging the device, selection of particles for use in design evaluation, and the development of protocols for experiments and data acquisition. Chapter 5 presents experimental results, and chapter 6 concludes the thesis with a discussion of contributions and possible directions for future work.

Chapter 2: Design and modeling

Iso-dielectric separation uses electric fields and non-homogeneous media conductivity to produce a force gradient in which particles are separated. The ultimate performance of the device will therefore depend on a broad range of physical phenomena. In order to effectively design the device, we need comprehensive models for all of these phenomena and the complex ways in which they couple together. We approach this problem by first considering each of the physical domains in isolation. This provides a first-order description for how the device will work. We then consider how different aspects of the model interact, to obtain higher-order corrections to the overall system description.

The design process can be decomposed as follows. Given the general device architecture outlined in chapter 1, we solve for the relevant field variables: electric potential, conductivity, and fluid velocity. Using these separately obtained solutions, we solve for corrections to the field variables that result from coupling between the subsystems. This coupling can be both direct (as in the case of field-conductivity interactions) and indirect (usually through temperature gradients induced by electric fields). These solutions are then used to calculate the forces (primarily DEP and drag) acting on a particle of known size and dielectric properties. The end result is a model for how the device will perform as a function of dynamic, geometric, and material parameters. With these models, we are able to specify the system's dimensions.

Throughout this work, we have placed a high priority on obtaining models that not only capture the system's behavior, but build insight as well. Accordingly, a proportionally large part of the discussion that follows is devoted to scaling analysis and the description of approximations made and the situations in which they are expected to be valid. We have adopted this approach in the belief that it more clearly illuminates the reasoning behind some of the design decisions made as well as alternatives not chosen that may yet be plausible. In the following sections, we begin by discussing the general architecture for the device and the underlying rationale. We proceed by describing each physical domain and their associated forces in isolation, followed by a discussion of coupling between the domains and the effect on the system's performance. The chapter culminates in specifications for the device's dimensions.

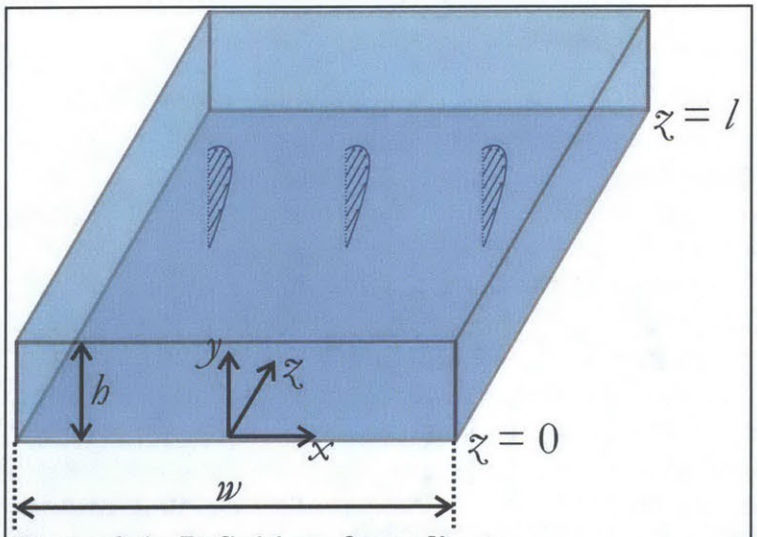

Figure 2-1: Definition of coordinates

Schematic representation of the geometry considered in section 2.1.

2.1 Flow and Transport Modeling

From the basic device concept, we may proceed to model the flow and transport of chemical species – the basis for the conductivity gradient – throughout the device. Figure 2-1 depicts the coordinate system and geometric parameters used in the following analysis. Flow through the device is pressure-driven, and consists of multiple stages. For now, we are concerned only with the final stage, within the separation chamber. The low aspect ratio ($h/w << 1$) enables the flow to be accurately modeled as parallel plate flow. Neglecting wall effects, we have:

$$v_z(y) = 6\left(\frac{Q}{wh}\right)\left[\frac{y}{h}\left(1-\frac{y}{h}\right)\right] \qquad \textbf{(2-1)}$$

Here, Q represents the volumetric flow rate, imposed by an external syringe pump. This volumetric flow is necessary to maintain a temporally stable conductivity gradient.

At the entrance of the separation chamber, a stepwise, conductivity gradient with linearly-spaced intervals between the high conductivity (σ_h) and low conductivity (σ_l) is present. The number of conductivity intervals depends upon the number of stages in the diffusive mixer, and determines the length needed to create a smoothly varying conductivity profile; fewer intervals in a chamber of fixed width take a longer time to smooth out. Since our primary concern is excessive attenuation of the gradient, few mixer stages are needed. We decide to use a two-stage mixer, producing four discrete conductivities along the width of the channel. This provides the boundary value at $z = 0$ we will need to model the evolution of the conductivity gradient downstream.

To solve the transport problem, we seek a conservation equation governing conductivity. Because the conductivity is determined by the concentration of positively and negatively charged species, we must take electrostatic interactions into account when solving for the conductivity throughout the channel. For this, we model the media as a binary, 1:1 electrolyte. Since the conductivity is controlled by adding saline to water, this is a good approximation. For such an electrolyte, the conductivity is given by:

$$\sigma = F\left[u_+c_+ + u_-c_-\right] \qquad \textbf{(2-2)}$$

where F denotes the Faraday constant, and u_i and c_i denote the respective mobilities and concentrations of the i^{th} ionic species. The conservation equations for the two species are given by:

$$\frac{\partial c_+}{\partial t} + \mathbf{v}\cdot\nabla c_+ = D_+\nabla^2 c_+ - u_+\left[c_+\left(\nabla\cdot\mathbf{E}\right) + \nabla c_+\cdot\mathbf{E}\right] \qquad \textbf{(2-3)}$$

$$\frac{\partial c_-}{\partial t} + \mathbf{v}\cdot\nabla c_- = D_-\nabla^2 c_- + u_-\left[c_-(\nabla\cdot\mathbf{E}) + \nabla c_-\cdot\mathbf{E}\right] \quad \textbf{(2-4)}$$

In this context, the electric field, **E**, is induced by the relative concentrations of positive and negative ions, as given by Poisson's equation:

$$\nabla\cdot[\varepsilon\mathbf{E}] = F[c_+ - c_-] \quad \textbf{(2-5)}$$

A good approximation for electrolyte solutions with large characteristic lengths is electroneutrality; that is, the concentrations of positive and negative ions are approximately equal [21]. Using this, we combine equations (2-4) and (2-5) to obtain the equivalent conservation equation for the conductivity:

$$\frac{\partial\sigma}{\partial t} + \mathbf{v}\cdot\nabla\sigma = \frac{2D_+D_-}{D_+ + D_-}\nabla^2\sigma \equiv D\nabla^2\sigma \quad \textbf{(2-6)}$$

With the conservation equation in this form, we are able to consider the solution conductivity independent of the electrostatic coupling between positive and negative ions with unequal diffusivities. An additional note regarding electronuetrality; although we have assumed that the space charge density throughout the fluid is negligibly small, this does not preclude the existence of a large induced electric field, as manifested by the diffusion potential. However, since we are expecting changes in conductivity of at most a factor of 10 across the channel's width, the coupling of ions will produce a potential on the order of the thermal voltage (~25mV). This is overwhelmed by the applied voltage, which is of order 10V, and is furthermore applied across a smaller distance. Consequently, any affects of the diffusion potential are ignored in this and all subsequent analysis.

Having solved for the velocity field and obtained the conservation equation governing conductivity, we may now model the evolution of the gradient throughout the separation chamber. To do this, it is useful to scale the governing equations. In the following analysis, the Peclet number is defined using the chamber width:

$$\mathrm{Pe} = \frac{Uw}{D} \quad \textbf{(2-7)}$$

where D is the equivalent diffusivity defined in equation (2-6). Assuming steady state and scaling x by the chamber width, y by the chamber height, and z by wPe, equations (2-1) and (2-6) combine to give:

$$6\tilde{y}[1-\tilde{y}]\frac{\partial\tilde{\sigma}}{\partial\tilde{z}} = \frac{\partial^2\tilde{\sigma}}{\partial\tilde{x}^2} + \left(\frac{w}{h}\right)^2\frac{\partial^2\tilde{\sigma}}{\partial\tilde{y}^2} + \left(\frac{1}{\mathrm{Pe}}\right)^2\frac{\partial^2\tilde{\sigma}}{\partial\tilde{z}^2} \quad \textbf{(2-8)}$$

To be consistent with later terminology, we scale the conductivity according to the average of the inlet conductivities, $(\sigma_h + \sigma_l)/2$. We immediately notice that for large Pe, as must be the case in our system, axial diffusion can be ignored. Somewhat more subtle is how we should treat diffusion in the y-direction. As a result of the parabolic flow profile, fluid near the channel floor or ceiling will have a longer residence time in the chamber than fluid near the center. In general, this will lead to shallower concentration gradients at the extremes of the channel, where molecules have had a longer time to diffuse [22]. However, a special case that applies to our system is when the channel width is much greater than the height ($w/h \gg 1$). Under these circumstances, and with no-flux boundary conditions at both the channel floor and ceiling, gradients in concentration cannot be supported in the y direction, since diffusion is so rapid. The result is that conductivity is very nearly independent of y. We may then integrate the PDE over the channel height to obtain:

$$\frac{\partial \tilde{\sigma}}{\partial \tilde{z}} = \frac{\partial^2 \tilde{\sigma}}{\partial \tilde{x}^2} \qquad \textbf{(2-9)}$$

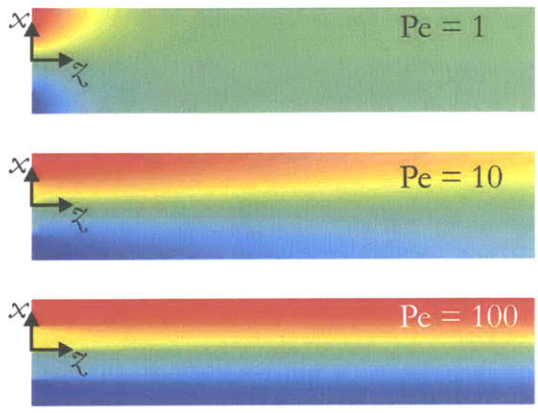

Figure 2-2: Varying the Peclet number

Solutions for equation 2-9 using different Peclet numbers. Pe >> 1 is necessary to preserve the conductivity gradient over the entire length of the channel.

This result represents a 2-dimensional boundary value problem which is readily solved using, for instance, the finite Fourier transform method [21]. The solution to this problem is plotted for channels of fixed length with variable Pe in Figure 2-2. We will return to this result in section 2.6 to determine the operating conditions and geometries in which the gradient will be satisfactorily preserved.

The analysis thus far has neglected the effects of the chamber's finite width. Wall effects alter the flow profile and, consequently, the conductivity gradient. To account for this, we consider the z-component of the Navier-Stokes equation:

$$\frac{1}{\mu}\frac{dP}{dz} = \frac{\partial^2 v_z}{\partial x^2} + \frac{\partial^2 v_z}{\partial y^2} \qquad \textbf{(2-10)}$$

From continuity and the other components of the Navier-Stokes, we conclude that dP/dz is simply a constant. Defining a disturbance velocity, Λ, as:

$$\Lambda(x,y) = v_z(x,y) - v_z^{\infty}(y) \qquad \textbf{(2-11)}$$

where v_z^{∞} denotes the infinite parallel plate solution, and assuming the sidewalls have a negligible affect on the total fluidic resistance (i.e. $P^{\infty} = P$, valid for $h/w << 1$), the PDE becomes homogeneous:

$$\frac{1}{\mu}\frac{dP}{dz} = \frac{\partial^2 \Lambda}{\partial x^2} + \frac{\partial^2 \Lambda}{\partial y^2} + \frac{\partial^2 v_z^{\infty}}{\partial y^2} \qquad \textbf{(2-12)}$$

$$\frac{1}{\mu}\left[\frac{dP}{dz}-\frac{dP^{\infty}}{dz}\right]\approx 0=\frac{\partial^2\Lambda}{\partial x^2}+\frac{\partial^2\Lambda}{\partial y^2} \qquad \textbf{(2-13)}$$

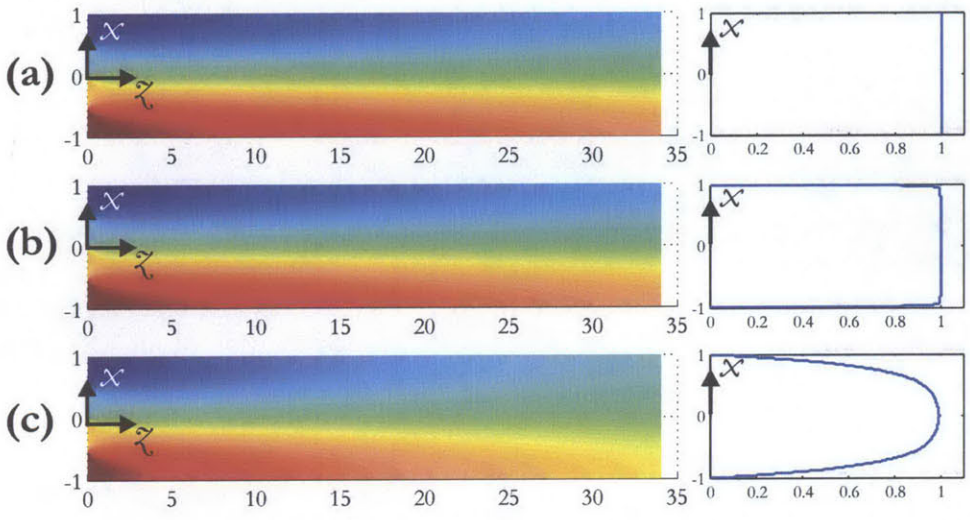

Figure 2-3: Wall stagnation

The effects (at constant Pe) of wall stagnation for h/w=0 (a), h/w=0.01 (b), and h/w=0.15 (c). Also shown (curves on the right) are the corresponding flow profiles, averaged over the chamber height.

The solution to this problem is again obtained using the finite Fourier transform. The solution for various values of h/w is shown in Figure 2-3, averaged over the chamber height.

To consider the affect of stagnation at the chamber sides on the conductivity gradient, we use spectral collocation, as described in [23]. Briefly, the eigenvalue problem associated with this boundary value problem is solved by converting the differential equation into a matrix equation using Chebyshev differentiation matrices. The resulting eigenvalues and eigenfunctions are then used to solve for and assemble the solution to the complete PDE. In Figure 2-3, we compare solutions obtained with and without wall effects. As might be expected, sidewall stagnation has little effect on the gradient evolution when $h/w \ll 1$; this is a consequence of the no-flux boundary condition on the sidewalls forcing any concentration gradients in this area to vanish.

Conclusions obtained through this analysis of transport offer several insights into the design of a device for IDS. First, we see that a high Peclet number is required if the gradient is to be preserved over the entire length of the channel. Recalling that the sensitivity of the separation requires that the DEP force overwhelms the drag force at all locations except near the particle's IDP, we conclude that high flowrates, and proportionally high mean fluid velocities, are to be avoided. This leaves the chamber width, w, as the most straightforward means of controlling Pe (although we do have some control over the species diffusivity). Thus the transport characteristics of the device are optimized by maximizing the width of the separation channel. A second conclusion that we may draw from flow and transport analysis is the advantage of using not only a wide chamber, but a shallow one as well. Constraining $h/w \ll 1$ creates very different timescales for y-directed and x-directed diffusion, with the result that no significant gradients in concentration can be supported along the height of the channel. It was also found that minimizing the ratio of height to width reduced the significance of wall effects on the flow profile. Since we want the force acting on a particle as it traverses the width of the

chamber to vary only with media conductivity, variations in the velocity field with respect to x are undesirable for IDS. Essentially, a wide channel preserves the conductivity gradient along the channel's width, while a proportionally shallow channel minimizes unwanted gradients in both conductivity and flow. We will see in later sections that these requirements are largely (and fortuitously) consistent with those imposed on the device's design by other factors.

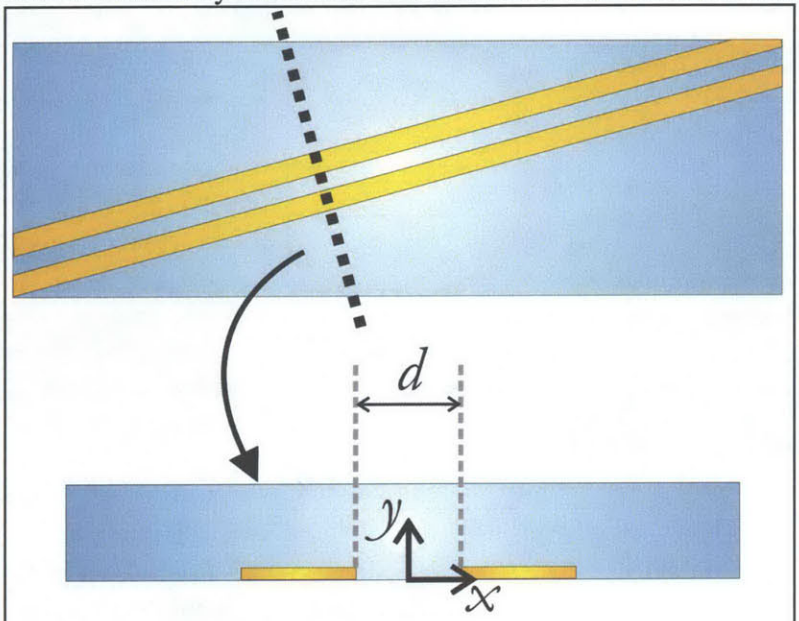

Figure 2-4: Coplanar electrodes

The coplanar electrode geometry and definition of coordinates used in section 2.2.

2.2 Electric Fields

Equally fundamental to the creation of a stable conductivity gradient in the implementation of an IDS device is the creation and shaping of electric fields. As outlined in chapter 1, we have elected to use planar electrodes to shape the field, placed across the diagonal of the chamber. We require that the electrode topology produce a field that is bi-directional in a plane normal to the electrode axis. This assures that the x-dependency of the total force acting on a particle will vary only with media conductivity. Under these constraints, the number of potential topologies is greatly reduced. Specifically, we compare coplanar strips (Figure 2-4), in which the electrodes are arranged side by side on a single substrate, to a parallel plate geometry, in which one electrode is placed on the bottom substrate with the second directly above it on the upper substrate. An important, if not particularly subtle, point is that since both geometries are governed by the same physics, there are limits to how different the field gradients and thus DEP forces they produce can be. It would seem reasonable to predict that, when channel height, h, matches the coplanar gap, d, the magnitude of the DEP force they produce would be very similar, with the coplanar geometry perhaps creating a somewhat weaker barrier, simply because only the very edges of the electrodes are separated by a distance d. This prediction is borne out by simulation. Since the parallel plate geometry will force particles undergoing n-DEP to the channel center, while the coplanar electrodes will force them to the channel ceiling, drag and DEP forces are taken at these respective locations for comparison. For $h = d$, the parallel plates deliver an x-directed DEP force at the channel center that is stronger by a factor of 7.75 than that produced at the channel ceiling by coplanar strips. However, this is largely compensated by the fact that the drag coefficient near the particle ceiling is ~5 times lower that at the channel center. We conclude that the two electrode geometries are very comparable in terms of their ability to hold particles against fluidic drag.

Ultimately, the coplanar geometry is chosen for ease of fabrication and flexibility in design. By patterning both electrodes on the bottom substrate, we avoid the need for wafer

bonding and alignment. This also enables the use of PDMS to form the microfluidic chamber. The result is a dramatically simplified process flow, discussed in greater detail in chapter 3. The other potential advantage of a coplanar geometry is that it decouples (to an extent) the channel height from the electric field strength. A wider design space is opened for consideration in this way. It is worth noting that none of this rationale suggests that the parallel plate geometry is inferior; indeed, by strength alone, it would modestly outperform the coplanar geometry in many cases. We have chosen the coplanar geometry for this initial implementation of IDS primarily to simplify fabrication.

Coplanar electrodes exhibit some interesting geometric dependencies. Of particular interest to us is how the field changes as the electrode spacing (*d*) relative to the chamber height (*h*) is varied. We begin with the simplest case; that of infinitely wide electrodes in an infinite half space (i.e. a chamber with a very high ceiling). This geometry permits an exact analytic solution, obtained by conformal mapping [24]:

$$\varphi(x,y) = V_0 \,\mathrm{Re}\left\{\frac{1}{2} + \frac{1}{\pi}\sin^{-1}(x+jy)\right\} \tag{2-14}$$

Far away from the electrodes (a radial distance $r >> d$), this can be approximated (in cylindrical coordinates) by:

$$\varphi(r,\theta) = -\frac{V_0}{\pi}\theta \quad \rightarrow \quad \mathbf{E} = \frac{V_0}{\pi r}\mathbf{e}_\theta \tag{2-15}$$

The magnitude and direction of the DEP force will thus be:

$$\mathbf{F}_{DEP} \propto \mathbf{E}\cdot\nabla\mathbf{E} = E_\theta \frac{\partial E_\theta}{\partial r}\mathbf{e}_r = -\frac{V_0^2}{\pi^2 r^3}\mathbf{e}_r \tag{2-16}$$

The DEP force is purely radial, and decreases as r^{-3}. This is significant, in that it suggests that the coplanar geometry is an extremely poor n-DEP barrier far away from the electrode gap. Particles carried by flow towards the barrier are pushed radially outward, in the direction of diminishing F_{dep}, until the drag force overwhelms DEP. So far, we have only formalized what is perhaps an intuitive result; that we must use the channel ceiling to stabilize the barrier, holding particles in close proximity to the region of high electric field. Thus we see that from an electrical perspective, as with the transport analysis, a shallow chamber should improve the device's performance.

Of course, decreasing the chamber height not only confines particles, but it distorts the electric field as well. This modified boundary value problem, in which an electrically insulating ceiling is imposed at some finite distance above the coplanar electrodes, does not, to my knowledge, permit an analytic solution. Others have had success using Fourier Series methods with polynomial interpolations for the BCs at $y = 0$, which produces very convenient and accurate results when the boundary value is very nearly independent of chamber height (true for values of *h/d* as low as 1/3) [25]. However, since we are potentially interested in cases where *h/d* << 1, we do not pursue this method further; nonetheless, this approach would provide a useful extension of the analysis presented here. We analyze the coplanar geometry using the finite element solver, Femlab (version 3.2, Comsol, Burlington, MA). In particular, we are interested in how the maximum *x*-directed DEP force (as calculated at the channel ceiling, where particles will be stably held) depends on the electrode spacing, *d*, and channel height, *h*. Before proceeding to the numerical analysis, we can gain insight into the DEP force scaling by considering a few asymptotic cases. When the electrode gap is much greater than the channel height (*h/d* << 1), we expect the field intensity gradient to scale as:

$$\nabla E^2 \sim \frac{1}{h}\left(\frac{V_0^2}{d^2}\right) \quad \rightarrow \quad \mathbf{F}_{DEP} \propto h^{-1},\ d^{-2} \tag{2-17}$$

This follows from the fact that the field will increase from ~0 to a value of *V/d* over a distance of a channel height, *h*. In the case that *h/d* >> 1, the problem reduces to that already considered, and we conclude that, at the channel ceiling (where $r \approx h$):

$$\nabla E^2 = -\frac{V_0^2}{\pi^2 r^3} \quad \rightarrow \quad \mathbf{F}_{DEP} \propto h^{-3} \tag{2-18}$$

This asymptotic scaling with channel height is seen in Figure 2-5, where the height dependence of these limiting cases are superimposed on the results from the finite element solution. From this, we see that the transition from one asymptote to the other occurs at h ≈ d, and that the limiting dependencies on *h* and *d* are roughly confirmed.

Also of interest to us is how these relationships change depending on whether we

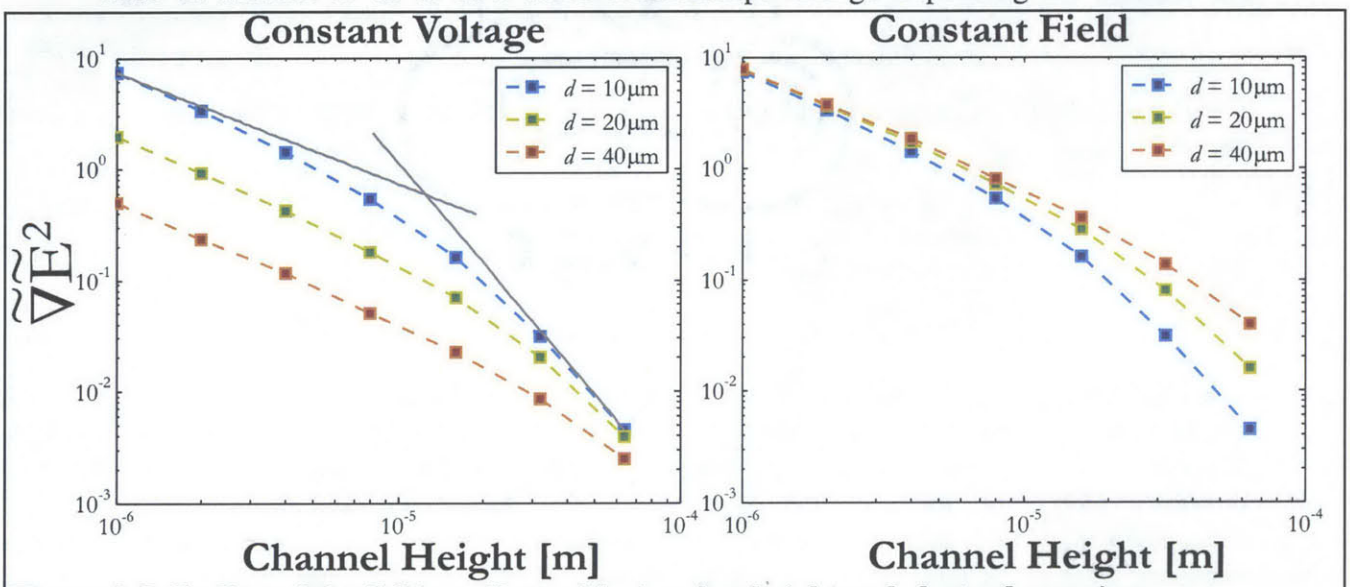

Figure 2-5: Scaling of the field gradient with chamber height and electrode spacing

Maximum values for the gradient of the square of the electric field intensity at the chamber ceiling. Both constant voltage and constant field (i.e. *V/d*) cases are shown.

constrain voltage or electric field. If it is the field, as defined by *V/d*, that is held constant, the force curves become independent of *d* as *h/d* → 0, as predicted by equation (2-17). Also, we see that the *wider* electrode spacing is uniformly better than the narrower ones at constant field; increased confinement of a field with constant magnitude creates a sharper field intensity gradient. This has several implications for the design of our device. Depending on the particles we are interested in separating, we may be more strongly constrained by voltage or field/current. The former is a constraint of instrumentation, while the latter is physical. As an example, insulating particles, such as polystyrene beads or some cell types at low frequencies, would be separated in similarly low conductivities. For these separations, where Joule heating and thermally induced fluid flows are expected to be small, we would be limited more strongly by the voltage our function generator can deliver than by the fields and subsequent heating: we would want a small electrode spacing. At the other extreme, some separations require physiological conductivities, in which heating and induced flows are a substantial concern: these

operating conditions, characterized by a threshold field that should not be exceeded, are optimized by increasing the electrode gap.

We can not optimize the device for all cases simultaneously. However, we are able to make some general decisions. If we are operating in a voltage-limited regime, narrow electrode spacing is desirable from the perspective of maximizing force. Alternatively, in a field-limited regime, force is maximized by wider electrode spacings. To resolve this conflict, we recognize that, in the absence of the non-idealities resulting from heating and induced flows, smaller electrode spacing is always desirable. We thus choose to maximize the DEP force we can deliver in the ideal case by setting $h \sim d$, and address the challenges presented by temperature and temperature gradients via alternate avenues. These approaches will be discussed in later sections.

As for the channel height, it is clear from Figure 2-5 that it should be absolutely minimized, subject only to practical constraints such as clogging and excessively high fluidic resistance. Given that the particles we are interested in separating range in size from ~1 μm to 5 μm, we tentatively set the chamber height to between 10 and 20 μm. In accordance with these heights, an electrode spacing of 15 μm is chosen. We will return to these decisions in later sections to confirm that they are in accordance with constraints imposed by other aspects of the system.

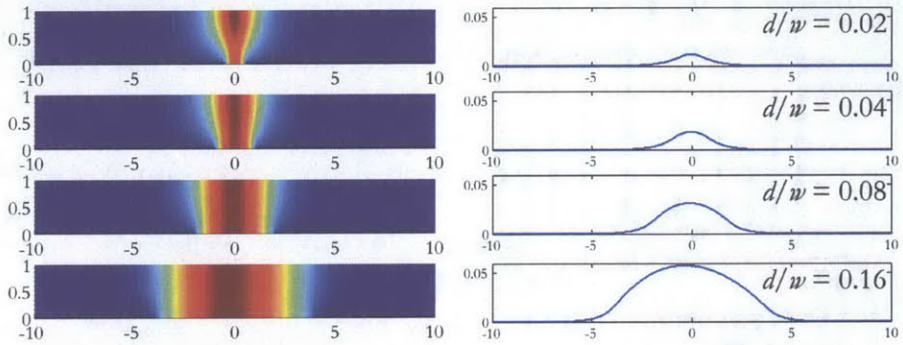

Figure 2-6: Perturbations of the electric potential arising from conductivity gradients
Surface plots (left) and corresponding cross-sections (right) of the change in the electric potential which arises in the presence of a conductivity gradient. As the lengths over which potential and conductivity vary become closer, the potential becomes increasingly distorted.

All of the electric field modeling presented so far is strictly valid only in the absence of media gradients. Since these gradients feature prominently in our device, we are interested in how they may be expected to affect its performance. We have already seen that gradients in the electrical properties of media tend to create oppositely varying electric fields, as required by conservation of charge. This motivated us to create disparate length scales for variations in conductivity and electric field, so that the conductivity change in the region of non-vanishing field is minimized. One way to quantify the influence of these media gradients is to decompose the electric potential into the superposition of a term that satisfies Laplace's equation, and a perturbation term representing the change in potential produced by polarization charge in the media. Figure 2-6 depicts the change in the potential introduced by media gradients. As more of the conductivity gradient is entrained in the region over which the potential varies, the potential (and by extension, the electric field) becomes increasingly distorted.

So far, we have decided that the channel height and electrode spacing should be approximately matched ($h \sim d$), and that the channel should have a low aspect ratio ($h/w << 1$).

It follows, therefore, that $d/w << 1$, as well. When this is the case, the perturbation the conductivity gradient introduces to the electric field will be significantly less in magnitude than the unperturbed field. This motivates its omission, in general, from calculations of the DEP force. However, this perturbation potential has as its origin an induced space charge, which combines with the applied electric field to produce a body force on the fluid. The effect of the conductivity gradient, while small in magnitude, introduces fundamentally new phenomena to the system. These new considerations may be relegated to second-order corrections, but they must be considered. In following sections, we will take this and related effects into account.

2.3 Modeling Forces

The field variables we have already solved for - electric fields, fluid flows, and media gradients - serve as the basis for calculations of the forces acting on a particle in our system. In the following section, the emphasis will be on determining the dielectrophoretic (DEP) and hydrodynamic drag forces, since it is primarily the balance between these forces that determines the sensitivity of the separation.

In order to create a maximally strong DEP force independent of a particle's size or electrical properties, a rapidly changing electric field is required. However, this is precisely what we assumed was not the case in the preliminary discussion of DEP presented in section 1.2. In order to correct for this, we need to take into consideration higher-order polarization moments and the subsequent polarization forces. The significance of these higher-order terms is illustrated by considering the mathematical formulation of these electrostatic boundary value problems. In the special case of section 1.2, where the field applied far away from the spherical particle was uniform, we were able to solve for the fields and moments exactly. The simplicity of this solution and the fact that the resulting field was equivalent to that produced by a dipole follows from the fact that the infinite condition (i.e. the field far away) matches a single eigenfunction of the axisymmetric boundary value problem (the Legendre polynomials in $\cos(\theta)$). To determine the significance of higher-order moments on the total DEP force in an axisymmetric field, we can solve for the fields and DEP force exactly, using an expansion of the applied potential in terms of $P_n(\cos(\theta))$. Since this expansion will generally require infinitely many terms, we conclude that, in general, infinitely many polarization moments will be induced. While the series expansion will often converge after only a few terms, in some cases, such as near a field null, higher-order terms can actually dominate the dipole term.

The situation becomes far more complex when the field surrounding the particle is no longer symmetric, and numerical routines become necessary to calculate the multipolar DEP force. An efficient algorithm for the calculation of these forces has been developed by Prof. Joel Voldman as part of his PhD thesis, and is the foundation of all DEP calculations done in this project [26]. The calculation is based on a formulation of multipolar dielectrophoretic theory presented in [27]. Using this source's notation, the (time-averaged) DEP force and (complex) polarization moment associated with the order n multipole are given by:

$$\underline{\mathbf{p}}^{(n)} = \frac{4\pi\varepsilon_m n R^{2n+1}}{(2n+1)!!}\underline{K}^{(n)}(\nabla)^{n-1}\mathbf{E}(\mathbf{r})e^{j\omega t} \tag{2-19}$$

$$\left\langle \mathbf{F}^{(n)} \right\rangle = \frac{1}{2n!}\mathrm{Re}\left\{\underline{\mathbf{p}}^{(n)}[\cdot]^n(\nabla)^n\mathbf{E}(\mathbf{r})e^{-j\omega t}\right\} \tag{2-20}$$

where the n^{th}-order CM factor is given by:

$$\underline{K}^{(n)}(\omega) = \frac{\underline{\varepsilon}_p - \underline{\varepsilon}_m}{n\underline{\varepsilon}_p + (n+1)\underline{\varepsilon}_m} \qquad \textbf{(2-21)}$$

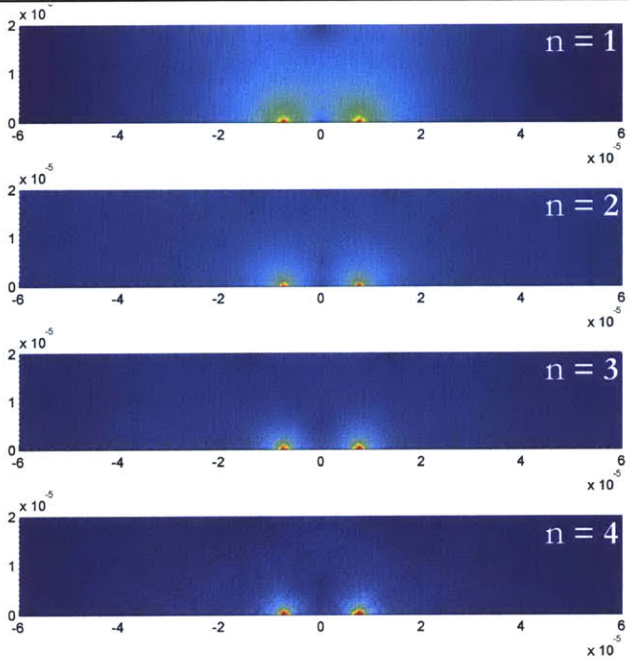

Figure 2-7: Multipolar DEP force magnitudes for the coplanar geometry.
The series is seen to converge rapidly in regions away from the electrode edge, where the field is singular.

As for the n = 1 (dipole) case, we see that the CM factor for arbitrary *n* vanishes exactly when the particle's effective dielectric properties match those of the media. Accordingly, we conclude that, although inclusion of higher-order force terms may have profound *quantitative* effects on how the device works and so must be taken into account, their *qualitative* effects – as defined by the existence and location of iso-dielectric points - are not significant.

Figure 2-7 shows the force calculations of increasing order for the coplanar electrode geometry used in the device, stretched to emphasize the shape of the field away from the electrode edges. As expected, in regions where the field is smoothly varying (i.e. away from the electrode edges), the force converges rapidly. Based on this observation, combined with the fact that we are primarily interested in n-DEP, where the particles are repelled from the electrodes, we choose to truncate the force calculation after two terms in most cases.

2.3.1 Lift and Drag Forces

Calculating the force exerted on a particle by the surrounding fluid presents a similarly challenging mathematical problem. In general, this requires calculation of the flow around the particle, followed by the integration over its surface of either the tangential (for drag) or normal (for lift) component of the total stress vector [21]. Here, we take advantage of the simple rectangular geometry of our flow chamber in using available analytic results for the drag on a particle in a parabolic flow profile [28]. In cases where the velocity field is not so regular, Stoke's drag, calculated from the unperturbed velocity at the particle's center, is used as a first approximation to the drag force.

2.3.2 Approximations and their Limits:

In obtaining these formulations for the forces in our system, it was necessary to make some approximations. First, in both drag and DEP calculations, the influence of other particles

was neglected. Since the presence of the particle in the flow or electric field clearly disturbs that field's shape, it is expected that these models may become inaccurate when particle concentrations become excessively high. From the nature of the equations and boundary conditions associated with the electrostatic and fluid dynamic problems, we expect the drag calculation to be limiting in this regard; the flow disturbance is expected to drop off as $\sim r^{-1}$ away from the particle, whereas electrical disturbance decreases more rapidly, as $\sim r^{-3}$.

Additional considerations must be made when the shape of the particle deviates from a perfect sphere [6]. The polarization of a non-spherical particle depends on the same variables that we saw for spheres – size, electrical properties relative to the media, but the forms of these dependencies vary and there is an additional dependence on orientation. Specifying the orientation of a particle subjected to DEP and hydrodynamic forces requires calculation of the spatially dependent torques throughout the system and the (stable) orientations in which they vanish. This couples the calculation of drag and DEP. Although considerable (and accurate) simplifications can be made by neglecting the inertia of the particles, the problem of calculating the orientation-dependent force field is considered unnecessarily complicated within the context of this project. Accordingly, orientational dependences are neglected everywhere except in the calculation of the CM factor. An ellipsoidal particle (i.e. bacterial cell) undergoing n-DEP in our device is eventually forced to the channel's ceiling. Here, only the x-component of the electric field is non-vanishing, and so it is assumed that all cells align parallel to the x-axis (perpendicular to the axis of the electrodes). In this orientation, the CM factor associated with the x-directed and y-directed DEP forces are, respectively:

$$\underline{CM}_x = \frac{\underline{\varepsilon}_p - \underline{\varepsilon}_m}{3\left[\underline{\varepsilon}_m + \left(\underline{\varepsilon}_p - \underline{\varepsilon}_m\right) L_{\parallel}\right]} \qquad \underline{CM}_y = \frac{\underline{\varepsilon}_p - \underline{\varepsilon}_m}{3\left[\underline{\varepsilon}_m + \left(\underline{\varepsilon}_p - \underline{\varepsilon}_m\right) L_{\perp}\right]} \tag{2-22}$$

The CM factor is thus modeled as constant but anisotropic throughout the chamber. In the case of ellipsoidal cells undergoing p-DEP, in which they are attracted to the electrode edges where the field aligns them to the y-axis, we simply switch the force component in which the shape factors, $L_{\parallel}$ and $L_{\perp}$, appear. Using dimensions reported in [29] for *E. coli*, the length factors are given by $L_{\parallel} = 0.173$ and $L_{\perp} = 0.413$ (as compared to $L_{\parallel} = L_{\perp} = 1/3$ for a sphere). In n-DEP operation, the x-directed DEP force is thus degraded by the alignment of the cell with the field by approximately 20%.

2.4 Coupling between the Subsystems: Electrohydrodynamics

So far, we have developed models describing how the different physical domains in the system (electrical and chemical/mechanical) behave independent of each other, and the forces they produce. We now consider the different coupling mechanisms and their influence on the overall performance of the device. Primarily, currents through the device dissipate power in the form of heat, creating thermal gradients. Since nearly all material properties – including density, viscosity, permittivity, and conductivity - exhibit some temperature dependence, it is expected that these gradients will have an appreciable effect on both the fields and flows throughout the device. In addition to these thermally induced gradients, we must account for interactions between the electric field and the imposed conductivity gradient, alluded to in section 2.2 and upon which the device's function relies. In this section, we will discuss the different mechanisms for coupling and the circumstances in which they are expected to significantly affect the device's performance.

Coupling between physical domains in the IDS device is described by combining Maxwell's equations (electroquasistatic form) with conservation of momentum, mass, chemical species, and energy:

$$-\frac{\partial \rho_e}{\partial t} = \nabla \cdot [\sigma \mathbf{E}] \tag{2-23a}$$

$$\rho_e = \nabla \cdot [\varepsilon \mathbf{E}] \tag{2-23b}$$

$$0 = \nabla \times \mathbf{E} \tag{2-23c}$$

$$\rho_m \left[\frac{\partial \mathbf{v}}{\partial t} + \mathbf{v} \cdot \nabla \mathbf{v} \right] = -\nabla P + \mu \nabla^2 \mathbf{v} + \rho_m \mathbf{g} + \rho_e \mathbf{E} - \frac{1}{2} E^2 \nabla \varepsilon \tag{2-23d}$$

$$0 = \nabla \cdot \mathbf{v} \tag{2-23e}$$

$$\frac{\partial \sigma}{\partial t} + \mathbf{v} \cdot \nabla \sigma = D \nabla^2 \sigma \tag{2-23f}$$

$$\rho_m c_p \left[\frac{\partial T}{\partial t} + \mathbf{v} \cdot \nabla T \right] = \kappa \nabla^2 T + \sigma E^2 \tag{2-23g}$$

To this system, we add the constitutive relationships relating any of the material properties given above to the local temperature, as well as all relevant boundary conditions. As posed here, this system constitutes a non-linear, time-dependent problem, the solutions of which are essentially unobtainable, numerically or otherwise. In order to capture the most relevant behavior, we seek simplifying assumptions that will render the system tractable. This process is aided enormously by comparing the dynamics of different subsystems and by dimensional analysis.

2.4.1 Simplifications based on timescales:

The timescales of interest that fall from the governing equations are given in Table 2-1. Under general operating conditions, the system exhibits dynamics spanning roughly 10 orders of

Timescale	Expression	Characteristic Values [s]
Charge Relaxation	$\tau = \varepsilon/\sigma$	$10^{-6} - 10^{-10}$
Applied	$\tau = 1/\omega$	$10^{-6} - 10^{-7}$
Conduction	$\tau = l^2/\alpha$	$10^{-2} - 10^{-4}$
Convection	$\tau = l/U$	$1 - 0.1$
Diffusion	$\tau = l^2/D$	$10 - 0.1$

Table 2-1: Timescales of the electrohydrodynamic system and their characteristic values.

magnitude. This essentially says that conduction, convection, and diffusion do not "see" the temporal variations in the field. This observation motivates the elimination of any explicit time dependence from the governing equations. We assume sinusoidal steady state for the EQS equations, and replace electrical terms elsewhere with time-averaged quantities.

Having eliminated the explicit time-dependence from the system, we proceed with a regular perturbation analysis [21]. The foundation of this perturbation analysis is the assumption that any gradients in any of the media properties can be accurately represented by a constant plus a small-amplitude perturbation:

$$b = b_0 + b_1(x,y) \quad \rightarrow \quad \tilde{b} = 1 + \tilde{b}_1(x,y) \tag{2-24}$$

This perturbation term (subscript '1') may be induced by temperature gradients or deliberately imposed on the system; the mathematical formulation will be identical. In all cases, we require that the perturbation term have a magnitude much less than that of the leading term. For simplicity, we will consider the thermal and imposed cases separately, beginning with otherwise uniform media perturbed only by changes in the fluid temperature. In the absence of any temperature non-uniformity, the system is described by the solutions obtained in previous sections; that is, we have already obtained the leading order terms (henceforth denoted with a subscript '0'). Our objective now is to scale the governing equations, introduce the perturbed media properties, and solve for the first correction of the electric and velocity fields. The scaled governing equations with time-averaging are:

$$-j\omega\tau_e\tilde{\rho}_e = \tilde{\nabla}\tilde{\sigma}\cdot\tilde{\mathbf{E}} + \tilde{\sigma}\left[\tilde{\nabla}\cdot\tilde{\mathbf{E}}\right] \tag{2-25a}$$

$$\tilde{\rho}_e = \tilde{\nabla}\tilde{\varepsilon}\cdot\tilde{\mathbf{E}} + \tilde{\varepsilon}\left[\tilde{\nabla}\cdot\tilde{\mathbf{E}}\right] \tag{2-25b}$$

$$0 = \tilde{\nabla}\times\tilde{\mathbf{E}} \tag{2-25c}$$

$$\mathrm{Re}\,\tilde{\rho}_m\left[\tilde{\mathbf{v}}\cdot\tilde{\nabla}\tilde{\mathbf{v}}\right] = -\tilde{\nabla}\tilde{P} + \tilde{\nabla}^2\tilde{\mathbf{v}} + \left[\frac{\rho_m h^2 g}{\mu U}\right]\tilde{\rho}_m\mathbf{e}_y + \left[\frac{\varepsilon E_0^2 h}{\mu U}\right]\left[\left\langle\tilde{\rho}_e\tilde{\mathbf{E}}\right\rangle - \frac{1}{2}\left\langle\tilde{E}^2\right\rangle\tilde{\nabla}\tilde{\varepsilon}\right] \tag{2-25d}$$

$$0 = \tilde{\nabla}\cdot\tilde{\mathbf{v}} \tag{2-25e}$$

$$0 = \tilde{\nabla}^2\tilde{T} - \mathrm{Pe}\left[\tilde{\mathbf{v}}\cdot\tilde{\nabla}\tilde{T}\right] + \tilde{\sigma}\left\langle\tilde{E}^2\right\rangle \tag{2-25f}$$

Scales used for the different variables are given in Table 2-2. In keeping with our goal of maximally simplifying the governing equations, it is enlightening to determine numerical values for the dimensionless groups that appear in the system. Comparing the coefficients of the

Variable	Scale Description
$\mathbf{E} = \tilde{\mathbf{E}} E_0 = \tilde{\mathbf{E}}[V_0 / d]$	Applied field
$\nabla = \tilde{\nabla} / h$	Chamber hieght
$\mathbf{v} = \tilde{\mathbf{v}} U = \tilde{\mathbf{v}}[Q/(wh)]$	Imposed velocity
$\rho_e = \tilde{\rho}_e[\varepsilon E_0 / h]$	Charge scale from Gauss's Law
$T = \tilde{T}\left[\sigma_0 E_0^2 h^2 / \kappa\right]$	Joule heating balanced with thermal conduction
$P = \tilde{P}[\mu U / h]$	Viscous pressure scale

Table 2-2: Scales for variables in the electrohydrodynamic system.

gravitational body force to that of the electrical body force, we find that the electrical force is generally several orders of magnitude higher. This motivates the elimination of buoyancy-driven flow from our model. We also find that under typical circumstances, both the Reynolds number and Peclet number are quite small (Re ~ Pe ~ 10^{-2}). The final step in formulating the equations is to account for the temperature dependence of the media conductivity and permittivity (the magnitude of inertial and buoyancy terms led us to discard any effects due to thermally induced variations in density). Linearizing about a reference temperature, T_0, gives:

$$b \approx b_0(T_0) + \left.\frac{\partial b}{\partial T}\right|_{T_0}\left[T(x,y) - T_0\right] \;\rightarrow\; \tilde{b} \approx 1 + \frac{\Delta T}{b_0}\left.\frac{\partial b}{\partial T}\right|_{T_0}\tilde{T}(x,y) \qquad \textbf{(2-26)}$$

where b denotes either permittivity or conductivity. It now becomes clear that the parameters we are expanding around in this perturbation analysis are these dimensionless coefficients mapping media properties to deviations from ambient temperature. Since the temperature coefficients for both permittivity and conductivity are ~ 10^{-2} K^{-1}, this approach is reasonable for temperature rises up to about 10K above ambient. For water at room temperature, a temperature coefficient (units of K^{-1}) of conductivity of 0.02 is used, and for permittivity, we use -0.004 [30]. Choosing the larger of these quantities as the coefficient for expansion, we seek solutions for all of the field variables of the form:

$$\Theta(\tilde{x},\tilde{y}) = \Theta_0(\tilde{x},\tilde{y}) + \Theta_1(\tilde{x},\tilde{y}) + O(a^2) \quad \text{where} \quad a \equiv \frac{\Delta T}{\sigma}\left.\frac{\partial \sigma}{\partial T}\right|_{T0} \qquad \textbf{(2-27)}$$

Implicit in this expansion is the assumption that the Θ_1 term is, at most, of order a. In some cases, it will be smaller, since we have chosen to expand around the (larger) temperature dependence of conductivity rather than that of permittivity. As shorthand, we refer to these terms as the O(a) terms. The leading term in the expansion corresponds to the solution in the absence of any gradients, which has already been solved. Keeping only O(a) quantities, the governing equations become:

$$-j\omega\tau_e\tilde{\rho}_{e,1} = \tilde{\nabla}\tilde{\sigma}_1\cdot\tilde{\mathbf{E}}_0 + \tilde{\nabla}\cdot\tilde{\mathbf{E}}_1 \tag{2-28a}$$

$$\tilde{\rho}_{e,1} = \tilde{\nabla}\tilde{\varepsilon}_1\cdot\tilde{\mathbf{E}}_0 + \tilde{\nabla}\cdot\tilde{\mathbf{E}}_1 \tag{2-28b}$$

$$0 = \tilde{\nabla}\times\tilde{\mathbf{E}}_1 \tag{2-28c}$$

$$0 = -\tilde{\nabla}\tilde{P}_1 + \tilde{\nabla}^2\tilde{\mathbf{v}}_1 + \left[\frac{\varepsilon E_0^2 h}{\mu U}\right]\left[\left\langle\tilde{\rho}_{e,1}\tilde{\mathbf{E}}_0\right\rangle - \frac{1}{2}\left\langle\tilde{E}_0^2\right\rangle\tilde{\nabla}\tilde{\varepsilon}_1\right] \tag{2-28d}$$

$$0 = \tilde{\nabla}\cdot\tilde{\mathbf{v}}_1 \tag{2-28e}$$

$$0 = \tilde{\nabla}^2\tilde{T}_1 + \tilde{\sigma}_1\left\langle\tilde{E}_0^2\right\rangle + \left\langle 2\tilde{\mathbf{E}}_0\cdot\tilde{\mathbf{E}}_1\right\rangle \tag{2-28f}$$

The system is simplified further by recognizing that the O(a) conductivity and permittivity are determined by the O(1) temperature gradient. Accordingly, for the first correction to the velocity field, we do not need to solve for the O(a) temperature. Combining equations (2-28a) and (2-28b) and substituting them into (2-28d), the Navier-Stokes equation becomes:

$$0 = -\tilde{\nabla}\tilde{P}_1 + \tilde{\nabla}^2\tilde{\mathbf{v}}_1 + \frac{1}{2}\left[\frac{\varepsilon E_0^2 h}{\mu U}\right]\left[\left(\frac{\tilde{\nabla}\tilde{\varepsilon}_1 - \tilde{\nabla}\tilde{\sigma}_1}{1+\omega^2\tau_e^2}\cdot\tilde{\mathbf{E}}_0\right)\tilde{\mathbf{E}}_0 - \frac{1}{4}\tilde{E}_0^2\tilde{\nabla}\tilde{\varepsilon}_1\right] \tag{2-29}$$

This is then solved along with continuity to obtain the leading order correction to the fluid velocity, due to thermally induced electrohydrodynamic flows. Figure 2-8a depicts the velocity field characteristic of this system.

A similar process is followed to analyze the influence of the imposed conductivity gradient in inducing EHD flows. The imposed conductivity gradient downstream of the inlet is adequately described by the first mode of the solution obtained in section 2.1. Scaling with respect to the mean conductivity gives:

$$\tilde{\sigma}(\tilde{x}) = 1 + \left[\frac{\sigma_h - \sigma_l}{\sigma_h + \sigma_l}\right]\sin\left(\frac{h\pi}{w}\tilde{x}\right) \approx 1 + \left[\frac{h\pi(\sigma_h - \sigma_l)}{w(\sigma_h + \sigma_l)}\right]\tilde{x} \tag{2-30}$$

The basis for an expansion of this form is the disparate length scales over which the conductivity varies as compared to other variables of interest; essentially, the conductivity is nearly constant over the region of non-vanishing electric field. This decoupling of the length scale for the conductivity gradient and the length scale characterizing the electric field is of fundamental

importance to our implementation of iso-dielectric separation. The linearized problem to be solved (in addition to continuity) is thus:

$$0 = -\tilde{\nabla}\tilde{P}_1 + \tilde{\nabla}^2\tilde{\mathbf{v}}_1 - \frac{1}{2}\left[\frac{\varepsilon E_0^2 h}{\mu U}\right]\left[\frac{\tilde{\nabla}\tilde{\sigma}_1}{1+\omega^2\tau_e^2}\cdot\tilde{\mathbf{E}}_0\right]\tilde{\mathbf{E}}_0 \qquad \textbf{(2-31)}$$

A solution to this equation obtained using a finite element solver is presented in Figure 2-8b.

2.4.2 Approximations and their validity:

A few points regarding the validity of this solution method as applied to both thermal and intrinsic cases deserve mention. First, since media gradients and the flows they induce are defined as first-order corrections to the system model, redistribution of these gradients by their respective flows are inherently assumed to be second-order corrections. As can be seen by considering the relevant conservation equations (2-23f and 2-23g), this is only guaranteed to be valid for vanishingly small Peclet number, in which case the temperature or concentration profile is decoupled from the local fluid velocity. While this is generally true for the thermal problem, it is not necessarily the case for Pe calculated from the species diffusivity. To capture the effects of convective mass transfer, we extend the perturbation analysis to solve for the second-order conductivity. Specifically, we have:

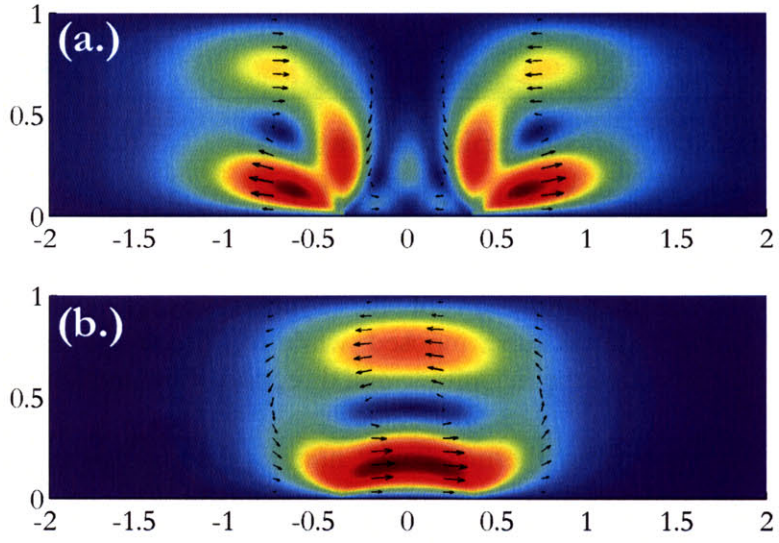

Figure 2-8: EHD velocity fields

Qualitative velocity fields produced by thermally induced gradients (a.), and the imposed gradient (b.). Quantitative results are discussed in section 2.5.

$$\tilde{\nabla}^2\tilde{\sigma}_2 = \mathrm{Pe}\left[\tilde{\mathbf{v}}_0\cdot\tilde{\nabla}\tilde{\sigma}_2 + \tilde{\mathbf{v}}_1\cdot\tilde{\nabla}\tilde{\sigma}_1 + \tilde{\mathbf{v}}_2\cdot\tilde{\nabla}\tilde{\sigma}_0\right] = \mathrm{Pe}\left[\tilde{v}_{x,1}\frac{\partial\tilde{\sigma}_1}{\partial\tilde{x}}\right] \qquad \textbf{(2-32)}$$

Solving this equation gives a sense for the influence of induced convection on the shape of the conductivity gradient. A plot of the shape of the correction to the conductivity, along with its characteristic magnitude as a function of voltage, is presented in Figure 2-9. At 10V, the second-order conductivity is ~10^{-2}. From this we conclude that, under conditions of interest, convective mixing is not expected to dramatically alter the solution for the induced velocity; the expansion, as posed, seems to be well-ordered in the sense that higher-order corrections rapidly decrease in magnitude.

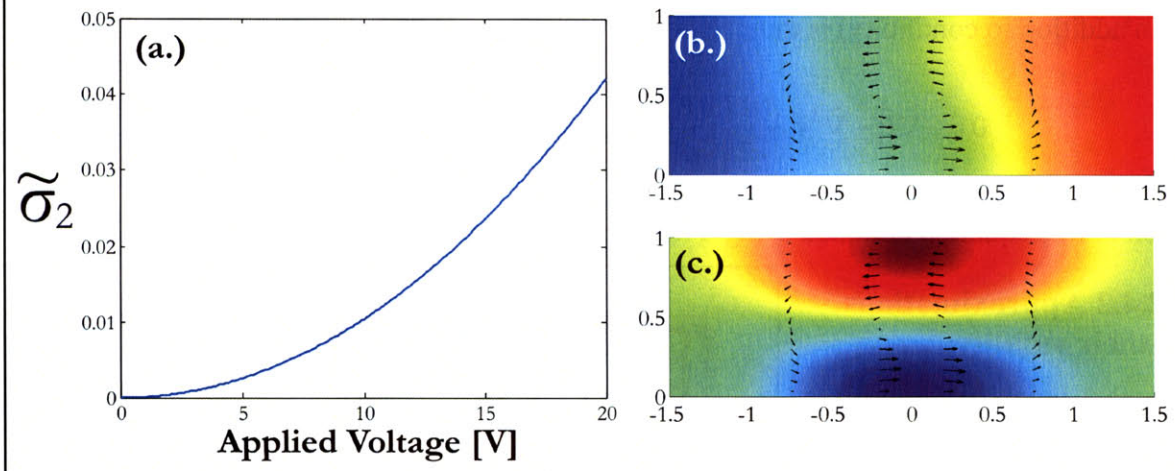

Figure 2-9: Mixing by induced convection

Inset (a.) depicts the maximum second-order conductivity disturbance resulting from induced flows as a function of the applied voltage. (b.) shows the first- and second-order conductivities superimposed, while (c.) shows the second-order conductivity alone. Arrows represented the magnitude and direction of the induced flow.

While the low thermal Peclet number assures that the temperature field is decoupled from the induced velocity, we must also confirm that the induced conductivity gradient does not substantially alter the electric field. Just as convective mixing was viewed as the primary threat to a well-ordered expansion in the case of the imposed gradient, a large correction to the electric field would compromise the validity of the analysis for thermally induced gradients. Figure 2-10 shows the first correction to the electric potential from gradients in the electrical properties of the media. Since this correction amounts to a perturbation of only ~1%, changes to the electric field are not expected to significantly undermine the validity of the analysis.

A second point worth mentioning in regards to the solution method described here is the distinction between the nature of the intrinsic EHD expansion and that used to solve for thermally induced flows. While the validity of the former is contingent on the smallness of a geometrical parameter (h/w), the latter requires that an operating parameter (the characteristic

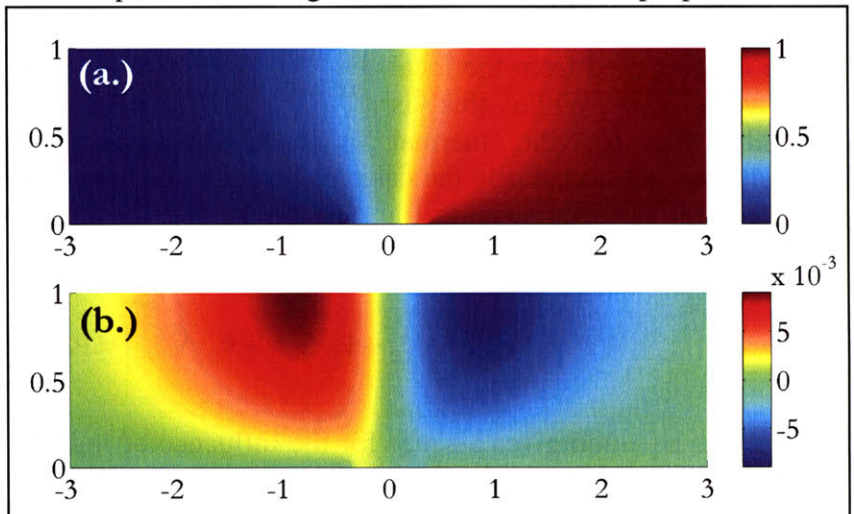

Figure 2-10: Change in potential due to thermally induced gradients

Total potential (a.) and first-order correction to the electric potential due to thermally induced gradients (b.).

temperature rise, ΔT) be small. For our device design, the geometric constraint is always satisfied, but the thermal constraint may not be. We see that under some conditions this analysis may become inaccurate. Nonetheless, we are able to predict for a wide range of valid operating conditions how these flows will develop and affect the performance of the device.

2.5 Scaling and Implications of EHD Flows

Some insight into the scaling of these flows can be obtained by considering the dimensionless parameters embedded in the governing equations. In both the thermal and imposed gradient cases, the electrical body force is scaled by a ratio of velocity scales (electroviscous [31] to imposed), multiplied by a parameter characterizing the magnitude of the gradients present in the system (in the general form of equation 2-26). The first distinction we notice is that, while thermally induced EHD is expected to scale as V^4, intrinsic EHD should scale as V^2. The additional factor of V^2 found in the thermal case follows from the electrical dependence of Joule heating; first the field must heat the fluid ($\sim V^2$), then it must induce ($\sim V$) and act upon ($\sim V$) the polarization charge. In the intrinsic case, the field simply induces and acts upon charge by interacting with gradients already present in the fluid. This expectation is borne out by numerical solutions to the governing equations, presented in Figure 2-11.

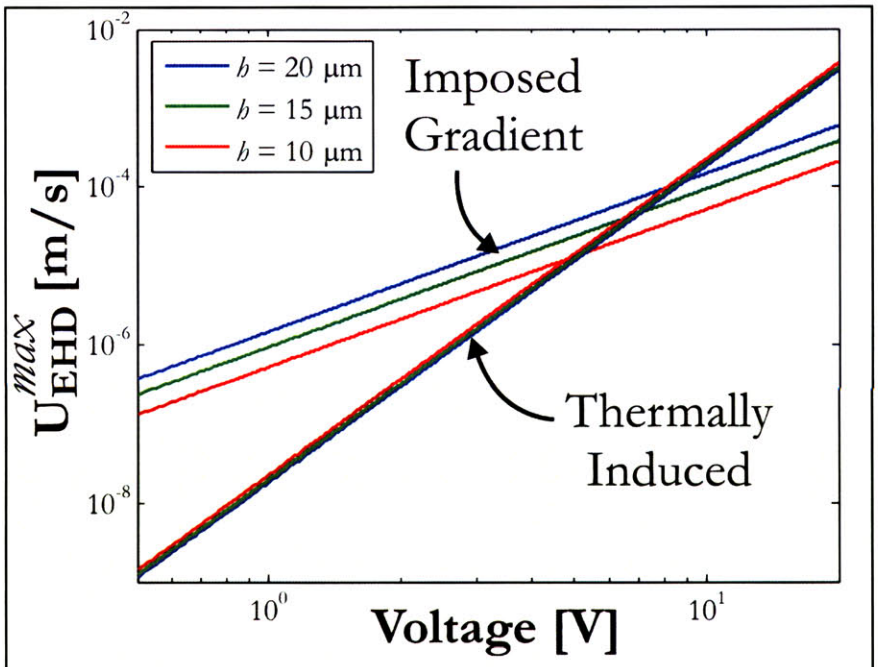

Figure 2-11: Scaling of EHD flow with voltage and chamber height

Comparison of imposed-gradient and thermally induced EHD flow as a function of the applied voltage, determined from the first-order numerical model. Velocities represent the maximum value of the velocity field throughout the device. The media conductivity is taken as 1 S/m, and the frequency is 1 MHz.

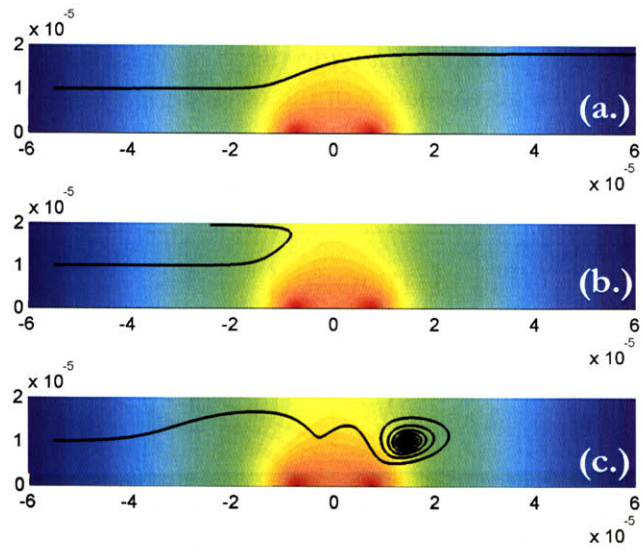

Figure 2-12: Operating regimes of the IDS device

(a.) Imposed drag dominant, (b.) DEP dominant, and (c.) EHD drag dominant.

A second distinction between the two types of flows involves their dependence on the channel height, h. As seen in the expression for the electroviscous velocity, decreasing the chamber height at constant field is expected to linearly reduce the induced velocity. This can be thought of as a shear stabilization effect. In the case of intrinsic EHD, an additional factor of h is introduced through the disparate length scales over which the field ($\sim h$) and conductivity ($\sim w$) vary. For the thermal case, the exact scaling of the flow with h is complicated by the fact that we have neglected in our temperature scale the effects of heat transfer through the substrate and channel ceiling. That is, the temperature scale we have used balances bulk power dissipation with heat conduction, ignoring heat transfer through surfaces. As a result, as interfacial heat transfer becomes dominant, the temperature scale, ΔT, may become inaccurate. As a consequence, the dimensionless temperature is expected to have a complicated dependence on channel height for h comparable to or less than d. From the numerical solution, we see that heat transfer through the substrate enhances the dimensionless temperature gradient (and by extension, the force on the fluid) so as to approximately cancel the influence of shear stabilization. The result is that, for typical geometries of interest to us, the thermally induced velocity is roughly independent of the channel height (Figure 2-11). Note that if the height were increased to the point that the temperature profile was no longer affected by it, we would expect an inverse dependence of EHD velocity on h to emerge, as seen for the imposed gradient flow.

For cases where the particles are sufficiently large and the media sufficiently insulating that thermal EHD is not a concern, we shift our attention to intrinsic EHD. Since this type of flow scales with voltage identically to DEP ($\sim V^2$), its significance can be controlled under all operating conditions by minimizing changes in conductivity over the region of non-vanishing electric field and through shear stabilization by the channel's ceiling. This can be done primarily through geometry; we see once again that a shallow and wide chamber is necessary. In our device, this mechanism for inducing flow is expected to be at least an order of magnitude less than the imposed flow ($\sim 10^{-3}$ m/s) and thus a secondary concern under all operating conditions (i.e. voltages and conductivities) of interest.

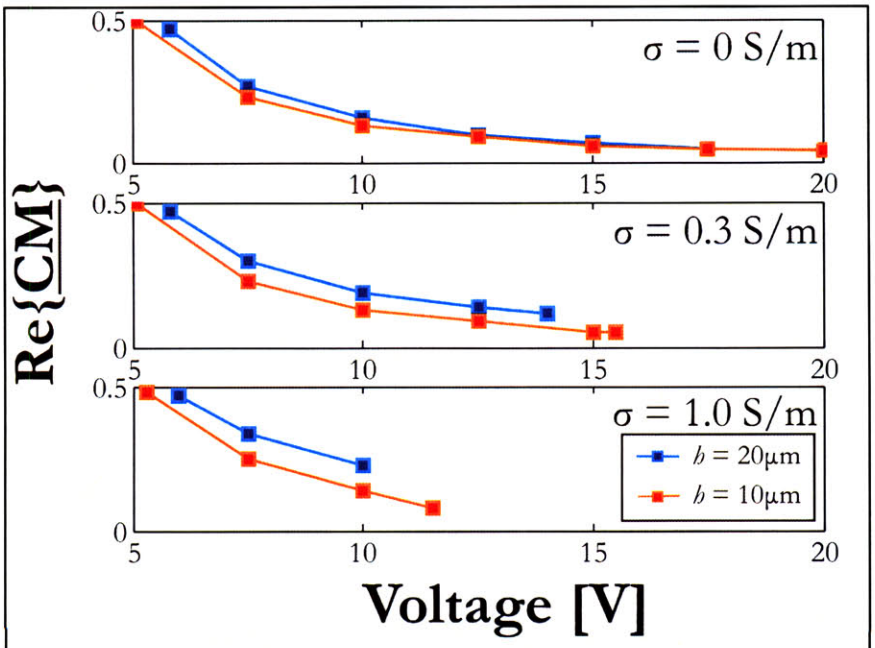

Figure 2-13: The effects of EHD on device performance

Plots of predicted device sensitivity vs. applied voltage, including the effects of EHD. For $\sigma > 0$, the highest voltage plotted represents the point at which device operation fails.

Having solved for the first-order induced velocities, we can extract some of the implications of EHD flows on the performance of our device. We begin by considering its effects on the force balance between drag and DEP. The three dominant forces in our system can be classified according to their voltage dependence as imposed drag ($\sim V^0$), DEP ($\sim V^2$) and EHD drag ($\sim V^4$). It follows that the relative significance of these forces will change depending on the applied voltage. Successful operation of our device requires that DEP be the dominant force until the magnitude of the CM factor reaches some threshold value, below which *imposed* drag dominates. A failure mode therefore occurs when EHD exceeds either of the other two forces, or when imposed drag exceeds DEP for all possible values of the CM factor. Besides these failure modes (shown in Figure 2-12), we also want to minimize the threshold value of the CM factor. Essentially, we wish to determine when a separation is possible (i.e. not a failure mode), and how sensitive that separation will be (i.e. the threshold CM factor). In order to use the CM factor as a metric for the device's sensitivity for a particle with completely arbitrary electrical properties, we vary conductivity and the CM factor independently. Also worth mentioning is the approximation used in the EHD drag calculations. Since the particle's position, the electrical body force on the fluid, and the channel's surfaces are all closely coupled, modeling the resulting drag force exactly is exceptionally difficult. An approximation that neglects the variability of the flow, rotation of the particle, and confinement by the chamber ceiling and floor is to use Stokes' drag and the unperturbed (by the particle) velocity field to determine the drag force. It is expected that this analysis will deviate from the physical reality - perhaps significantly. Nonetheless, we proceed by this method, as it offers some insight into the general impact of induced flow on the device's performance.

Figure 2-13 illustrates the simulated results for particles with a radius of 1 μm, subjected to 1 μL/min of flow for chambers with heights of 20 μm and 10 μm. A few noteworthy trends emerge. First, as the voltage is lowered, the sensitivity of the device decreases, as manifested by the increase in the threshold value of $\mathrm{Re}\{CM\}$. In the zero conductivity case, analogous to turning off EHD, the threshold value of $\mathrm{Re}\{CM\}$ approaches zero as the voltage is increased. At finite conductivities, however, as the voltage is increased, EHD eventually overtakes either imposed drag, DEP, or both – a failure mode. The result is a range of voltages under which

separations may be performed. As the conductivity increases, this range becomes narrower, and the sensitivity of the possible separations becomes lower. Performance improves when the channel height is reduced, in this case from 20 μm to 10 μm. The range of voltages and conductivities at which separations may be performed becomes wider, and the separations become more sensitive. This effect, which becomes more pronounced as the conductivity is increased, is primarily attributable to an increase in the DEP force at the chamber ceiling rather than a reduction in EHD flow from increased shear stabilization in a shallower channel. This follows from the scaling of the DEP force and the EHD velocity with channel height, as shown in Figure 2-5 and Figure 2-11, respectively.

A very important conclusion follows directly from this analysis: the performance of any device for IDS modeled around the architecture presented in this thesis is strictly bounded. Assuming a constant system geometry and material properties, the relative significance of drag and DEP will vary only with particle radius and applied voltage. The different size dependencies imply that there will always exist particles which are too small to separate with satisfactory sensitivity using this method at a given voltage. Furthermore, one is not able to indiscriminately increase the voltage, since the scaling of EHD drag relative to the DEP force precludes it. We see from Figure 2-13 that the maximum voltage we can operate at decreases with increasing conductivity. IDS, therefore, will work best for relatively large, relatively insulating particles.

The influence of unwanted gradients and subsequent flows can potentially extend beyond mechanical effects. Specifically, since media conductivity is the basis for separation, anything that affects the local media conductivity, either thermally or by EHD mixing, will also affect the performance of the device. We will now consider the changes to the conductivity gradient, originally solved in section 2.1, that result from temperature rises and convective mixing.

The temperature profile throughout the device is solved as an intermediate step in solving for the induced fluid velocity. Briefly, we assume that the temperature outside of the device is held at ambient, that the upper and lower substrates are PDMS and pyrex, respectively (see chapter 3 for discussion of these materials), and we solve for the temperature throughout the chamber by imposing continuity at the floor and ceiling of the channel. As a function of the applied voltage, we find the average temperature rise within three characteristic lengths (h) of the electrodes to be:

$$\langle \Delta T \rangle = 0.279 \frac{\sigma_0}{\kappa} V_0^2 \qquad \textbf{(2-33)}$$

where σ_0 and κ denotes the electrical and thermal conductivity of the fluid, and V_0 is the amplitude of the applied voltage (as opposed to the RMS value). A channel height of 20 μm and an electrode gap of 15 μm have been used as representative geometries. Using this expression and a temperature coefficient of 0.02 K^{-1}, we expect a conductivity of 0.5 S/m to increase by 48% under a 10 V signal. This percentage varies linearly with the media conductivity, and so for higher conductivities this effect becomes a significant consideration. However, this change in conductivity *by itself* (as distinguished from the flows it induces) is not thought to be limiting to device performance, as it is always possible to alter the imposed, concentration-dependent conductivity to compensate for these effects.

Convective mixing provides an alternate mechanism for changing the conductivity gradient, as has already been discussed in connection with EHD flows (see Figure 2-9). This is not expected to be a dominant effect, as follows from geometrical arguments: since the electric field and thus EHD flows are confined to a small fraction of the channel's overall width, a very

small fraction (~*h*/*w*) of the total conductivity gradient is subjected to EHD mixing at any particular point along the channel's length. One way, which is imprecise but intuitive, to consider this effect is to model the diffusivity as spatially varying, with an enhanced value in close proximity to the electrodes and constant everywhere else. The effective enhanced diffusivity can be found using scaling analysis and the equivalent forms of the conductivity conservation equation:

$$D_0\nabla^2\sigma = (\mathbf{v}_0 + \mathbf{v}_1)\cdot\nabla\sigma \quad \rightarrow \quad \nabla\cdot\left[(D_0 + D_1)\nabla\sigma\right] = \mathbf{v}_0\cdot\nabla\sigma \qquad \textbf{(2-34)}$$

Using this, we find that EHD flows effectively enhance the local diffusivity by an amount approximately equal to $|\mathbf{v}_1|h$, the characteristic EHD velocity times the channel height. At 10V, we see that this diffusivity increment will be, at most, of order 10^{-10} m^2/s, or about one order of magnitude less than the base diffusivity, D_0. Since the change in diffusivity is both small and highly localized, we find that the change in the conductivity gradient attributable to convective mixing is negligible under all geometries and operating conditions of interest.

2.6 Sizing the Device

With the understanding of IDS that we have obtained from this modeling, we are finally able to specify appropriate geometries for the device. This process is outlined sequentially in the following few steps.

Chamber Height: Recalling the results of section 2.2, especially Figure 2-5, the critical parameter for optimizing the system's electrical characteristics (i.e. the DEP force) was found to be the channel height. Since a shallow chamber height was shown to be additionally advantageous in mitigating EHD flows (section 2.5), as well as smoothing any *y*-dependence of the conductivity (section 2.1), we choose to *absolutely minimize* the chamber height. Since the particles we are interested in separating range in size from ~1 to 5 μm, we choose chamber heights ranging from 10 μm to 20 μm to accommodate them without clogging the device.

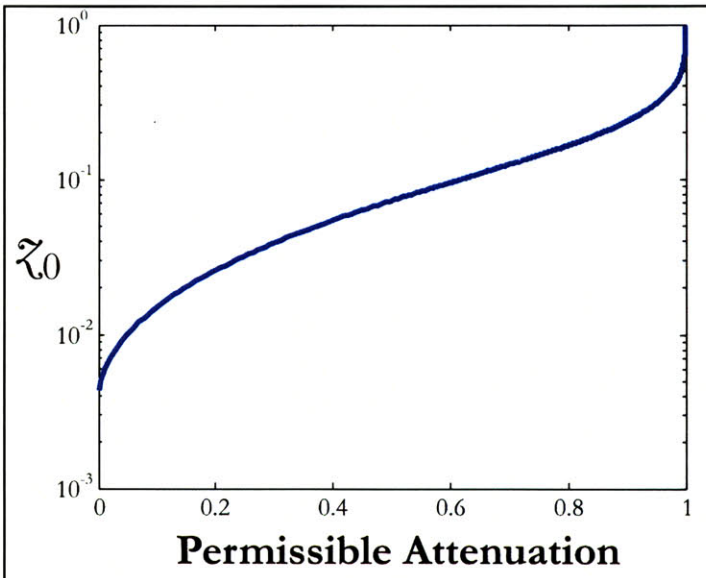

Figure 2-14: Quantifying gradient attenuation

The dimensionless parameter, $\tilde{z}_0$, as a function of the allowed gradient attenuation. An attenuation of 1 corresponds to complete attenuation.

Chamber Width: In scaling the transport model of section 2.1, we solved for the evolution of the conductivity gradient for a system with arbitrary Pe. In this example, it was found that a natural length scale for the *z* direction was *w*Pe, the channel width stretched by the Peclet number. We return to this solution to determine how the channel's length and width must be related to prevent excessive attenuation of the conductivity gradient. This gives us:

$$L = w\mathrm{Pe}\tilde{z}_0 = \frac{w^2 U}{D}\tilde{z}_0 \tag{2-35}$$

where $\tilde{z}_0$ is a dimensionless parameter selected by deciding the maximum allowed attenuation of the gradient. Figure 2-14 illustrates how this parameter depends on the permissible attenuation. To solve for the allowable chamber lengths and widths, it remains to specify the mean fluid velocity, U. For this, we return to force balance between drag and DEP.

In equilibrium (we are neglecting the presence of a conductivity gradient for now), the particle will move parallel to the electrodes at a constant velocity. Force balance in the x- and z-directions gives:

$$c_d(R)R\mu v_x = |\mathbf{F}_{\mathrm{DEP}}|\cos(\theta) \tag{2-36a}$$

$$c_d(R)R\mu[U - v_z] = |\mathbf{F}_{\mathrm{DEP}}|\sin(\theta) \tag{2-36b}$$

$$v_x = |\mathbf{v}|\sin(\theta) \qquad v_z = |\mathbf{v}|\cos(\theta) \tag{2-36c}$$

where θ denotes the angle of the electrodes with respect to the y-axis, U denotes the imposed fluid velocity, $\mathbf{v}$ denotes the particle velocity, and $c_d(R)$ is the drag coefficient. The fact that the imposed fluid velocity is spatially varying is taken into account by the dependence of the drag coefficient (c_d) on particle size (R); different size particles will be acted upon by different regions of the velocity profile. For a particle pressed up against the ceiling of the channel, where the fluid velocity varies nearly linearly, the drag coefficient is very nearly linear in R, making the drag force proportional to R^2. Replacing $c_d(R)$ with cR^2 and solving for U, we have:

$$U = \frac{|\mathbf{F}_{\mathrm{DEP}}|}{\sin(\theta)cR^2\mu} = \frac{|\mathbf{F}_{\mathrm{DEP}}|\left(w^2 + l^2\right)^{1/2}}{wcR^2\mu} \tag{2-37}$$

We now have an equation relating the magnitude of the DEP force to the mean fluid velocity by parameters related to the particle, fluid, and geometrical properties. From this, we see that the balance between drag and DEP is most favorable when the channel length is much greater than its width. Constraining this to be true, we can solve for the chamber width independent of its length:

$$w \approx \frac{\mu c \mathrm{R}^2 D}{|\mathbf{F}_{DEP}|\tilde{z}_0} \tag{2-38}$$

This expression is valid provided that $l >> w$. Note that, implicit in the DEP force is a dependence on particle volume; accordingly, w decreases as the particles of interest become larger. Calculating the DEP force and drag coefficient at the chamber ceiling we obtain:

$$|\mathbf{F}_{DEP}| = \alpha\varepsilon_m \mathrm{R}^3 K_0 V_0^2 h^{-3}$$
$$c = 8.4511\times10^6 \tag{2-39}$$

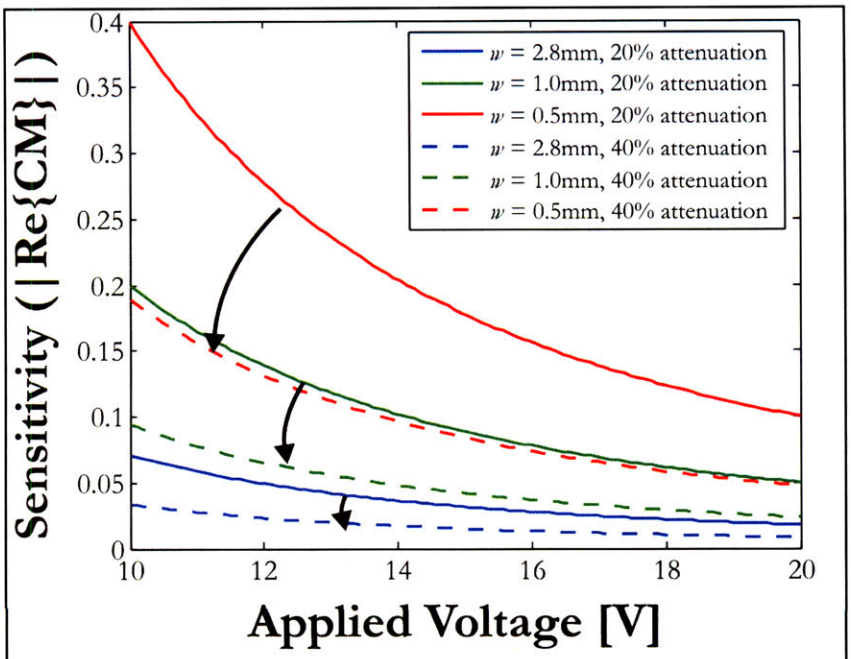

Figure 2-15: Value of Re{CM} at the IDP vs. voltage

Ideal separation sensitivities for specific channel widths and allowed gradient attenuations, as calculated from equations 2-38 and 2-39.

where c has dimensions of inverse meters, and K_0 denotes the minimum value of $\mathrm{Re}\{CM\}$ at for which the DEP force can still hold against flow, and the dimensionless coefficient, α, is determined by the ratio of the chamber height, h, to the electrode spacing, d. For values of h/d of 4/3, 1, and 2/3, respectively, we find values for α of 0.3678, 0.3117, and 0.1041. For the device to be maximally sensitive, we want K_0 and thus $|\mathbf{F}_{DEP}|$ to go to zero. Of course, the channel cannot be excessively wide due to practical constraints. As an example, it is not known a priori what minimum value h/w may assume before the device becomes unusable as a result of deformation of the PDMS channel. To be conservative, we design chambers with widths of 2.8mm, 1.0mm, and 0.5mm to accompany the heights of 10 to 20 μm. All of these devices are capable of producing reasonably sensitive separations ($\mathrm{Re}\{CM\} < 0.1$) at achievable voltages (<15V), without excessive attenuation of the gradient (<50%). Predicted (ideal) sensitivities are shown in Figure 2-15 for a range of voltages, widths, and allowed attenuation of the conductivity gradient. Clearly, wider channels would be expected to outperform narrower ones from this perspective. We will discuss the practical considerations for choosing conservative chamber widths further in the next chapter.

Chamber Length: The task of setting the channel's length is straightforward. We saw that, assuming $l >> w$, the channel length did not matter in influencing the device's performance. Physically, this follows from the cancellation of two effects: the decreased velocity component that the DEP barrier must block against combined with the higher mean fluid velocity needed to maintain the gradient over a longer channel. From the perspective of throughput, a long channel is favored, as it increases the volumetric rate at which the particles are separated. However, a longer channel increases the fluidic resistance and thus the pressure drop across the length of the channel. This could lead to deformation of the chamber or a compromise of the bond between the device and substrate. Since increasing l forces one to increase U (and thus Q, for a given cross-sectional area), the increase in pressure drop scales as length squared. Balancing these two options, a channel length of 1.5cm is selected. Unlike the width and height, we select a single length for fabrication because it facilitates the allocation of space on the mask. In the following

chapter, we will discuss in greater detail these geometric decisions and their implications on mask design, fabrication, and material selection.

2.7 Sensitivity to Variations in Particle Size

The analysis we have used here to size the device considers only particles of well-defined properties as inputs. In order to asses the device's sensitivity, we must extend our models to account for particles with statistically distributed properties. Having specified the channel dimensions, we are now able to approach this challenge. We simplify the analysis by considering only the effects of distributions in particle size, since this is most likely parameter to overwhelm electrical properties in determining IDPs; other considerations, such as variations in shape, are ignored. In this section, we will describe several models for predicting the sensitivity of the device. The ultimate objective is to derive models for the minimum change in conductivity, $\Delta\sigma$, that we are able to detect for particles with a given size distribution described by $R\pm\Delta R$.

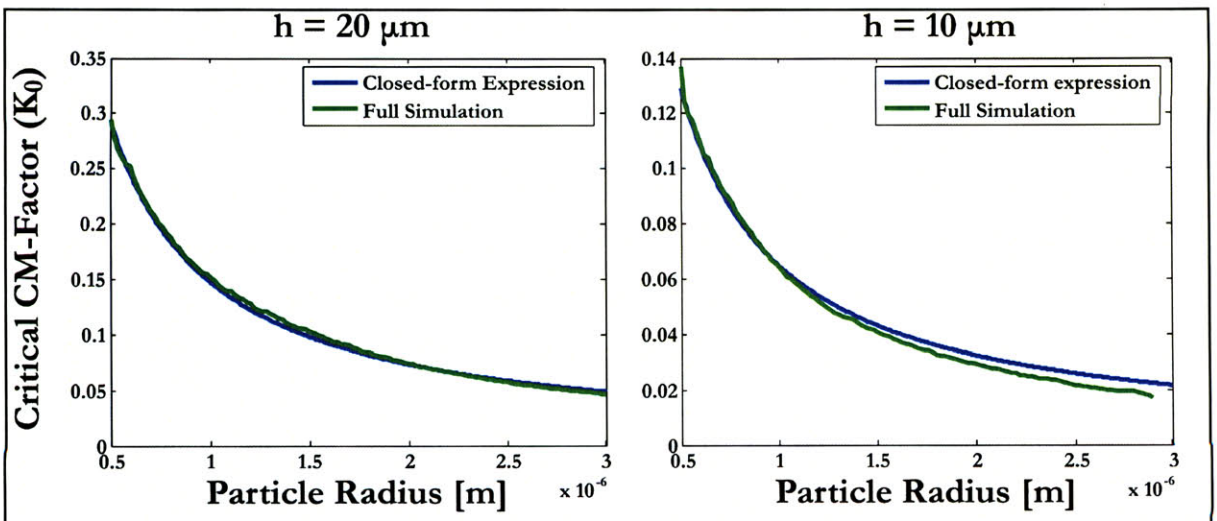

Figure 2-16: Comparison of scaling laws to results from full numerical simulations

Critical values for Re{CM} (at V_0 = 10 V_{pp} and $U = 0.833\times10^{-4}$ m/s) as a function of particle radius, as determined through numerical simulation (green) and fit to the expected functional dependencies (blue). The scaling laws are in excellent agreement except when particle size becomes comparable to the chamber height.

In section 2.3, we discussed the models we use for calculating the forces in our system, especially drag and DEP. Using these calculations, we may determine the trajectory of a given particle under given operating conditions. While knowledge of full particle trajectories is in many cases very useful, we are only interested in finding the value of Re{CM} at which drag overwhelms DEP, denoted here as K_0. If we are able to describe K_0 entirely in terms of physical and geometrical properties of the device and the particles without carrying around all of the additional spatial dependencies of the forces, our analysis will be greatly simplified. Our approach in the following, therefore, is to use the full numerical models and inferred functional dependencies to obtain a convenient, closed-form expression for K_0. Specifically, we will cast our expressions in terms of applied voltage, mean fluid velocity, and particle radius.

Equations 2-37 and 2-39 provide all of the information we will need. Combining these, we find that K0 can be written as:

$$K_0 = \frac{\mu \sin(\theta) c h^3 U}{0.3678 \varepsilon_m R V_0^2} = 0.0176 \frac{U}{R V_0^2} \quad (\text{for } h/d = 4/3) \qquad \textbf{(2-40a)}$$

$$K_0 = \frac{\mu \sin(\theta) c h^3 U}{0.1041 \varepsilon_m R V_0^2} = 0.00776 \frac{U}{R V_0^2} \quad (\text{for } h/d = 2/3) \qquad \textbf{(2-40b)}$$

This is a very useful result, as it decouples our analysis from the need to work any further with finite element models or numerical routines for calculating the DEP force to order *n*, provided the value of *h/d* is one for which we have solved for the dimensionless coefficient α (introduced on page 45). However, these expressions are not *exact*: for particles with diameters of >20% the total chamber height, the closed form expression begins to deviate slightly from the result obtained by full numerical simulation (Figure 2-16). This follows from the fact that the DEP force will increase as a particle's larger radius forces it closer to the electrodes, and the drag will be over-predicted, since the fluid velocity can no longer be approximated as varying linearly as the particle extends towards the chamber's center. Underestimating DEP and overestimating drag will overestimate K_0, which we see in the rightmost plot. These small corrections notwithstanding, we are sacrificing a small amount of accuracy in cases we are not particularly interested in (i.e. large particles) for increased facility and insight into how the device behaves.

In equations 2-40a and 2-40b, we have further lumped parameters together to obtain a more concise expression in terms of quantities which we will actively vary (U and V_0) or which will vary independent of our wishes (R). The remaining variables are combined into a coefficient (henceforth denoted generically as β, although it assumes different values depending on *h/d*) which we treat as a constant from now on. To estimate the sensitivity of the device for separations of +/- PHB *E. coli*, we begin by assuming that we are operating in a frequency regime where the CM factor is determined exclusively by the cytoplasmic conductivity of the cells, σ_p. We can then solve for the media conductivity in which cells will pass over the DEP barrier:

$$\sigma_m^0 = \sigma_p \left[\frac{1 - K_0}{1 + 2K_0} \right] = \sigma_p \left[\frac{R V_0^2 + \beta U}{R V_0^2 - 2\beta U} \right] \qquad \textbf{(2-41)}$$

If we know the media conductivity at all points in the channel (note that it also varies with U), we can invert this relationship to obtain IDP as a function of the media conductivity, and by equation 2-41, particle conductivity and size. We will calculate this using the full solution for the conductivity gradient momentarily, but first it is enlightening to approximate the media conductivity as varying linearly with position along the channel's width, with no attenuation along the channel's length. This gives us:

$$x_0 = \frac{w}{(\sigma_h - \sigma_l)} \left[\sigma_p \left(\frac{R V_0^2 + \beta U}{R V_0^2 - 2\beta U} \right) - \sigma_l \right] \qquad \textbf{(2-42)}$$

where x_0 denotes the IDP. This result presents some conclusions that we had arrived at previously from a somewhat new perspective. If we want the IDP to be independent of particle size, we require that $RV_0^2 >> \beta U$, which causes the ratio involving R to approach unity (note that

we cannot make $\beta U >> RV_0^2$ simply because the IDP will cease to exist). Insensitivity to R can therefore be achieved by using high voltages, large particles, or low mean fluid velocities (of course, we have neglected diffusion, which provides a lower limit for U). Differentiating equation 2-42 with respect to R allows us to obtain:

$$\Delta x_0 = \left[\frac{w\sigma_p}{(\sigma_h - \sigma_l)}\left(\frac{3\beta U V_0^2}{\left(RV_0^2 - 2\beta U\right)^2}\right)\right]\Delta R \qquad \textbf{(2-43)}$$

We have now related the spread in particle sizes to a corresponding spread in IDPs. Using this, we can obtain an analytic expression for the minimum conductivity increment needed to get arbitrary purity for a population with a variance in size of ΔR. Defining our criteria for minimum purity as one standard deviation (Δx_0) between the IDP associated with particles of two distinct conductivities ($\sigma_p^{(0)}$ and $\sigma_p^{(1)}$) we obtain:

$$\frac{\sigma_p^{(0)}}{\sigma_p^{(1)}} = \frac{\left[\left(RV_0^2 + \beta U\right) - \frac{3}{2}\left(\frac{\beta U V_0^2 \Delta R}{RV_0^2 - 2\beta U}\right)\right]}{\left[\left(RV_0^2 + \beta U\right) + \frac{3}{2}\left(\frac{\beta U V_0^2 \Delta R}{RV_0^2 - 2\beta U}\right)\right]} \qquad \textbf{(2-44)}$$

Taking the equivalent radius of *E. coli* as 0.7um ± 50% and the channel height as 10 μm, we tabulate a few values for the minimum conductivity difference we can separate:

	0.5 μLmin^{-1}	**0.25 μLmin^{-1}**
10 V	14.4%	7%
15 V	6.2%	3.1%

We expect these percentage differences in conductivity to translate roughly into percentage differences in intracellular concentrations of PHB. While we have not taken the effects of EHD explicitly into account here, we see from Figure 2-13 that, at media conductivities of around 0.3 S/m, we are able to operate at up to 15 V. Accordingly, separation of cells with differences in PHB concentration of ~3% in the presence of size variations of ~50% should be achievable with our device.

For completeness, we now incorporate diffusion into the analysis. Figure 2-17 illustrates the expected distributions of IDPs for the four voltages and flowrates we have tabulated at conductivity increments of 15%, in the presence of gradient attenuation via molecular diffusion. We see that decreasing the flowrate by a factor of two does not result in attenuation of the gradient sufficient to have an adverse effect on performance.

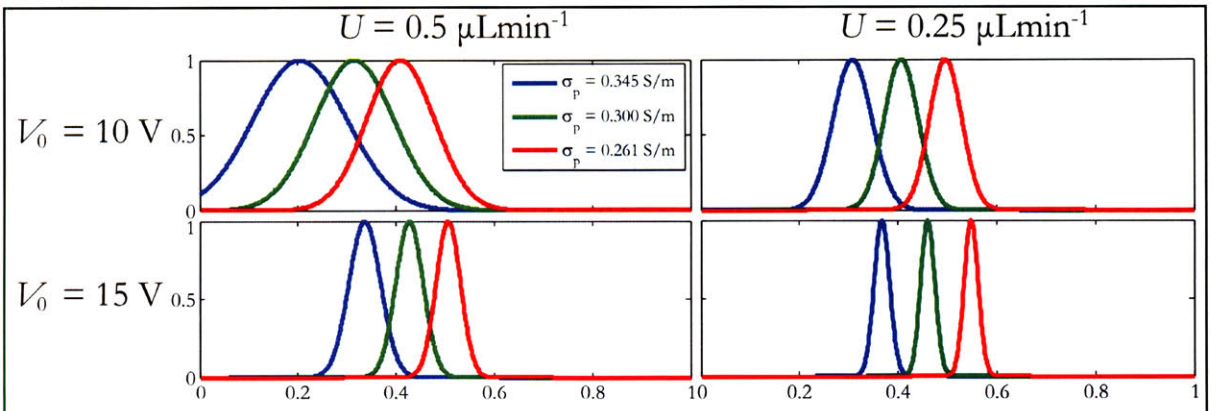

Figure 2-17: Predicted IDPs, assuming a normal distribution

Predicted (normal) distributions of IDPs for R = 0.7um ± 50% and h = 10 μm for conductivities of 0.3 S/m (green), 0.3 S/m + 15% (blue), and 0.3 S/m – 15% (red).

The final approach we will discuss in developing models for device sensitivity is that of Monte Carlo simulations. So far, we have assumed that both cell sizes and IDPs are normally distributed, when in fact they are not. To improve upon this somewhat, we may generate a (normal) distribution of particle sizes and calculate explicitly the IDP of each. Assembling a histogram of these IDPs should then give us a sense of the asymmetric distribution. Figure 2-18 shows the results of these simulations, with each curve representing the IDPs 10^4 cells with the same size distributions as Figure 2-17. While the expected asymmetry is observed, it does not seem to significantly alter the expected purity under any given operating condition.

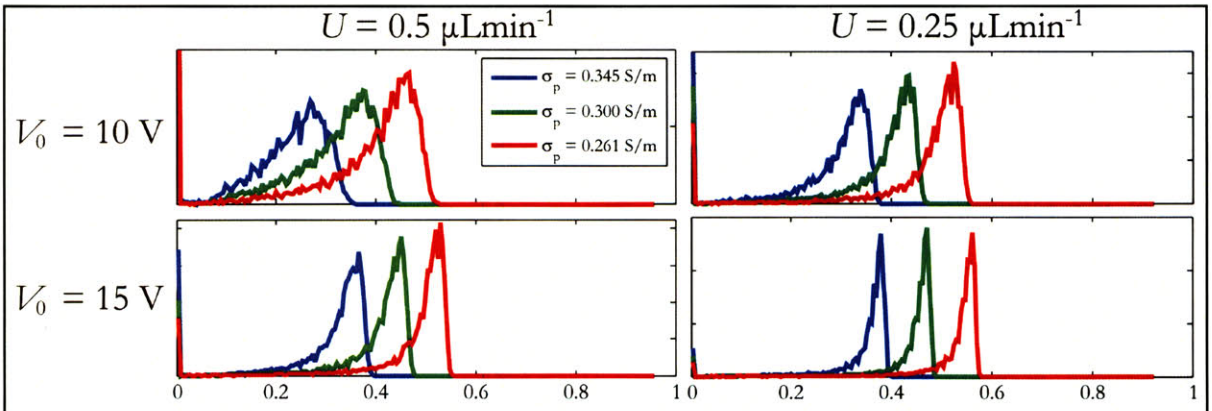

Figure 2-18: Predicted IDPs from Monte Carlo simulations

Plots analogous to those of Figure 2-17, obtained using a Monte Carlo simulation to approximate the distributions of IDPs.

Chapter 3: Fabrication

One of the motivating factors behind our choice of architecture for IDS was ease of fabrication. Because the electrode topology we have chosen lies in a single plane and the accompanying fluidic chamber is of uniform height, the design requires only two masks, both with minimum feature sizes greater than 10 μm. In this chapter, discussion begins with the process by which we designed the masks and allocated space to different electrode and chamber geometries. From this, we proceed to discuss the microfabrication of the device's electrical and fluidic components. Because the processes described here are widely used (see for example, [32]), we will outline them only briefly, with emphasis placed on a few steps and protocols that we found to be critical.

3.1 Mask Design and Layout: Electrodes

The masks for both electrical and fluidic components of the device followed directly from the modeling discussed in chapter 2. Because the important considerations of IDS vary widely depending on the particles we are interested in separating (especially their size and electrical properties), and because we would like as much flexibility in our design as possible, we fabricate several variations on the common theme. We begin with the electrode mask, shown in Figure 3-1. At a die size of 21×34 mm, 16 devices fit on a 6" wafer. The 16 devices are comprised of three different device widths and two variations on the coplanar electrode topology. In addition, some other performance-optimization features have been included on many of the die, which we will discuss in some detail.

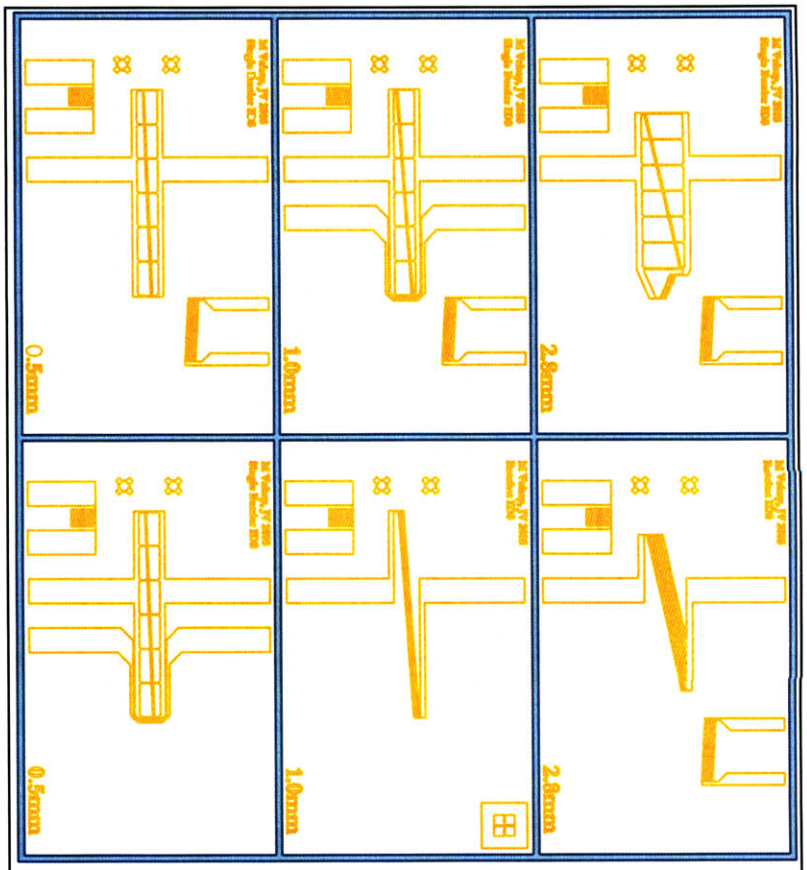

Figure 3-1: Design variations on the electrode mask.

3.1.1 Channel Widths:

One of the most fundamental conclusions reached in the device modeling is the affect of chamber width on the force balance between drag and DEP. As discussed in section 2.1, increasing the channel width slows the attenuation of the conductivity gradient proportional to w^2, enabling operation at a lower fluid velocity and thus higher sensitivity. This is canceled to

some extent by the fact that the electrode must span the channel's diagonal, forcing the DEP barrier in a wider chamber (of fixed length) to hold against a larger component of the particle's resolved velocity. Nonetheless, force balance was seen to favor a wider channel (equation 2-38). However, this modeling did not take into consideration some practical concerns. Since the chamber is to be made from PDMS, a low modulus polymer, it is subject to deformation. This is can be shown to be more problematic for wider chambers. If deformation of the PDMS leads to significant deviation of the channel's cross-section from rectangular, operation of the device would be compromised. A variable channel height means that the force acting on a particle as it traverses the width would not depend solely on the local conductivity.

In order to predict how significant a problem deformation of our device will be, we approximate the maximum deflection of the chamber ceiling using the approaches outlined in [33]. For a parallel plate flow chamber, such as ours, the pressure drop is related to the flowrate by:

$$\Delta P = \frac{12\mu l}{wh^3} Q \tag{3-1}$$

As a conservative estimate for the deflection of the chamber ceiling under this distributed load, we model the chamber ceiling as a simply-supported beam. Modeling the ceiling in this way roughly accounts for the ability of the side walls of the chamber to deform. The maximum change in the chamber height is then given by:

$$\Delta h = \frac{5\Delta P w^4 l}{384 EI} \tag{3-2}$$

where E denotes Young's modulus for PDMS, and I denotes the moment of inertia for a rectangular beam. Substitution of typical values into this expression predicts deflections of, at most, on the order of 10^{-9} m. This is well beneath what would be acceptable. Still, the coarseness of this analysis warrants some degree of caution.

There are other reasons for avoiding an excessively wide channel. A second consequence of increasing w is that it forces particles to move in a direction increasingly perpendicular to the imposed flow. Since particles being guided by the barrier are therefore moving much more slowly along the axis of the channel than particles acted upon by drag alone (i.e. as they are delivered to the barrier), the local concentration along the electrodes could become very high. Not only would this dramatically alter the electric and velocity fields, invalidating much of the modeling upon which the design is based, but particles incident on the barrier could force others past it prematurely. In a comparatively narrow channel, axial particle velocities are less significantly altered by the barrier, mitigating the problem of high local concentrations. Essentially, it is expected that restricting the channel width to some extent will help to prevent non-idealities that were not incorporated into the modeling. Since the significance of these effects is unknown, we conservatively settle upon three previously stated channel widths of 2.8mm, 1.0mm, and 0.5mm. We will return to these considerations in chapter 5, when we discuss how these device geometries compare in practice.

3.1.2 Electrode Variations:

In addition to the three different widths, we fabricate two different classes of electrode topologies, both of them coplanar and closely related. These include single barrier devices,

named from the presence of only a single diagonal electrode pair across the flow chamber, and ratchet devices, consisting of an interdigitated array of electrodes similarly arranged across the channel diagonal. The inclusion of these two variations follows from performance predictions both quantifiable and less so. The first such consideration is that of impedance. The resistance and capacitance of the electrodes are calculated from the finite element solutions for the electric fields, discussed in section 2.2, by integrating the current and charge densities associated with each electrode. Accounting for the total length of the electrode (i.e. the separation chamber diagonal), we find the resistance (at a media conductivity of 1 S/m and electrode length of 1.5 cm) to be 120 Ω and the capacitance to be 5.9×10^{-12} F. For frequencies of interest (10^5 to 10^7 Hz) and the stated conductivity, the device is purely resistive. Since the device is to be driven by a function generator with a source impedance of 50 Ω, we see that at this conductivity and with only a single electrode, the voltage delivered to the electrodes has been attenuated by a factor of 0.7 from the nominal applied voltage. The situation is less favorable still when we consider placing several of these electrodes in parallel, as is done for the ratchet device. With 10 electrode gaps, the impedance becomes 12 Ω, and the voltage drops to about 20% the nominal value. To avoid this difficulty when attempting high conductivity separations, we favor single barrier devices from an impedance perspective.

Of course, the ratchet topology is not without merit. At moderate to low conductivities, where impedance is no longer a concern, an array of electrodes offers redundancy; if a particle is forced past the first electrode barrier prematurely, it may still be held by subsequent barriers, improving the device's robustness. This topology is further benefited by the fact that the electrodes are spaced (at a periodicity of 75 μm) such that the fields produced by one pair do not couple to the fields of an adjacent pair, resulting in force characteristics for the ratchet barrier that are essentially identical to those of the single barrier design. An additional consideration, not pursued in this thesis, is the possibility of spacing the electrodes so that they couple thermally, but not electrically – this may help to reduce flow-inducing temperature gradients, even while increasing the overall temperature rise. At any rate, as fabricated, the ratchet electrodes are expected to behave as a periodic tiling of the solutions already obtained for the electric fields, temperatures, and flows associated with the single barrier design.

3.1.3 Optional Features:

In addition to the key components for IDS, the electrode masks include some additional features designed to enhance the device's performance where applicable. The first such feature we will refer to as a pre-focusing stage. Since the particles to be separated are introduced into the device via one inlet, and since they diffuse negligibly owing to there large size, they will enter the separation chamber spanning one half of the conductivity gradient. This is undesirable, as it compromises separation of particles with IDPs somewhere along that half of the gradient; they are past the appropriate conductivity before even reaching the electrode barrier. To mitigate this problem, the inlets are stretched to accommodate an additional bank of electrodes, arranged at an angle with respect to the direction of flow, that serve to steer particles closer to one side of the channel prior to entering the diffusive mixer. The concept is illustrated in Figure 3-2. Of course, this method of particle focusing/concentration has some potential short-comings. First, in cases where it is needed most (i.e. when the particle conductivity is close to that of the media in which it is suspended), it is the least effective. This follows from the fact that the particles in these cases are originally suspended in conditions that approximate their iso-dielectric media, and the DEP force is small. In some cases, this can be resolved by operating the pre-focusing

electrodes at a frequency for which the DEP force is strong. Another possible drawback of using electrodes to push particles to one side of the chamber is that these electrodes either draw current away from the main separation barrier, or require additional instrumentation. These problems can be solved, at the expense of more complicated experimental protocol, by injecting more than two conductivities into the device; three inlets would restrict particles to one-third of the channel, four to one-fourth, *ad infinitum*, or at least to the limit of practicality. We have decided against this approach simply as a means of simplifying use of the device.

A second set of features included on some of the die is what we will call a levitation stage. The layout and operation of this structure is shown in Figure 3-3. Essentially, it serves the purpose of levitating particles to the chamber ceiling prior to their arrival at the electrode barrier. The rationale behind this structure, quantified by the graph in Figure 3-3 (left), is simply that, in n-DEP operation, it is easier to hold particles that have already been levitated than to both levitate and hold them using a single pair of electrodes. Similarly for p-DEP, the electrode barrier is much more efficient if particles first encounter while they are close to the chamber bottom. As with the pre-focusing stage, this presents an energy-consuming approach to solve a problem that could also be addressed passively, by altering the solution density, for instance, so that particles are levitated by buoyancy. However, we note that nothing in our design precludes such density-controlled levitation, and that doing so is itself not without flaws. Increasing the density, usually by the addition of a heavier solute to the fluid, tends to increase the viscosity as well, leading to higher pressures and drag coefficients inside the chamber. Since the electrical approach circumvents this problem, it is preferred in moderate to low conductivity operation, where the additional power dissipated by the device is not significant.

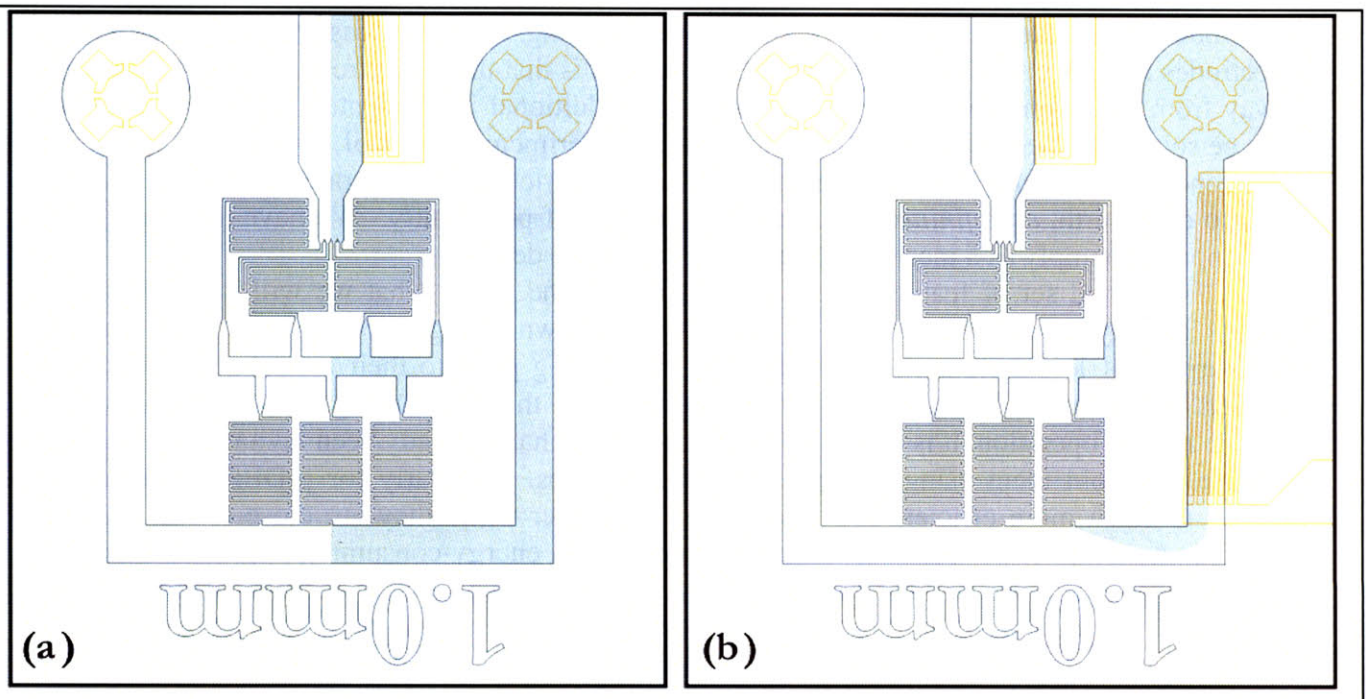

Figure 3-2: Prefocusing stage

Schematic description of prefocusing, with shaded regions representing fluid containing particles to be separated. In the absence of focusing electrodes (a), particles are spread across half of the device. With these electrodes (b), it is possible to confine cells to a smaller fraction of the total chamber width.

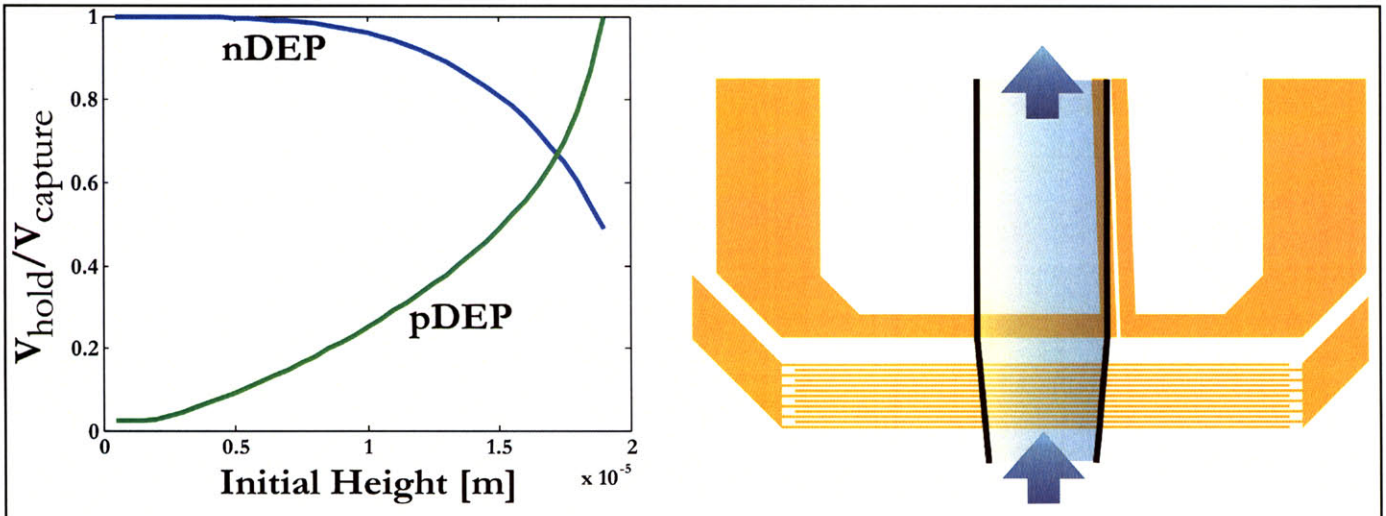

Figure 3-3: Prelevitation stage

Concept behind the pre-levitation stage. Holding particles that have reached their steady state positions (i.e. the channel ceiling for nDEP and the channel floor for pDEP) requires less energy than entraining particles at the appropriate height (graph on left). Interdigitated electrodes (right) are therefore used to force particles closer to their steady state heights before reaching the separation barrier.

3.2 Mask Design and Layout: Flow Chambers

The three types of flow chambers we created, corresponding to the three widths discussed previously, are shown in Figure 3-4. Since we have already discussed the rationale behind the widths, we will focus instead on other features. The use of a two-stage diffusive mixer is motivated by the relatively low Peclet number the device is designed to operate at; for much of the separation chamber's length, the only non-vanishing mode of the conductivity gradient is the first and most slowly decaying one. Since this is true regardless of the conductivity profile at the inlet, we limit the design to two stages to minimize the total pressure drop across the device and the device's total footprint. The mixer was originally designed anticipating a chamber height of 20 μm and flowrates of around 3 $\mu Lmin^{-1}$, for which the residence time of fluid in each mixer stage (LU^{-1}) exceeds the characteristic time for diffusion ($\sim w^2/4D$) several times over when a serpentine channel of width 40 μm and total length 1cm is used. These dimensions also (in practice) prove satisfactory for mixing under more stringent conditions, such as with a lower chamber height at the same volumetric flowrate.

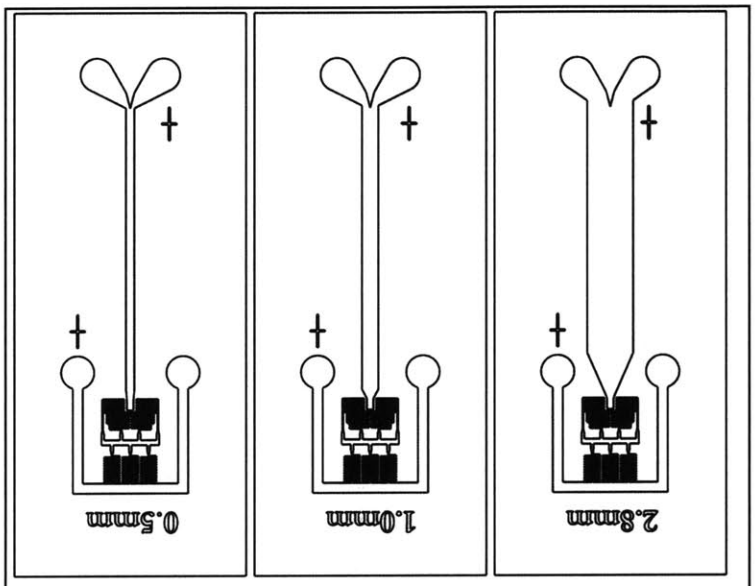

Figure 3-4: Flow chamber masks

Channel widths are (from left to right) 0.5mm, 1.0mm, and 2.8mm devices.

We also decided to limit the number of outlets on the device to two; this simplified the packaging and use of the device during the preliminary stages of evaluation, covering the scope of the work for this thesis. Despite the use of only one or two outlets, we are still able to extract information from the device using the optical techniques discussed in section 4.3. In future designs, when actual sample collection comprises a greater component of the overall goal, more outlets may be added with no conceptual change to the device design.

3.3 Materials and Fabrication: Electrodes

With masks for both electrodes and microfluidic structures in place, we shift attention to microfabrication. All components of the device were fabricated in MIT's Technology Research Laboratory, a class 100 cleanroom. A complete listing of processing steps and parameters can be found in the appendix. In the following discussion, we will place emphasis on processing steps that involved deviations from standard protocol and my rationale in selecting specific materials.

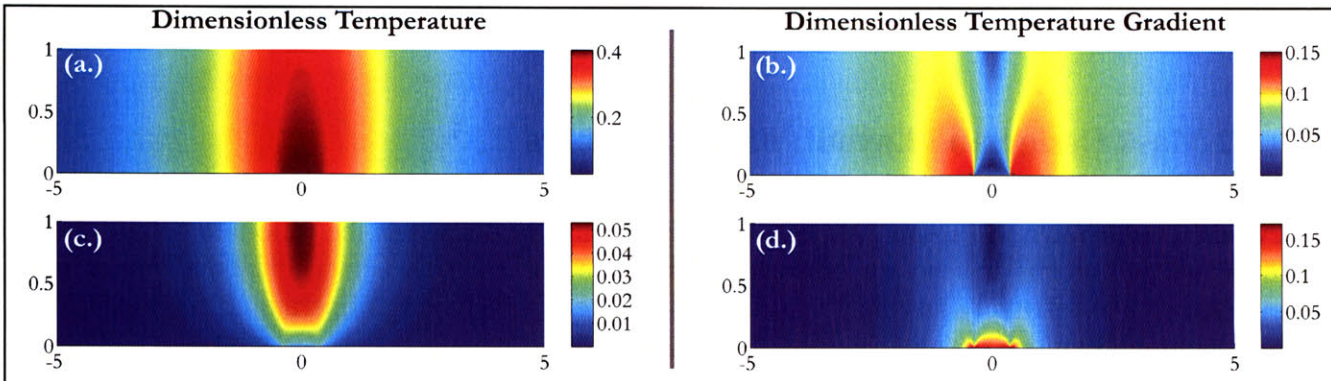

Figure 3-5: Temperatures and temperature gradients along the channel cross-section

Comparison of the (scaled) temperature profiles and temperature gradients produced under identical operating conditions with Pyrex ((a.) and (b.)) and silicon ((c.) and (d.)) substrates. Switching to a more thermally conductive substrate (in this case, from Pyrex to silicon) decreases the temperature substantially, but has little effect on the magnitude of thermal gradients.

We patterned the electrodes on 6" Pyrex wafers. The substrate material amounted to a choice between silicon, which has superior thermal properties, and Pyrex, which is electrically superior. The thermal conductivity of silicon is roughly two orders of magnitude greater than that of Pyrex [29]; accordingly, it is able to support a substantially higher heat flux, lowering the temperature rise within the channel. This is potentially advantageous for two reasons. First, extreme temperature rises can be deleterious to the health of microorganisms, mammalian cells more so than bacteria. Second, as we have already discussed, temperature rises change media properties, which can then induce flows. Because the target application of this device is originally bacterial cells, specifically *E. coli*, which are robust to variations in the temperature of their environment, we decide that the temperature rises produced in the device (<10K) with either choice of substrate should not be problematic. The choice between silicon and Pyrex is thus reduced to the mitigation of EHD flows (see sections 2.4 and 2.5). Figure 3-5 shows the scaled temperatures and temperature gradients produced under identical operating conditions with Pyrex and silicon substrates. While silicon reduces the maximum temperature rise by nearly an order of magnitude, it does not reduce the magnitude of the temperature *gradients*, which are ultimately responsible for EHD flows. This, combined with the excellent electrical insulation it provides, motivates us to choose Pyrex as a substrate material.

To create the electrodes, we used a standard liftoff process. Liftoff enabled the use of gold as the electrode metal without necessitating etchants that are not widely available. Gold is well suited to devices which need to interface with cells and fluids as it is biocompatible and does not tend to corrode. The process begins with a 10 minute clean of the Pyrex wafers in a Piranha solution (1:3 H_2O_2:H_2SO_4), followed by a rinse with DI water and spin dry. We then dehydrate the wafers at 150°C for 20 minutes, prior to a vapor-phase deposition of the adhesion promoter Hexamethyldisilizane (HMDS). Next, we coat the wafers with AZ5214 photoresist, and expose them in accordance with an image reversal process. This involves coating the wafer with resist (ramp to a final spin speed of 3000 rpm), pre-baking (30 minutes at 90°C), exposing with the mask (2.3 seconds at 10 mW/cm^2/s, 365-405nm), post-baking (30 minutes at 90°C), and flood-exposing (60 seconds at 10 mW/cm^2/s, 365-405nm) to reverse the polarity of the

photoresist. After developing for 70s in AZ422 developer, the wafers are bare where electrodes are to be deposited and covered in photoresist everywhere else.

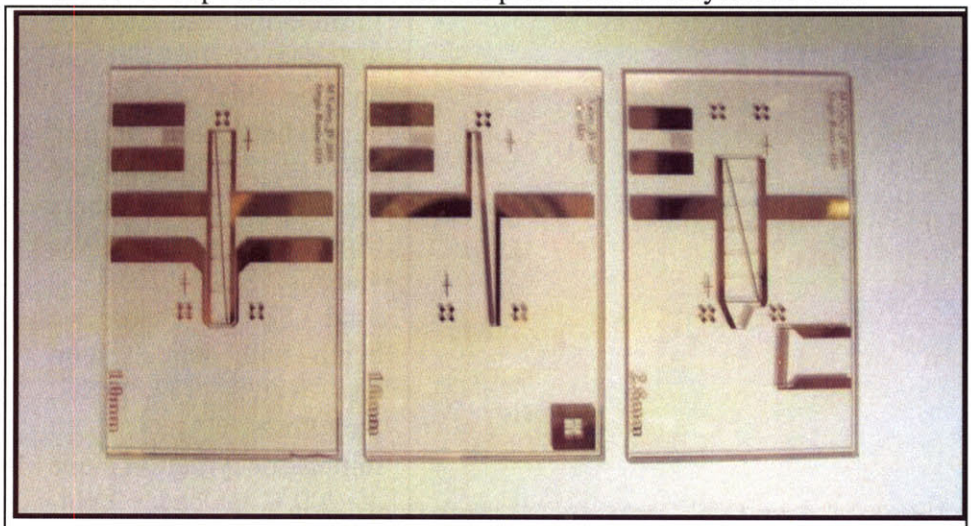

Figure 3-6: Photograph of dies prior to further packaging.

In our experience, the pre- and post-bakes proved to be the most sensitive steps in fabricating the electrodes. We used a convection oven for these bakes, which was shared with other users of the facilities. When the oven was opened in the middle of one of these steps, it was often the case that the process would be compromised, with some areas of the wafer never developing. Additionally, orientation of the wafers with respect to air flow in the oven seemed to make a difference, with best results obtained when the wafers were parallel with the flow. These observations are largely speculative, and have not been rigorously tested; I provide them only as empirical guidelines for practices that seemed to mitigate lithography problems.

After lithography, we use electron beam (e-beam) deposition to cover the wafer with a 100′ layer of titanium, followed by a 2000′ layer of gold. The titanium serves as an adhesion layer, securing the overlying gold to the substrate. We then soak the wafers in an acetone bath overnight to remove the photoresist and the metal on top of it. Any loose gold is removed by placing the wafers briefly in an ultrasonic bath. It remains only to separate the wafer into individual die. In preparation for this, we coat them with a protective layer of photoresist (final spin speed of 600rpm). A photograph some of the final die is shown in Figure 3-6.

3.4 Materials and Fabrication: Flow Chambers

The flow chambers in my device are made from PDMS, using standard soft lithography techniques, as described in [34]. For the master mold, we patterned a silicon wafer with the epoxy-based, negative photoresist SU-8 (MicroChem, Newton, MA). SU-8 is a rigid, durable resist that is available in a wide range of viscosities for layer thickness ranging from one to hundreds of microns. This versatility facilitates the fabrication of a range of heights, simply by varying the formulation of the resist and the spin speeds.

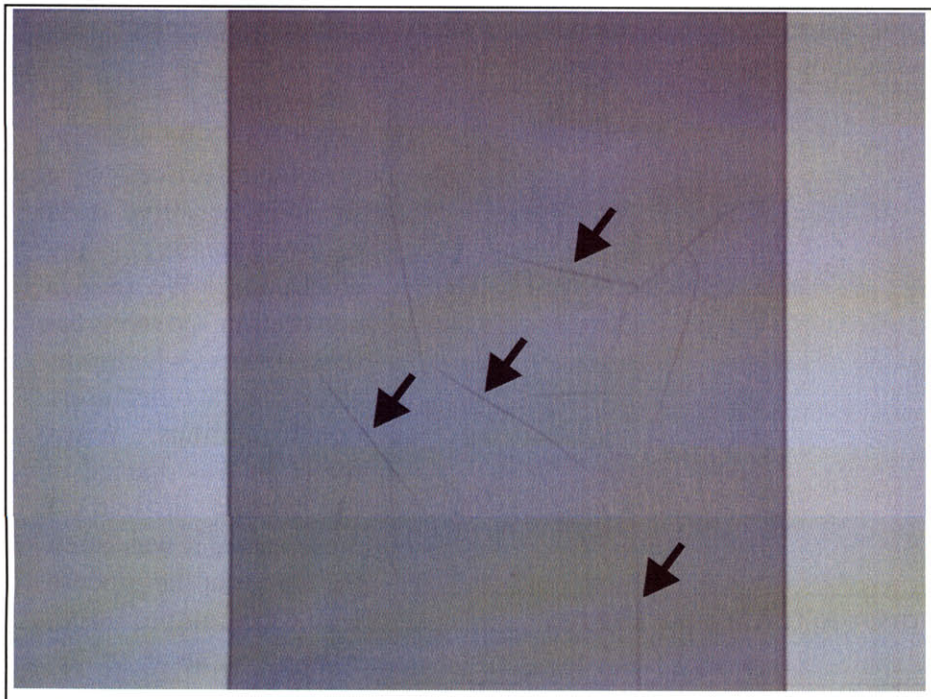

Figure 3-7: Surface imperfections on the SU-8 molds

These scratches are believed to be caused by the stress induced by the cross-linking of the film.

Different process parameters and resist formulations are used for different targeted chamber thickness. For a target height of 20 μm, SU-8 2015 is used, while for all thinner chambers (8 μm to 12 μm), the less viscous SU-8 2010 is used. In all cases, we begin with bare silicon test wafers (WaferNet, San Jose, CA). A 30 minute dehydration bake at 200°C precedes spin-coating the wafers at final spin speeds of 2250, 1750, and 3000 rpm for layer thickness of 20, 12 and 8 μm, respectively. To prevent the accumulation of resist on the edge of the wafer, a swab coated with acetone was held at an angle with respect to the edge of the spinning wafer. In patterning the wafers, the soft-bake and post-expose bake seem to be critical steps. For the soft-bake, we place the coated wafers on a hotplate at 60°C and immediately turn it up to 95°C. After the plate has equilibrated at this new temperature (typically 5-10 minutes), we allow the wafer to bake for an additional 2 to 5 minutes, depending on the layer thickness. Immediately afterwards, we turn off the plate and wait for it to cool to at least ~50°C before removing the wafer. The wafers are then exposed (soft contact) for 8 to 12 seconds at a dosage of 10 $mW/cm^2/s$ and 365-405nm. Even with the precautions taken with edge-bead removal during the spin-coat and the substantially longer soft-bake times, the wafers would often stick to the mask during exposure. Generally, the point of contact was limited to the wafer's edge, and we could remove the wafer without damaging the SU-8 film or needing to clean the mask between each exposure. We proceeded with the post-expose bake in much the same way as for the soft-bake, ramping the temperature slowly from 60°C to 95°C, sustaining it at this level for 2 to 5 minutes, and then cooling the plate and wafer to roughly ambient. It was during the post-expose bake that we encountered the most difficulty; the cross-linking film would often become stressed to the point that scratches would appear on the surface of the resist (Figure 3-7). Following the post-expose bake, the wafers were developed in PM acetate for 3 minutes, followed by a final spin during which we sprayed the wafers with first PM acetate, then isopropanol, and finally allowed to spin dry.

The final results of this process were SU-8 molds of roughly the prescribed thicknesses. The nominally 20 μm wafer contained chambers with heights between 17.8 and 18.9 μm, while the thinner chambers were generally within 5% of the target thicknesses. The limiting factor on

yield was the aforementioned surface roughening more than anything else. While this challenge was never fully overcome, we were able to alleviate it to the point that ~30% of the molds on any particular wafer would be nearly devoid of these scratches. Attempts to measure the topology of these surface imperfections suggest that they have little impact on the uniformity of the channel ceiling. We subjected both the original molds and PDMS casts to scans with a stylus profilometer, and detected no changes in topology associated with scratches. While in the case of the SU-8 mold, this may be attributable to the disparity between the relative sizes of the stylus (large) and the scratches (small), the absence of any protrusions detected on the PDMS cast suggests that they do not appreciably transfer to the microfluidic chambers. In support of this, we have not observed any disturbance to fluid streamlines or particle trajectories in subsequent experiments that could be attributable to these imperfections. We conclude that the molds are satisfactory for our purposes, and prepare them for use by silanizing them; this entails placing them under vacuum with a small volume of HMDS for about 40 minutes. The HMDS prevents the PDMS from bonding irreversibly to the silicon wafer when the chambers are cast. This process and the eventual integration of electrical and fluidic components are discussed in chapter 4.

Chapter 4: Materials and Methods

Before we can proceed to characterize the device, some additional issues must be resolved. First, we must package the device so that it interfaces with the outside world in a way that is both facile and reliable. Next, we must define standard operating procedures for performing IDS, as well as for quantifying performance. Since the data we collect from the device is an inextricable function of both the device and the particles we put into it, deconvolving the characteristics intrinsic to the device necessitates a comprehensive understanding of the particles. These three objectives – developing schemes for packaging, data acquisition and processing, and characterizing particles for metrology – comprise the discussion of this chapter.

4.1 Packaging and Test Setup

Packaging the device in a way that was both reliable and easy to work with was one of the greatest challenges in this project. Material and processing selections that were chosen to optimize ease and reliability of fabrication often had the opposite effect on device packaging. In the following section, we will outline how we have dealt with the challenges faced in going from a diced wafer to a device ready for testing. We place special emphasis on those steps that proved especially challenging, or that, when done incorrectly, are believed to limit the performance of the device.

4.1.1 Assembling the electrodes and fluidic chamber:

Once we have removed the wafers from the MTL facilities, we begin packaging the devices by drilling fluidic access holes into the Pyrex die, using 0.75-mm-diameter diamond drill bits (C.R. Laurence Co., Inc., Los Angeles, CA). We leave the thin coating of photoresist left over from the dicing step on the die for protection. After the holes have been drilled, the photoresist is removed with acetone and the chip cleaned with methanol and isopropanol. In some cases, the die is then coated with Sylgard® Prime Coat (Dow Corning, Midland, MI), by the same protocol described in [32]. This step is designed to promote the eventual bonding of the fluidic chamber, especially over metal regions of the chip, where bonding is otherwise not possible. This surface modification has also been found to reduce non-specific adhesion of particles to the

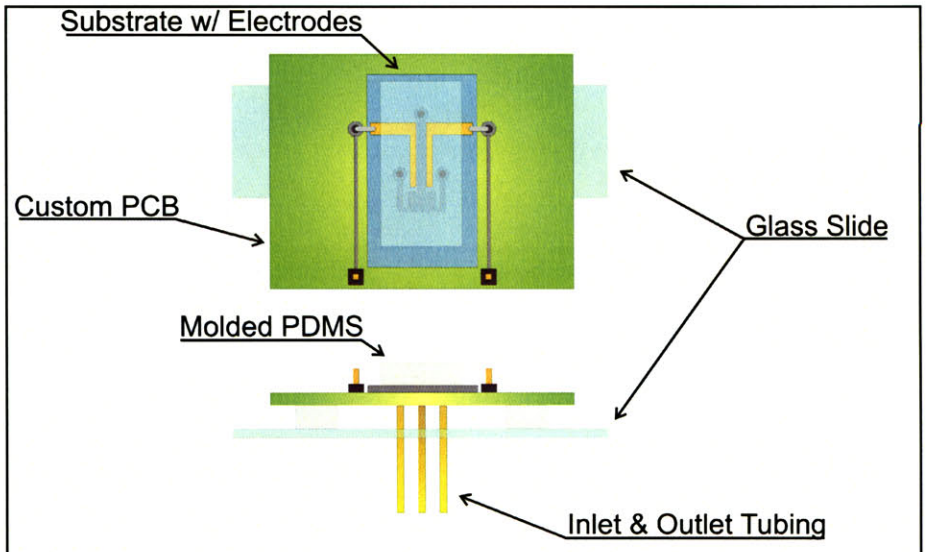

Figure 4-1: Schematic of the packaging scheme.

substrate. After cleaning and surface modification, the chips are placed in an oven at 65°C to dehydrate prior to bonding.

In parallel with the preparation of the electrodes, we cast the molds for the microfluidic chambers. For this, we pour ~100g of PDMS at a ratio of 10:1 base-to-curing agent, mix thoroughly, and allow the viscous solution to degas for ~30 minutes. We pour the PDMS on to the HMDS-treated SU-8 master and allow it to cure for about two hours, after which we peel the PDMS from the master and divide it manually with a sharp knife into individual chambers. Owing to the thinness of the chamber (<20 μm), the macroscopic alignment marks designed to aid in registering the chamber to the electrode chip are difficult to see. To facilitate alignment, we color over the marks with black marker prior to cleaning the chamber with tape. This removes all excess ink not recessed into the PDMS, leaving the surface clean and the alignment marks visible. We are now ready to bond the chamber to the substrate.

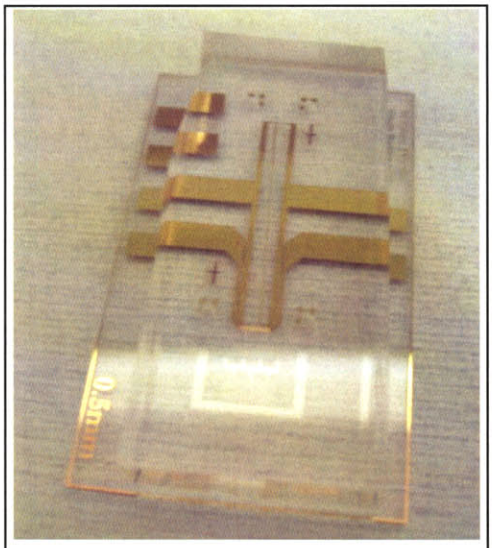

Figure 4-2: Photograph of a bonded device

The PDMS chamber and the glass-gold substrate are exposed to air plasma for one minute (PDC-001, Harrick Plasma, Ithaca, NY). This oxidizes the surface, causing the two exposed faces to bond spontaneously when brought into contact. It must be noted that the PDMS does not bond to untreated gold features; this is why we sought to minimize the gold surface area in the vicinity of the channel's walls, especially prior to the mixer, where the pressures are especially high. By doing this, we are able to create leak-free interfaces at all pressures of interest. Indeed, it is found that, under excessively high pressures (>1 atm, corresponding to over 20 times the flowrates we would commonly use), the first point of compromise is generally the mixer, rather than any gold-PDMS interface. After the device has been bonded, it is placed in an oven at 65°C overnight, to allow the bond to set. This is empirically found to strengthen the bond. A photograph of a bonded device is shown in Figure 4-2.

This bonding step, particularly the alignment of the chamber to the electrodes, is especially critical. It is performed by hand, in the absence of any magnification, and is thus a primary source of variability from device to device. Roughly, we are able to align the bond to within ~200 μm of center laterally, and to within ~2° of the target angle. While lateral misalignment was anticipated and accounted for in the mask design and is thus not a significant problem, misalignment of the angle of the chamber is more difficult to compensate for. With all other parameters held constant, and at small angle variations, the device's performance is roughly linear in θ, the angle of the electrodes with respect to the direction of flow. If the electrode angle is 6° instead of 4°, for instance, it will be ~50% less effective. At an angle shallower than the target, the device will be more sensitive, but it may not have access to the full width of the channel. In cases where either of these misalignments occur, we remove the PDMS, clean the device, and attempt the bond again with a fresh chamber.

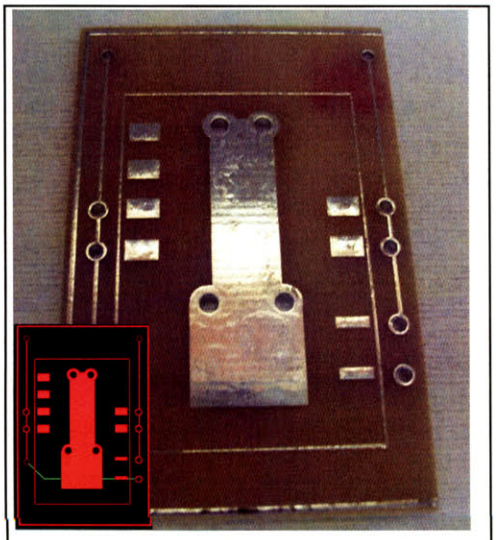

Figure 4-3: Representative PCB and schematic (inset).

Given the sensitivity of the device's performance on alignment, it is perhaps not surprising that the removal of bonded PDMS became a common occurrence throughout this project. Besides poorly aligned channels, removal of the PDMS was also necessitated by fouling of the device after several uses. To do this, we placed the bonded chip and PDMS in heptane, which dramatically swells the PDMS, causing it to separate cleanly from the substrate. The PDMS is discarded, and the electrode chip is cleaned with Nanostrip (Cyantek Corp., Fremont, CA), rinsed, and dehydrated. It is then once again ready for bonding. Following this protocol extended the lifetime of the electrode chips considerably.

4.1.2 Printed Circuit Board (PCB):

The next packaging step is to secure the device to a PCB. The purpose of the PCB is to facilitate making electrical and fluidic connections to the device, while permitting observation of the device during operation. A schematic and photograph of one type of PCB that was used are shown in Figure 4-3. The PCB contains metal plating beneath where the chamber is located to block the autofluorescence of the PCB itself. This is vital, as the broadband emission spectrum of the PCB would easily overwhelm fluorescently-labeled particles flowing through the device. The metal sheet is a convenient alternative to drilling the PCB out from under the chamber. We also make PCBs without this plating for instances in which we would like to view the device under bright field, which would be strongly reflected by the metal. For fluidic connections, the PCB contains holes aligned with those of the chip where 1/16"-outer-diameter, 0.007"-inner-diameter PEEK tubing (1536, Upchurch, Oak Harbor, WA) is inserted. We seal the tubing to the back side of the PCB using High Performance Epoxy (Loctite Inc., Rocky Hill, CT). With the tubing in place, we attach the chip to the PCB, again using PDMS mixed 10:1 to paint around the tubing, isolating each inlet and outlet. We use PDMS in place of more conventional epoxies to minimize background fluorescence; alternative means of sealing the device were found to have considerable broadband emission spectra. The chip is then lowered onto the board and adjusted until there is a uniform seal between the PCB and chip fully surrounding each access hole. For the electrical connections, Conductive Epoxy (ITW Chemtronics, Kennesaw, GA) is used to attach wires to the chip which are then soldered to the through-holes on the back side of the PCB. Finally, pins are soldered into the PCB, for attaching an external function generator to the device.

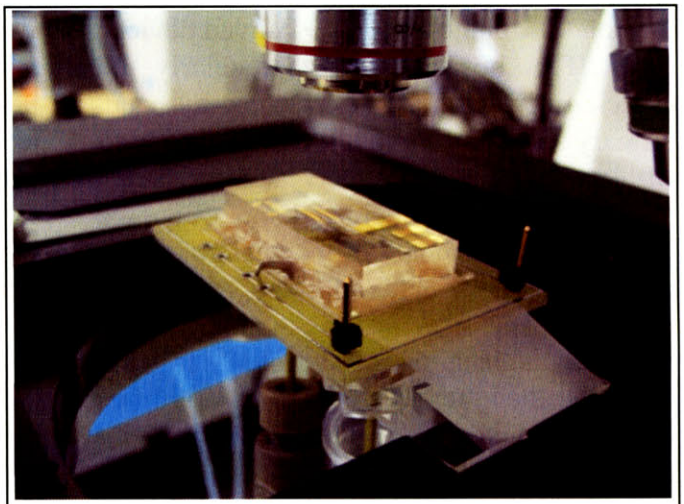

Figure 4-4: Photograph of the packaged device placed on the microscope stage for observation.

At this point, the device is ready for integration into the test setup, shown schematically in Figure 4-5. This consists of a plastic base fastened to two four-way valves (V-101T, Upchurch Scientific, Oak Harbor, WA), to which three syringes connect: two for the high and low conductivity solutions with the accompanying sample particles, and a third, which is used to flush the device before and after use, where desired. By adjusting the valves, the inlets may be set to receive either the distinct conductivities, or the common wash solution. From the valves, tubing connects directly to the device's two inlets, using Upchurch unions and ferrules. The device is mounted on a glass slide which clips directly into the microscope stage, facilitating real-time observation of the device (Figure 4-4).

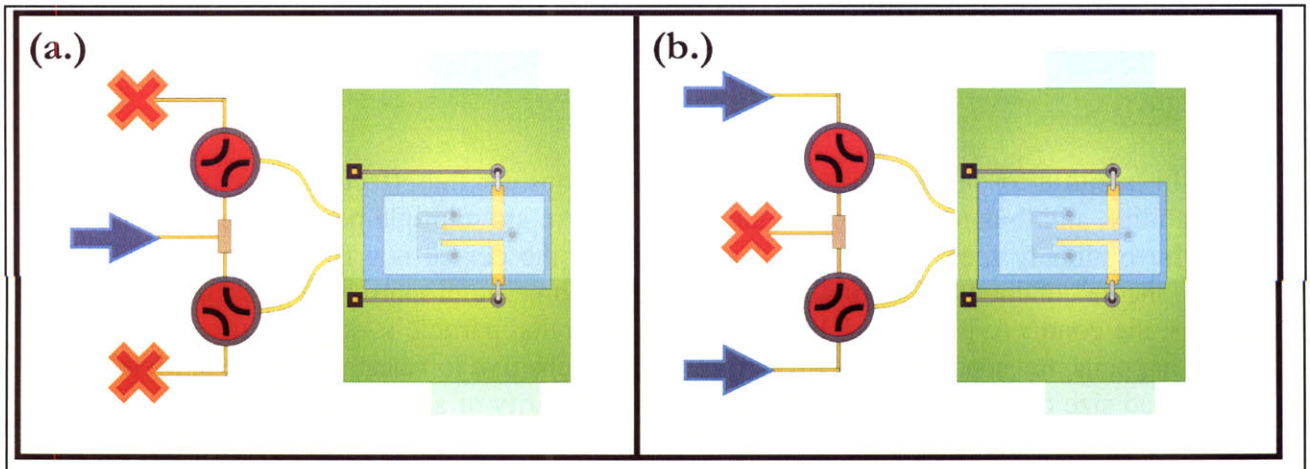

Figure 4-5: Schematic of the test setup used for the device.

4.2 Test Particles

With packaging complete, we shift our attention to the particles we will use to characterize the device. While IDS was originally conceived as a tool for separating *E. coli*, these cells are suboptimal as tools for characterization. The precise electrical characteristics of bacterial cells are largely unknown and highly variable. Additionally, these cells exhibit some of the characteristics, discussed in section 2.5, for which we saw IDS to be particularly challenging: small and broadly distributed sizes across a population (relative to other cells, such as yeast), and high conductivity (since the separation is based upon differences in cytoplasmic concentrations of polymer). To facilitate the collection and analysis of data, we initially seek particles over which we have greater control. The characteristics of the ideal test particle depend in large part on which aspect of the device we are interested in characterizing. Since the polarizability of a particle is dependent on both its size and its electrical properties, these two characteristics are of particular interest. Here, we discuss some considerations with regard to them both.

4.2.1 Electrical properties:

The electrical conductivities of widely available materials, from glasses to metals, span roughly 20 orders of magnitude. In contrast, we are interested in separating particles whose conductivities vary by ~10%. We further require that this small difference in conductivity fall comfortably in the range of conductivities easily achieved in aqueous solutions. Generously defining this range as from 5.5×10^{-6} Sm^{-1} (ultra pure DI water at neutral pH) to ~1.6 Sm^{-1} (the

approximate conductivity of phosphate buffered saline), we immediately eliminate the use of many materials based on their bulk properties; most dielectrics have bulk conductivities below the limit of DI water, and particles with even very thin metal coatings will generally have effective conductivities in excess of the upper bound for aqueous solutions. We approach this problem in essentially two ways. First, although the *bulk* properties of materials generally lie in an unfavorable range for IDS, it is possible to chemically modulate the *surface conductance* of many dielectric particles through the addition of charged groups. For sufficiently small particles, these surface effects contribute significantly to the overall electrical properties. The second approach we adopt in the development of tools for metrology is the use of vesicles. Here, we overcome the conductivity restrictions of aqueous phase solutions by using particles which themselves consist largely of a well-defined electrolytic solution.

4.2.2 Size:

In addition to electrical properties, we must consider the effects of size on a particle's polarizability, and thus its behavior in our device. There are multiple perspectives on this issue. As we have already seen, the predicted sensitivity of the device is a function of particle size, voltage, media conductivity, and other material and geometric properties. For sufficiently small particles, the conductivity at the IDP will diverge from that particle's iso-dielectric conductivity. As this happens, the separation becomes increasingly sensitive to variations in the particle's size. Thus, broad size distributions will tend to degrade the purity of any separation targeting specific conductivities that have no correlation to size. In this sense, device characterization becomes difficult when conductivity differences become entangled in size differences; this would encourage us to seek monodisperse particles. However, the robustness of the device depends on its ability to reject these variations in size; without simultaneous variability in both size and conductivity, it is impossible to say which feature, if either of the two, is most responsible in determining a particle's IDP. Accordingly, polydisperse particles provide an avenue for measuring the robustness of the device, and its relative sensitivities to conductivity and size.

The simultaneous constraints imposed on particle selection by both electrical properties and size are therefore reconciled by testing the device with a combination of commercially available, monodisperse particles, the conductivity of which are modified with surface charge, and vesicles, which we create in our lab to precise conductivity specifications, but with little control over the size. In the following sections, I will discuss the theoretical behavior of both of these particles, as well as some measurements taken to characterize their properties.

4.2.3 Polystyrene Beads:

The first type of test particle we use are polystyrene beads. While bulk polystyrene is itself quite insulating, at the sizes of interest to us (~1 μm), surface effects can often dominate those of the particles' bulk, volumetric properties [35].

The origin of this surface conductance is fixed charge in the bulk or on the surface of the beads. This charge exerts an electrostatic attraction (repulsion) on the mobile counter-ions (co-ions) in the external solution which balances the ions' tendency to diffuse, creating a small region in which there is a net space charge density. In this region, the counterion concentration can be many times that of the bulk, charge-neutral, solution. Since conductivity is related to ionic concentration by equation 2-2, this thin layer of enhanced counter-ion concentration is

highly conductive. Despite the fact that it is generally on the order of 1-10nm thick, it is in many cases the dominant determiner of a particle's electrical properties.

While much work has been done developing models for the electrical properties of charged particles in ionic solutions [35, 36], it remains an active area of investigation. For the interests of this project, a relatively simple model is adopted, which proves to be at least modestly predictive. In equilibrium, in the absence of convection or an externally applied electric field, the Boltzmann distribution relates the ion concentration to the electric potential:

$$c_i = c_0 e^{-z_i \frac{q\phi}{kT}} \tag{4-1}$$

And thus for the conductivity, we have from equation 2-2:

$$\sigma(r) = F c_0 \left[u_+ e^{\frac{z_+ F\phi}{RT}} + u_- e^{\frac{z_- F\phi}{RT}} \right] \tag{4-2}$$

The fact that the conductivity is radially symmetric follows from the fact that we have neglected the deviations from equilibrium caused by flow and applied fields around the bead. We can simplify this expression further by using local rectangular coordinates, $x = r - R$, justified by the fact that the Debye length is orders of magnitude smaller than the particle radius, R. The electric potential can be solved for using the Poisson-Boltzmann equation (see, for example, [21]) and substituted into equation 4-2 to give the spatially-varying conductivity in the vicinity of the bead.

To go from the concentration of ions around the charged bead to a lumped value for that bead's effective electrical properties, we model the particle as being comprised of an insulating polystyrene core covered by a conducting membrane with a thickness of one Debye length. We can then average the conductivity over this thickness to define the lumped membrane conductivity. Linearizing the expression for the lumped conductivity of a layered particle, we obtain the following:

$$\sigma_p \approx \left[\frac{\left(\frac{R+\delta}{R}\right)^3 - 1}{\left(\frac{R+\delta}{R}\right)^3 + \frac{1}{2}} \right] \sigma_s \approx \frac{2\delta}{R} \sigma_s \tag{4-3}$$

In the above, we have set the conductivity of the bulk polystyrene equal to zero.

This model for the effective conductivity of a polystyrene bead has several noteworthy characteristics. First, we notice that it varies as the inverse of the particle radius, R. This reflects the significance of surface effects (manifested by the surface conductance $\delta\sigma_s$) relative to volume effects, which are taken to be zero in this case. A very large particle will have an effective conductivity identically to that of bulk polystyrene. This suggests that, with media and surface chemistry held constant, a larger particle will have a lower conductivity than a smaller one. A second feature worth noting is the dependence of σ_p, the particle conductivity, on the media conductivity, σ_m. From equation 4-2, we see that σ_s is proportional to the bulk media electrolyte concentration, c_0, which is in turn proportional to the media conductivity, as seen from equation 2-2. Furthermore, the Debye length, δ, can be shown to vary as $c_0^{-1/2}$ for a binary, 1:1 electrolyte. This suggests that the particle conductivity will vary as the square-root of the media conductivity.

We can show this explicitly by following [36] and approximating the conductivity throughout the double layer as equal to the conductivity at the surface of the particle. Determination of the surface potential, ζ, will then give the particle's effective conductivity. Ignoring the contributions of co-ions to the surface conductance, and assuming that co- and

counter-ions have approximately equal diffusivities, we can rewrite the particle conductivity of equation 4-3 as:

$$\sigma_p \approx \frac{\sqrt{D\varepsilon_m \sigma_m}}{R}\left[e^{(\zeta / v_{th})}\right] \qquad \textbf{(4-4)}$$

where v_{th} denotes the thermal voltage and ζ denotes the potential at the surface of the particle.

Before this model can be of any use to us, we must address some of its deficiencies. One obvious shortcoming is the indeterminate nature of some critical parameters. Specifically, calculation of the surface conductance requires knowledge of the surface potential. This information is not easily determined from first principles, and thus the model, as posed, is incomplete. We can mitigate this problem, to some extent, through measurements of the beads' crossover frequencies in different media. This is done by adding saline to de-ionized water to specified conductivities, suspending the beads of interest in these solutions, and placing them in a chamber over interdigitated electrodes. We then excite the electrodes at different frequencies in a binary search pattern until we converge at the frequency at which the minimal DEP response is seen. In some cases, we observe no crossover frequencies.

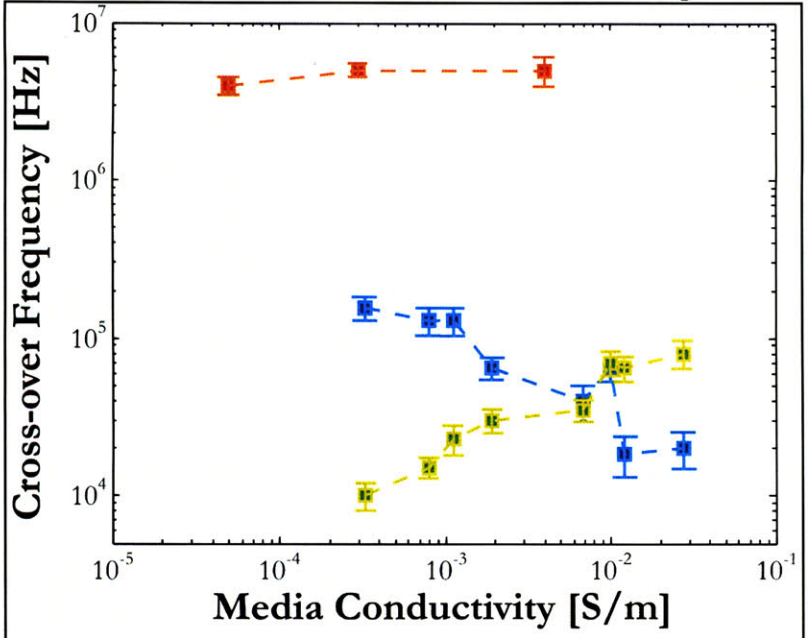

Figure 4-6: Cross-over frequency measurements

Cross-over frequencies for three types of beads: 1.25-μm-diameter (red), 1.60-μm-diameter (blue), and 1.9-μm-diameter (yellow-green).

We have repeated this process for a few different types of beads, with different sizes and surface chemistries. Originally, it was thought that the presence of surface modification would substantially influence the effective conductivities of the beads; this would be consistent with the theory described earlier, where a higher surface charge results in a larger surface conductance. However, measurements taken for beads of the same size with different surface modifications did not produce different crossover frequencies, to within the accuracy of the measurement. One possible reason for this is that the intrinsic charge of the surface, common to all beads and necessary to stabilize the colloid, is dominating the effects of the surface modification. However, since we are able to obtain test particles of repeatable electrical properties, we do not pursue the effects of surface modification further.

Figure 4-6 shows the results from these measurements for three types of beads, with diameters of 1.25 (red), 1.6 (blue), and 1.9 μm (yellow-green). In all cases, particles are observed to undergo p-DEP at frequencies below the dashed curves, and n-DEP above them. As expected, there is a range of media conductivities for which the particle's effective conductivity varies inversely with its size (equation 4-3), manifested by lower cross-over frequencies for

larger particles at a given media conductivity. Still, some unexpected behavior is observed, especially regarding the largest beads. For these, we observe cross-over frequencies which increase with increasing media conductivities over the range we have observed. To some extent, it is possible to explain this in terms of the surface conductance model of equation 4-4. Here, we have argued that the effective particle conductivity should vary proportional to the square root of the media conductivity. Substituting this into the real part of the CM factor and solving for the cross-over frequency gives us:

$$\omega_0 = \alpha\left[\beta^2\sigma_m + \beta\sigma_m^{3/2} - 2\sigma_m^2\right]^{1/2} \qquad \textbf{(4-5)}$$

where α and β are simply positive constants based on physical properties. For sufficiently low media conductivities, therefore, we would expect the cross-over frequency on a logarithmic scale to increase with a slope of ½. This is in very good agreement with the observed characteristics of the yellow-green line, which has a measured slope of 0.45 on a logarithmic scale. Of course, the definition of "sufficiently low" media conductivities depends on the values of α and β for a particular particle, and so we would not necessarily expect different particles to be in the same regime (i.e. ω_0 increasing or decreasing with σ_m) at the same conductivities. It is possible that all three curves would exhibit similar characteristics were we to measure their properties under a broader range of media conductivities.

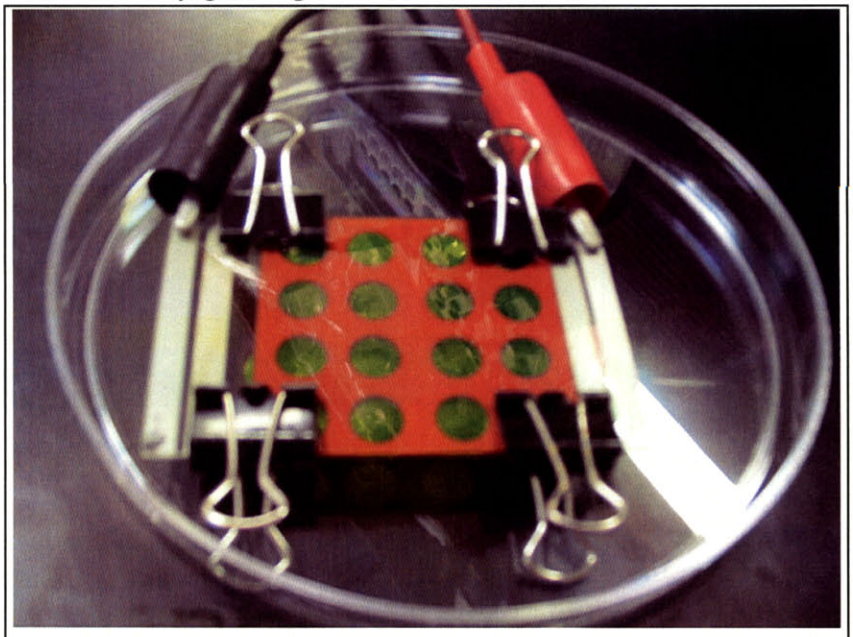

Figure 4-7: Electroformation jig

Apparatus for the electroformation of GUVs. (Photograph courtesy of Salil Desai).

4.2.4 Vesicles:

Vesicles are unilamellar, phospholipid containers with properties of interest to biologists and biophysicists [37], as well as engineers, especially in the development of methods for controlled drug delivery [38]. A common technique for the creation of vesicles is electroformation, described in [39]. Electroformation produces what are referred to as giant unilamellar vesicles (GUVs), which generally range in diameter from a few to hundreds of microns. We begin by depositing droplets of the lipid 1-stearoyl-2-oleoyl-*sn*-glycero-3-phosphocholine (SOPC) (Sigma-Aldrich, St. Louis, MO) diluted 10:1 in chloroform in 1-mm-deep silicone gaskets (P24744, Molecular Probes, Carlsbad, CA) adhered to an ITO slide. The slide is then placed under vacuum for ~30 minutes, to allow the solvent to evaporate, leaving each well coated with a dry lipid film. On top of this film, we pipette the solution we wish to entrain in the vesicles until each gasket is full. This solution can be mixed to a wide range of electrical conductivities or fluorescent intensities, although we observed that higher

conductivities produced fewer and smaller vesicles. On top of these wells, we secure a second ITO slide, so that the conductive sides face each other, and fasten the ensemble together with binder clips. A photograph of the apparatus is shown in Figure 4-7. A sinusoidal potential difference with a frequency of 10Hz and an amplitude of 1V is then applied across the ITO slides for two hours. The vesicles are then collected and prepared for use. Figure 4-8 shows images of vesicles produced in this manner.

Before the vesicles are ready to be flowed through the device, we must filter them, to eliminate the vesicles which are too large to pass freely through the device. This is done using a 10 μm, ultra-high molecular weight polyethylene filter (A-423, Upchurch, Oak Harbor, WA). Despite this precaution, vesicles significantly larger than the filter pore size do enter the device, possibly as a result of their ability to deform. The vesicles which survive filtration are still suspended in the media which they have encapsulated. Since this media will generally be of a different conductivity than we want and will contain the fluorescent salt used to facilitate observation of the vesicles, we must centrifuge them for 5 minutes at 2000 rpm and resuspended in them in media of the appropriate conductivity. Repeating this centrifugation step multiple times is essential to remove the of the background fluorescence as possible.

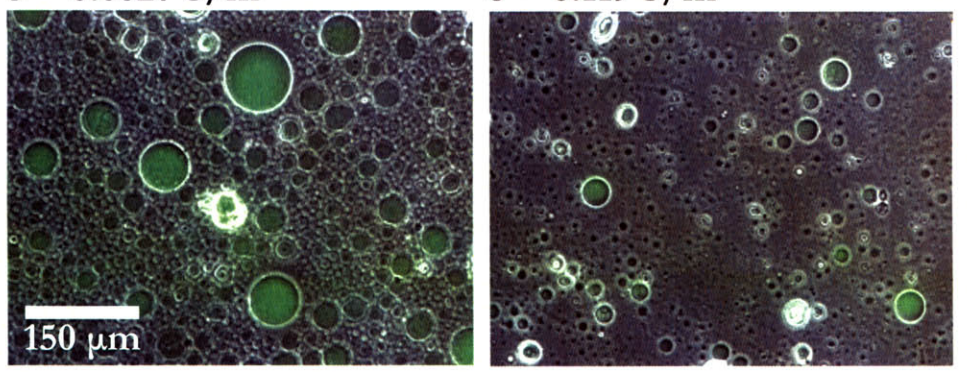

Figure 4-8: Vesicles

Vesicles created in media of different conductivity and ~50 μM fluorescein. Photographs are composites of phase and fluorescent images (courtesy of Salil Desai).

4.3 Electrical Characterization of Biological Particles

Beyond the characterization of our device, we are ultimately interested in the separation of biological particles. This requires detailed knowledge of the DEP spectra of these cells, and how they differ with viability and phenotype. In section 1.1, we described briefly how the heterogeneous structure of a cell can be lumped into effective electrical properties that will depend on the frequency of the applied field. We also argued that it is far more practical to attempt to arrive at these properties experimentally than by deriving them from basic physics. In this section, we will consider more quantitatively how specific characteristics of a cell change its electrical properties, how we measure these changes empirically, and how we generalize from these measurements to define protocols for separating different types of cells.

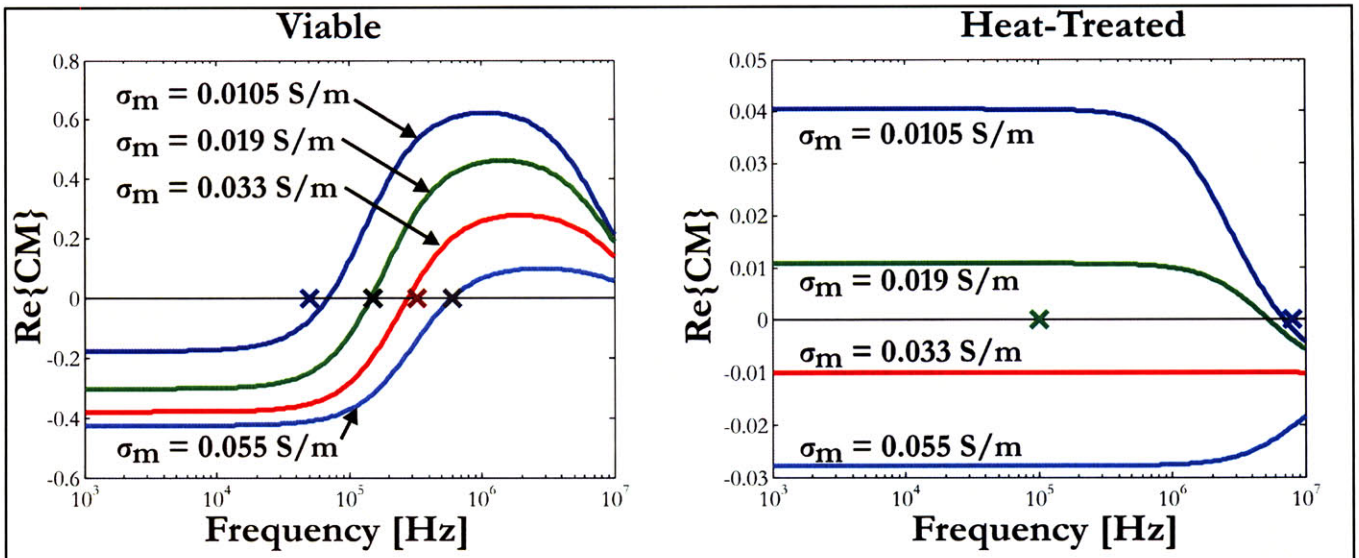

Figure 4-9: DEP spectra of yeast

Two-layer model for the DEP spectra of viable and heat-treated yeast cells, predicted from cross-over frequency measurements.

4.3.1 Yeast:

Separation of viable from non-viable yeast cells is a common application of microfluidic DEP systems, and so there is much literature regarding these assays and the electrical difference between live and dead cells [40, 41]. As a test for our device, we wish to attempt such an assay, obtaining non-viable cells by heat-treating a nominally live population. This involves placing ~1mL of cells in a flask on a hotplate set to 90°C for 20 minutes, after which the cells are washed in media of the appropriate conductivity and subjected to cross-over frequency measurements by the same method as for polystyrene beads. Given this data, we attempt to generate a predictive model for the dielectric spectra of both viable and non-viable yeast. As with the polystyrene beads, a Newtonian search is performed over a range of dielectric properties to determine those which best predict the observed dispersions. We model the cells as a two-layered particle, and the search is conducted in terms of a wall conductance and capacitance and a cytoplasmic conductivity and permittivity. For non-viable cells, we constrain the cytoplasmic permittivities and conductivities to match those of the media, consistent with the theory that the membrane has been compromised. Also, it seems appropriate from this perspective that the membrane conductance would increase and the capacitance decrease. The results of these measurements and our fit to the two-layer model are given in Figure 4-9.

Importantly, we do not expect this model to communicate any profound information about the physical structure of live and heat-treated cells; rather, we wish only to develop a predictive model for the DEP spectra of these cells. The underspecified nature of this problem implies that it is possible for our model to be predictive without being correct in its underlying details. We view this as a perfectly acceptable outcome, since our ultimate objective is simply to use these results to better plan our separations. Accordingly, our analysis suggests that a conductivity gradient ranging from about 0.05 S/m to about 0.01 S/m, at a frequency of a few hundred kilohertz would be appropriate for separating these cells.

4.3.2 *E. coli:*

We now shift our attention to the application for which IDS was originally conceived: the separation of *E. coli* based on intracellular concentration of PHB. As with yeast, we are exploiting the tendency of changes in the physical structure of cells to produce changes in electrical properties. Unlike yeast and our proposed viability assay, however, the physical differences we are targeting are now much more subtle. Granules of PHB internal to a cell are themselves subject to DEP forces. As we saw with the measurements of the DEP spectra for polystyrene beads, particles which have very low electrical conductivities in bulk may appear conductive when surface effects are dominant. It is therefore not trivial to predict how the presence of PHB will affect the dielectric properties of cytoplasm over all frequencies; at low frequencies, they may *increase* the apparent conductivity of the cytoplasm. Fortunately, we are interested only in high frequencies, for which the outer structure of the cell becomes electrically transparent, and we are probing the only the cytoplasm. We expect that at these frequencies (> 1 MHz), the dielectric spectrum of PHB in cytoplasm will be approximately independent of frequency, and will result in a decrease in the effective conductivity and permittivity of the cytoplasm.

Frequency	+PHB *E. coli*	-PHB *E. coli*
1 MHz	nDEP	nDEP
7 MHz	nDEP	CM~0
80 MHz	nDEP	pDEP

Table 4-1: Observed DEP behavior of +PHB and –PHB *E. coli* in a conductivity of 0.37 S/m.

This prediction is borne out by measurements of the cross-over frequencies of both wild-type *E. coli* (-PHB) and cells which produce the polymer (+PHB). Our collaborators in the Stephanopolous lab have developed multiple strains of *E. coli*, known to produce concentrations of PHB ranging from 1% of dry cell weight (DCW) to 55%±5% PHB DCW. In this thesis, we focus on the highest producing strain, pAGL20, and a control strain developed by the Stephanopolous lab, pAGL19, which produces no PHB. Table 4-1 shows characteristic measurements for these two strains, taken repeatedly over the past two years by both our lab and the Stephanopolous lab. We see that at a media conductivity of 0.37 S/m and frequencies in the vicinity of 10 MHz, +PHB and -PHB cells have different DEP responses to applied electric fields. In agreement with our hypothesis, +PHB cells have n-DEP affinity over a wider range of frequencies than their wild-type counterparts. This suggests that they do, in fact, have a lower effective electrical conductivity at these frequencies.

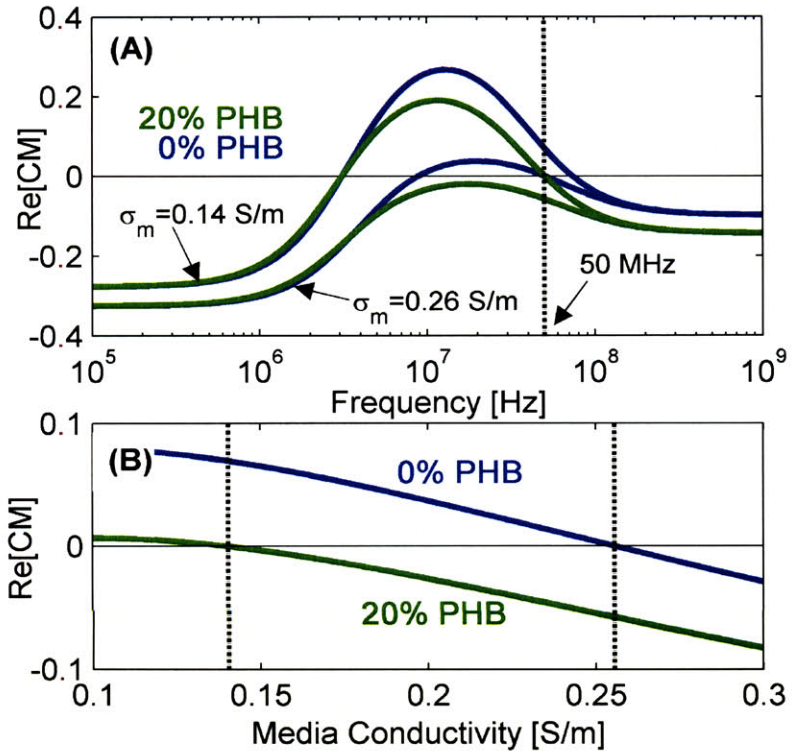

Figure 4-10: DEP spectra of *E. coli*

DEP spectra for –PHB *E. coli* (blue) and +PHB *E. coli* (green). This data suggests that we could perform a separation at frequencies from ~10-100 MHz and conductivities of around 0.3 S/m.

Figure 4-10 presents these results graphically, as predicted by an approach analogous to that used in modeling the DEP spectra of yeast (Figure 4-9). Producing and non-producing cells are indistinguishable at low frequencies, where the dielectric properties are predominantly determined by the cell's outer structure. At frequencies of around 10 MHz, the cell types begin to diverge, with producing cells undergoing n-DEP at lower conductivities than wild-type. Finally, at frequencies in excess of 100 MHz, the cytoplasmic permittivity is predominant. The low permittivity of PHB relative to cytoplasm assures that the two cell types will still be dielectrically distinct, but their behavior will no longer vary with media conductivity. This model suggests that IDS could be used to separate +PHB cells from -PHB cells using a conductivity gradient varying from around 0.3 S/m to 0.1 S/m at a frequency of around 10 MHz.

4.4 Data Acquisition and Processing

The final precursor to characterization of the device is the development of techniques for data acquisition and analysis. We have chosen to adopt an optical approach for ease of collecting data. An optical approach allows the testing of many experimental conditions in a short amount of time compared to what would be necessary if data were extracted from collected samples. Over the times that might be required to collect data for tens of experimental conditions on a single device, fouling would likely occur, via the gradual adhesion of particles to the chambers surface. This would make it difficult to meaningfully compare the results obtained early in an experiment to those obtained later. Not only would it take considerable time to collect the samples, but even then, they would likely be very small and difficult to work with. Essentially, we have decided to limit our focus at this stage in the project to characterizing the *intrinsic* properties of this method and architecture; the challenges associated with sample extraction, although certainly significant, are left unexplored in this thesis.

In accordance with our packaging scheme, the device is imaged using an upright scope. Under a 5× objective, we are able to view and record the entire width of a 1mm channel. This automatically preserves the positions of the channel walls as reference locations when we

analyze the videos. Data is collected by recording an area of the channel as near the outlets as possible. As shorthand, this original data file is referred to as a signal $x[m,n,k]$, where m is the row index, n is the column index, and k is the frame index. To extract the IDP of the particles from this signal, we first process the video to remove the (stationary) background. This amounts to the following operation:

$$\Delta[m,n,k-1]=\left(x[m,n,k]-x[m,n,k-1]\right) \tag{4-6}$$

The motion-filtered video is then thresholded (so that particles are not counted twice within a frame) and collapsed into a 2-D image:

$$y[m,n]=\sum_{k=2}^{K}\left[\Delta[m,n,k]\cdot\left(\Delta[m,n,k]>0\right)\right] \tag{4-7}$$

As shown in Figure 4-11, $y[m,n]$ represents the time-smoothed data, with the background removed by the simple low-pass filter of equation (4-7). The next step is to simply sum over the rows, m, and normalize:

$$c[n]=\frac{\sum_{m=1}^{M}y[m,n]}{\sum_{m=1}^{M}\sum_{n=1}^{N}y[m,n]} \tag{4-8}$$

The index of the IDP (N_{IDP}) is then straightforward to calculate:

$$\sum_{n=1}^{N_{IDP}}c[n]=\frac{1}{2} \tag{4-9}$$

Comparing this index to the indices of the channel walls, we can convert the IDP into a dimensional position along the channel's width.

While this algorithm has certain advantages – primarily, ease of use and computational simplicity – there are certain experimental conditions in which it is inadequate. The most limiting case occurs when the signal to noise ratio becomes very small, and the differencing filter becomes a very poor at rejecting background while preserving the moving particles. This is usually caused by biological samples that are small and have sensitive stains that photobleach easily. When the signal-to-noise ratio is too small, we resort to slightly more sophisticated motion filters. Subtracting out only the DC time-component (i.e. subtracting the average over k from each frame, then summing that to get $y[m,n]$) is effective in cases where the intensity of the particles is comparable to the noise level. In extreme cases, spatial filtering (in m and n) could be used on each frame prior to filtering in time (k); this further smoothes out noise, and if a bandpass filter is used, can filter out the background as well. These algorithms, while certainly more precise than that outlined in equations (4-6) through (4-9), are quite computationally expensive. Accordingly, they are generally not used.

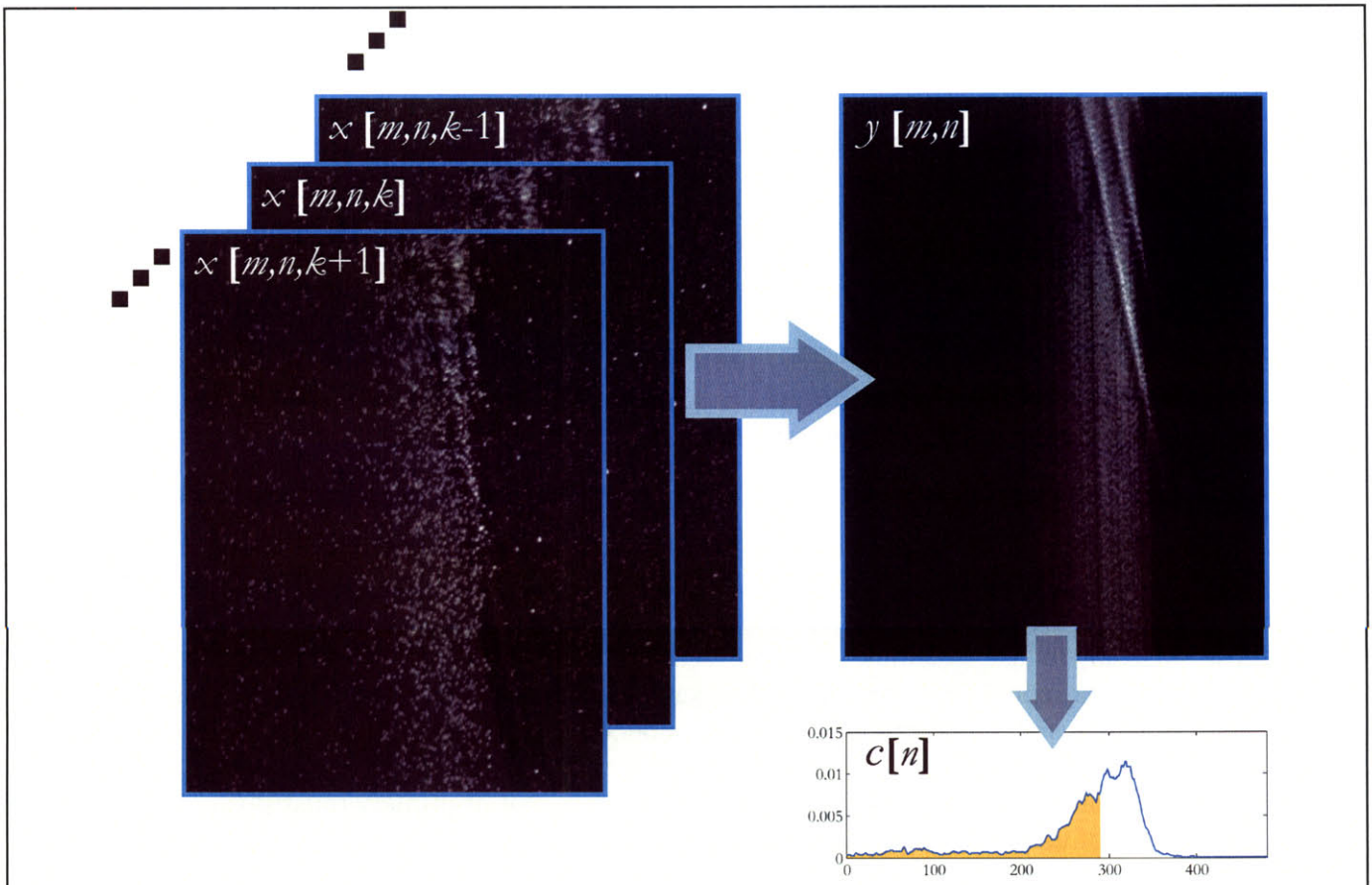

Figure 4-11: Image processing routine

Cartoon overview of image processing routine. Starting with the movie, $x[m,n,k]$, we apply the first-order motion filter and sum over k. The result, $y[m,n]$ is then summed over m, producing $c[n]$. The final reduction of dimensionality occurs by finding the "center of mass" of the cross-section, taken as the IDP.

Chapter 5: Results

In this chapter, I will discuss the results of some preliminary experiments that we have performed. We begin by considering the conductivity gradient created within the device, measured using quantitative fluorescence. From here, we proceed to look at the behavior of a single type of bead within the device, followed by the addition of a second type of bead and subsequent separation of the two. We will use the models developed in chapter 2, combined with measurements of the beads cross-over frequencies discussed in chapter 4, to interpret the trajectories observed for these beads. We then expand the battery of test particles to include operation of the device with vesicles, yeast, and *E. coli*. The chapter will conclude with discussion of some early experiments in flow visualization, designed to characterize the significance of EHD in the device under different operating conditions.

5.1 Gradient Verification

Verification of the concentration gradients established by the device is our first priority. One method for doing this, since it is gradients in electrical conductivity that we are ultimately interested in, is electrically. While techniques for doing this are well-established [42], we choose, instead, to use quantitative fluorescence [43]. While optical techniques restrict our measurement to concentrations of fluorescent species, which will generally have lower diffusivities than the saline comprising our conductivity gradients, they offer superior spatial resolution to electrical methods, and do not require the fabrication of additional test structures. Since we are constrained to work with a solute other than that of primary interest (i.e. NaCl), our objective is to use our device to try to measure the diffusivity of fluorescein. If our measurements and models combine to produce values for this diffusivity that are consistent with the literature, our confidence in our ability to create known gradients in other solutes will be increased.

In taking these measurements, we bond PDMS chambers to clean glass slides. We stamp access holes into the PDMS and insert tubing. High Performance Epoxy is used to seal the interface between the PDMS and tubing. We make multiple devices, so as to avoid reusing them; this mitigates the problem of diffusion of fluorescent molecules into the PDMS, staining the chambers. To asses the extent to which the chamber walls stain, we imaged a device as it was flushed with water, followed by fluorescein, followed by water again. No significant difference was noticed between the initial and final images, each at nominal fluorescein concentrations of zero. However, it is still possible that diffusion into and out of the PDMS is a problem at shorter time scales than were captured by this test.

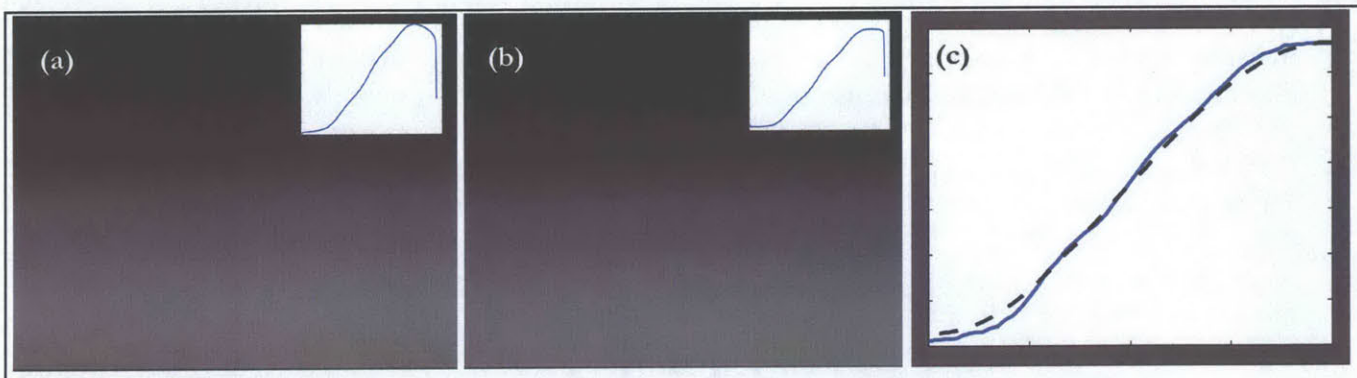

Figure 5-1: General sequence for image analysis of fluorescein gradients

The original image is cropped and rectified to obtain (a). We then divide out the microscope's response to a uniform concentration to obtain (b). Using the results from a calibration series, we convert pixel intensity into concentrations and fit to our model (c).

With the devices packaged in this way, we obtain a calibration series, to relate fluorescein concentration to fluorescent intensity in the device. The results of the calibration are then used to choose the range for the gradient. This is done by making sure that the highest concentration is outside of the saturated portion of the calibration curve, and the lowest concentration is above the noise floor. Consistent with this, we choose 3 μM and 10 μM solutions as the endpoints of the gradient.

Figure 5-1 depicts the sequence by which the images are processed. Beginning from an image of the channel at some point along its length, taken at a known flowrate, we crop and rectify the image, to assure that the Cartesian coordinates used in analyzing concentration gradients are registered to pixel rows and columns. The next step is to adjust for optical nonuniformities imposed by the microscope. This is done by dividing an image in which the intensity is uniform everywhere

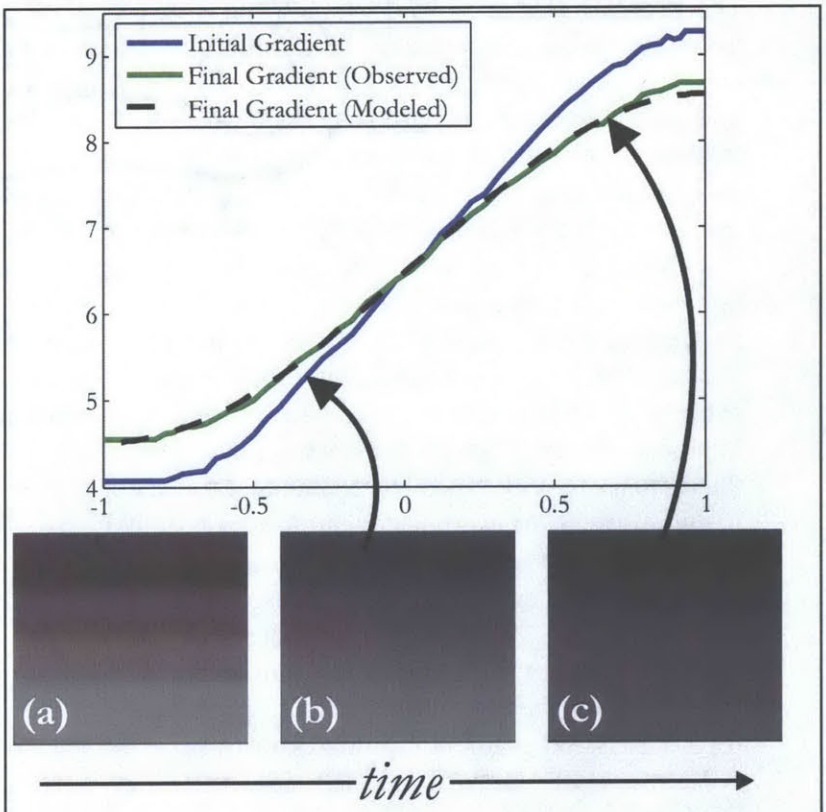

Figure 5-2: Determining the diffusivity of fluorescein from a transient measurement.

A convection-stabilized gradient is established (a), prior to stopping flow and plugging the outlet. The gradient then vanishes over time via molecular diffusion, as shown in the recorded images of (b) and (c). We fit the observed data to our model (dashed curve) to determine the diffusivity. A value of 5.33×10^{-10} m^2/s is obtained in this way.

inside the channel by an image taken of a uniform concentration, to obtain what we will call a transformation image. Because the microscope acts to some approximation as a lowpass filter, the intensity in the image of the uniform concentration decreases smoothly at the edges of the chamber, rather than suddenly transitioning from some high value to zero, as would happen in the ideal case. The transformation image, therefore, has high values at the edge of the chamber. These edge values are "stretched" further by raising the transformation image to a power such that, when it is applied to the gradient images, the change in intensity normal to the channel walls goes to zero. This forces the boundary conditions of our images to match those of the models to which we will be fitting them. We then smoothly interpolate the calibration data, and apply it to the image obtaining concentrations instead of fluorescent intensities. The final step is to enforce conservation of mass: the concentration integrated over all cross-sectional slices of the channel's width are forced to be equal.

The result of this processing is a matrix of concentrations that we seek to relate to our solution of the species conservation equation. For completeness, we include wall *effects in the* transport model, as described in section 2.1, page 25. The boundary value problem is completed by using a no-flux condition at the side walls and the measured upstream concentration at $z = 0$. The problem is then solved using spectral collocation, and the mean squared error between the measured outlet concentration and the model fit is computed. Newton's method is used to find the diffusivity that minimizes the error between measurements and the model. In this way, a diffusivity of 3.85×10^{-9} m^2/s $\pm$ 1.06×10^{-9} m^2/s is obtained, significantly higher than values reported elsewhere in the literature.

One possible explanation for why the fit of our measurements to our model substantially over-predicts the diffusivity is that we have neglected photobleaching entirely. At the relatively low flowrates we are considering, we suspect that the sample has sufficient time to decrease in intensity as it flows downstream. Since the changes in fluorescent intensities we are comparing are very subtle to begin with, this could have a significant impact on our measurements. Indeed, the fact that we had to artificially impose conservation of mass on the collected data suggests that some reaction was taking place. Since higher concentrations of fluorescein will exhibit a greater intensity change after photobleaching than lower concentrations, when the data is renormalized the diffusivity will appear to be enhanced. Better understanding of the dynamics of this process would allow us to account for photobleaching explicitly in our model, by including a volumetric reaction term in the species conservation equation. Rather than pursuing this further, we attempt to measure the diffusivity in the absence of convection. In a static system where diffusion is purely transient, it is easier to correct for photobleaching, since the entire field of view has been subjected to light for the same amount of time. For these measurements, a gradient is established by convection before turning off the pumps and plugging the device's outlet. A video is then recorded as the gradient attenuates in time. This measurement proves more successful (Figure 5-2), predicting a diffusivity of 5.33×10^{-10} m^2/s, in good agreement with values from the literature.

Despite the challenges we encountered with this optical approach for gradient characterization, we were successful in a few important respects. First, we demonstrated the ability to create and preserve a concentration gradient over the full length of the device at the flowrates we plan to operate at (~1 $\mu L min^{-1}$). Second, by approaching the diffusion problem from both a transient and steady-state perspectives, we have obtained evidence in support of the hypothesis that the disagreement between our models and observations is attributable to the non-idealities of our experimental set-up (photobleaching), rather than any over sight in our model

that would be pertinent to non-fluorescent gradients. We consider this a satisfactory verification of the gradients created in our system, and proceed to consider the behavior of particles in these gradients.

5.2 Polystyrene Beads

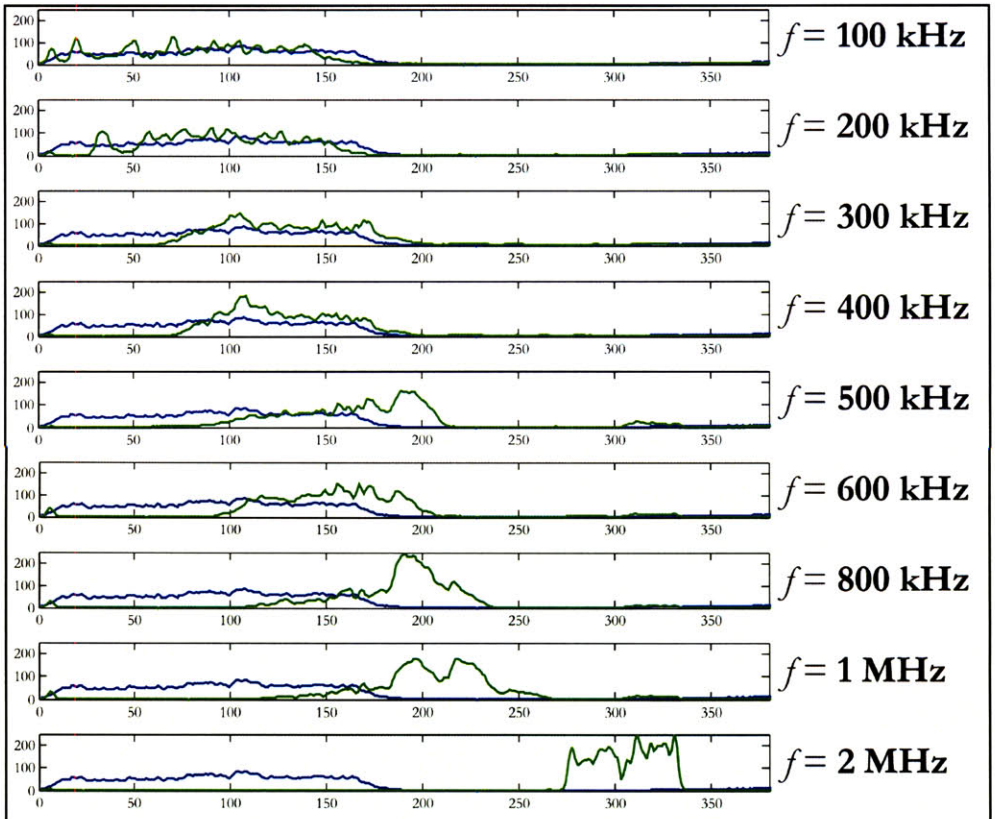

Figure 5-3: Microsphere concentrations along the channel width

Steady-state positions of microspheres with σ_h = 0.0089 Sm^{-1} and σ_l = 0.0009 Sm^{-1}. The green curves show the bead distributions produced at the specified frequencies with a voltage of $20V_{pp}$ and a flowrate of 2 $\mu Lmin^{-1}$. Blue curves depict the distribution of beads with the electrodes off.

Having established that a reasonably reliable conductivity gradient is established in the device, we proceed to add particles to the solution. We initially consider only a single particle type, since it allows us to characterize the device without complicating the experimental protocol unnecessarily. Because of their stable electrical properties and reasonable size, we choose the 1.6 μm diameter Fluoresbrite® BB microspheres (17686, Polysciences, Warrington, PA) as the primary beads for testing. The first objective is to choose appropriate operating conditions. For this, we use the measured DEP spectra of the beads, as shown in Figure 4-6. To avoid the electrokinetic flows that may emerge at higher media conductivities (>10^{-2} Sm^{-1}) and lower frequencies (<50 kHz), we choose to use a gradient ranging from a high conductivity of 10^{-3} Sm^{-1} to a low conductivity of 10^{-4} Sm^{-1}. This range, which is easily achievable using de-ionized water and small concentrations of PBS, corresponds to crossover frequencies of ~100 kHz.

The protocol for preparing a packaged device for an experiment varies slightly depending on the particles we are working with. For beads, no prior surface treatment is used on the PDMS. As a consequence, some degree of non-specific adhesion is usually observed. However, this does not seem to have any significant impact on the performance of the device during short-term experiments (~2-6 hours of continual flow of particles through the device) presented here. Often, the device is flushed with ethanol before use. This whets the chamber, and the low

surface tension and viscosity of ethanol relative to water helps to eliminate bubbles. This ethanol flush continues until all bubbles have been expelled either through the gas-permeable PDMS, or through the device's outlets. This typically takes 30 minutes to an hour.

In parallel with flushing the device, we prepare the bounding conductivities of the gradient, σ_h and σ_l, and add the test particles (~10^8 beads/mL) to the appropriate solution. Since we are initially interested in n-DEP operation, this corresponds to the high conductivity, σ_h. The beads are washed in the solution three times, to remove any trace of the media in which the beads were previously suspended. The two solutions, σ_h plus beads and σ_l, are then placed in separate 1mL syringes (Becton Dickinson, Franklin Lakes, NJ) and connected to the test setup, to which we also connect the fully packaged device. The two syringes are then placed in a single syringe pump (KD Scientific 200, Holliston, MA), and flow is started by setting the pump to a rate of 2 $\mu Lmin^{-1}$, corresponding to an actual flowrate of 4 $\mu Lmin^{-1}$, since the two input syringes are driven simultaneously. In cases where the device has been flushed with ethanol before hand, the system is given time to equilibrate. This assures that any ethanol which has diffused into the PDMS is given sufficient time to diffuse out. After the test solutions have flowed through the device for ~1 hr, and any new bubbles that were introduced during the switching of fluids have been expelled, the flowrate is decreased to typical operating levels of 1-3 $\mu Lmin^{-1}$ (combined flow through both inlets). Typically, it requires several minutes for the flow to equilibrate after changing the pump setting. After this time has lapsed, we are ready to begin collecting data.

We begin by connecting a function generator (33220A, Agilent, Palo Alto, CA) to the pins of the PCB. Since the function generator has a source impedance of 50 Ω, a voltage divider is formed between the source the imprecisely known device impedance. To measure the voltage actually delivered to the device, we connect an oscilloscope (Tektronix, Richardson, TX) to monitor the amplitude of the sinusoidal signal. Unless it is specified otherwise, the voltage used in all experiments has a peak-to-peak amplitude of 20 V (20 V_{pp}), corresponding to an RMS value of 7.07 V. We select an appropriate frequency and activate the electrodes. Since particles typically have a residence time in the separation chamber of 15-30 s, depending on flowrate and the chamber dimensions, the system is given 1-2 minutes to reach steady state after the electrodes are turned on. As might be expected, transients in the device (i.e. time after turning the electrodes on before all particles reach their IDPs, or time after turning the electrodes off before particles relax back to their original positions) are limited by the convective timescale (LU^{-1}). Once equilibrium is reached, we record video of the particles flowing through the channel for between 30 s to 1 min, depending on particle concentration and exposure time. These times have again been chosen empirically to keep file sizes manageable for data analysis while still capturing the behavior of a large number of particles. We repeat this process for a range of operating conditions, spanning different voltages, frequencies, and flowrates. These three parameters are particularly convenient, since they can be easily changed on the fly, and can be related back to characteristics of the device. Voltage and flowrate offer a metric for determining the magnitude of the CM factor at the IDP, while varying the frequency enables direct comparison to the measurements of crossover frequency.

Experiments have been performed with both single-barrier and ratchet IDS devices. Since the media conductivity used in these separations is very low, we expect the ratchet devices to offer better, more reliable performance (section 3.1). Once the data has been collected, we analyze it as outlined in section 4.4, by filtering the video in the time domain, followed by averaging over the height of the particle column. We consider the device's operation from three perspectives: frequency dependence, voltage dependence, and flow dependence.

Figure 5-3 shows typical cross-sections measured for the steady-state position of the beads at constant voltage, flowrate, and conductivity gradient as frequency is varied. In all experiments where n-DEP operation is used, the conductivity decreases from left to right across the channel's width, as viewed in these plots. The observed behavior in all experiments with these beads is qualitatively the same. With the electrodes off, particles are influenced only by the drag of the fluid. As a result, the equilibrium distribution is roughly uniform over half of the channel. Exciting the electrodes at an appropriate frequency causes the particles' trajectories to deflect. For these particles, the extent of this deflection into lower media conductivities increases with frequency. This is perhaps best explained from the perspective of the threshold CM factor, defined as the value of $\mathrm{Re}\{CM\}$ at the IDP. Since the IDP is determined by force balance between drag and DEP, and since the electrode and chamber geometries have been designed to deliver electric fields and fluid velocities that do not vary over the width of the chamber (except for very near to the walls), it follows that the value of $\mathrm{Re}\{CM\}$ at the IDP must not vary as a function of frequency or media conductivity. Changing one of these parameters, in this case frequency, forces a change in the other such that $\mathrm{Re}\{CM\}$, which depends upon them both, can remain constant.

We can go further with this line of reasoning by formally defining the IDP as the "center of mass" of the particle column downstream of the electrode barrier. Since we know the location the particles center around along the channel's width (from the data), and we know how the conductivity is expected to evolve throughout the channel (from the models), we can present the data in a form analogous to the plots of cross-over frequency versus media conductivity presented earlier (Figure 4-6). This is what we have done in Figure 5-4. The points extracted from the IDP data follow fairly closely the shape of the contour we propose for $\mathrm{Re}\{CM\} = 0$ (the cross-over frequencies). This contour is obtained by fitting the surface conductance model (equation 4-4) to the measured cross-over frequencies by varying the ζ-potential. The fit is optimal for $|\zeta| = 84\text{mV}$. To the extent that this model is accurate, a perfectly sensitive device would produce IDP data corresponding exactly to this contour.

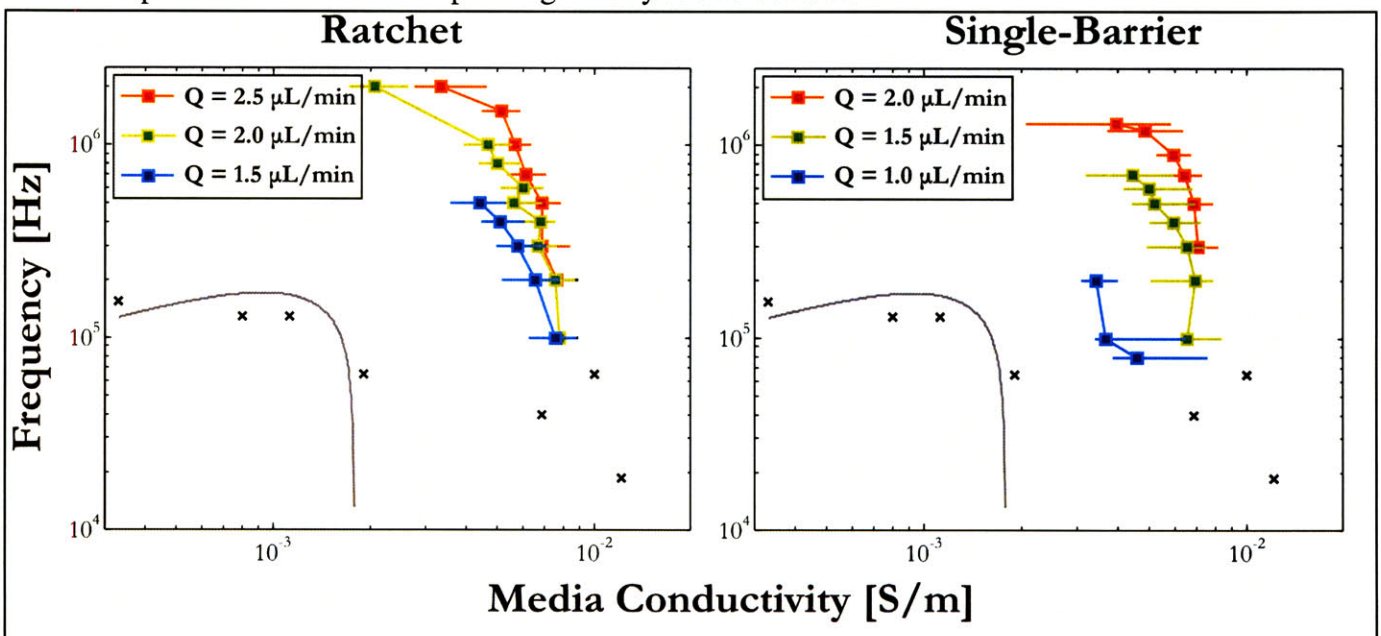

Figure 5-4: Frequencies and media conductivities at the IDPs

Comparison of IDPs measured for ratchet and single-barrier topologies under variable frequency and flowrate. '×' denotes cross-over frequencies measured under static conditions, with the gray curve showing the fit to the surface conductance model with $|\zeta| = 84\text{mV}$. The voltage in all cases is 20 V_{pp}.

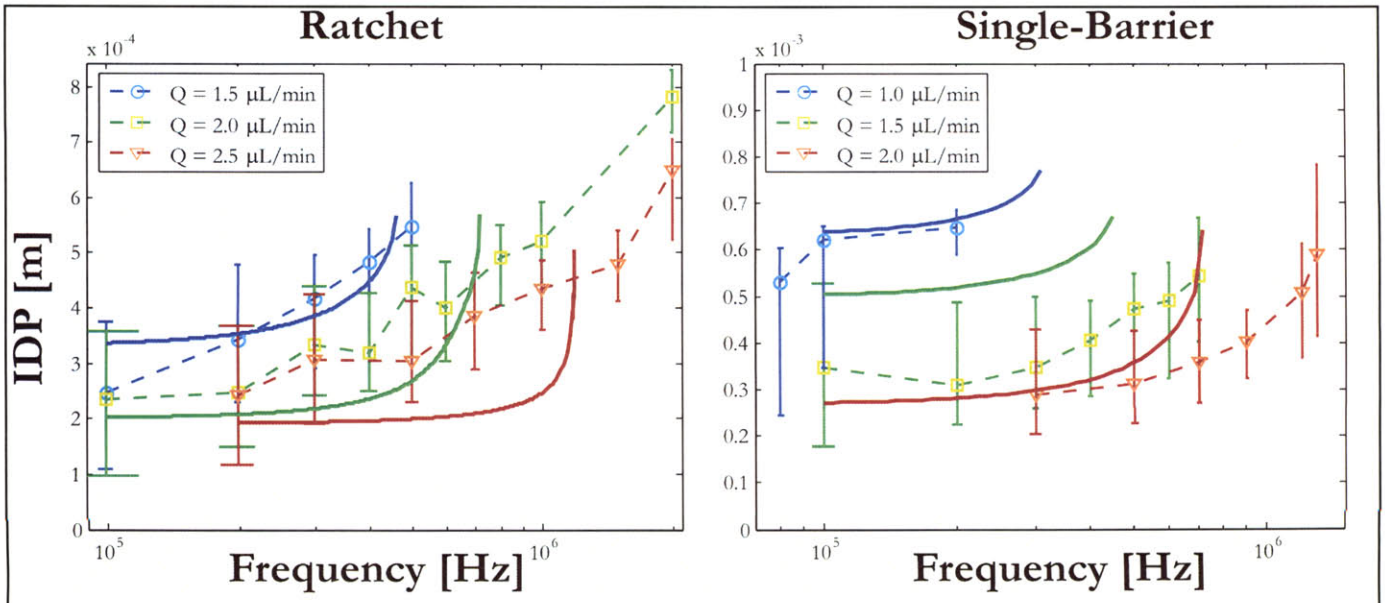

Figure 5-5: Comparison of predicted and measured IDPs.

The same data as in Figure 5-4, analyzed from a different perspective. Here, we compare the IDPs (solid curves) predicted from modeling to those determined experimentally. The model combines calculations of the drag and DEP forces, evolution of the conductivity gradient, and the surface conductance model for the beads' CM factor to determine their trajectories in the device.

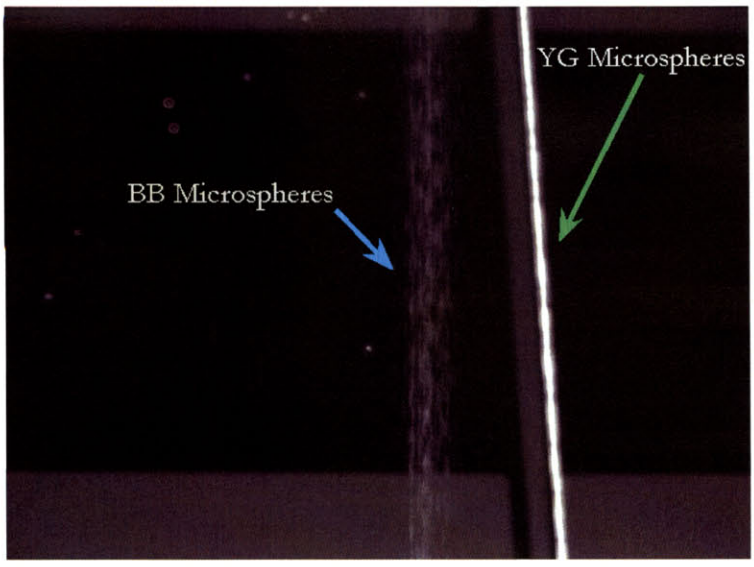

Figure 5-6: Separation using n-DEP

Separation of 1.6 μm microspheres (BB) from 1.9 μm microspheres (YG). The smaller beads have a higher conductivity, and thus separate earlier than the larger beads.

In getting to this point, we have said nothing regarding the forces acting on particles other than that the value of $\mathrm{Re}\{CM\}$ at the IDP ought to be independent of frequency and media *conductivity* for each particle. We now reverse our line of reasoning to see how well our dynamic models agree with the experiments. Starting with a prediction for the CM factor of these beads (obtained from the fit of cross-over frequencies to the ζ-potential model), we can calculate where we would expect the IDPs to be located. Figure 5-5 presents the same experimental data as that in Figure 5-4 from this perspective. Using the predicted CM factor, we calculate the point along the chamber width where particles pass over the DEP barrier;

this defines the predicted IDPs, which we superimpose on the directly observed results. We see from this that our models predict qualitatively how these particles will behave in the device, but are not terribly accurate quantitatively. This is likely caused by one or both of two factors; our incomplete model for the CM factor of the beads, and coupling between the particles caused by their overlapping disturbances to the electric fields and fluid velocities. We will discuss how these challenges may be overcome - or otherwise dealt with - in chapter 6.

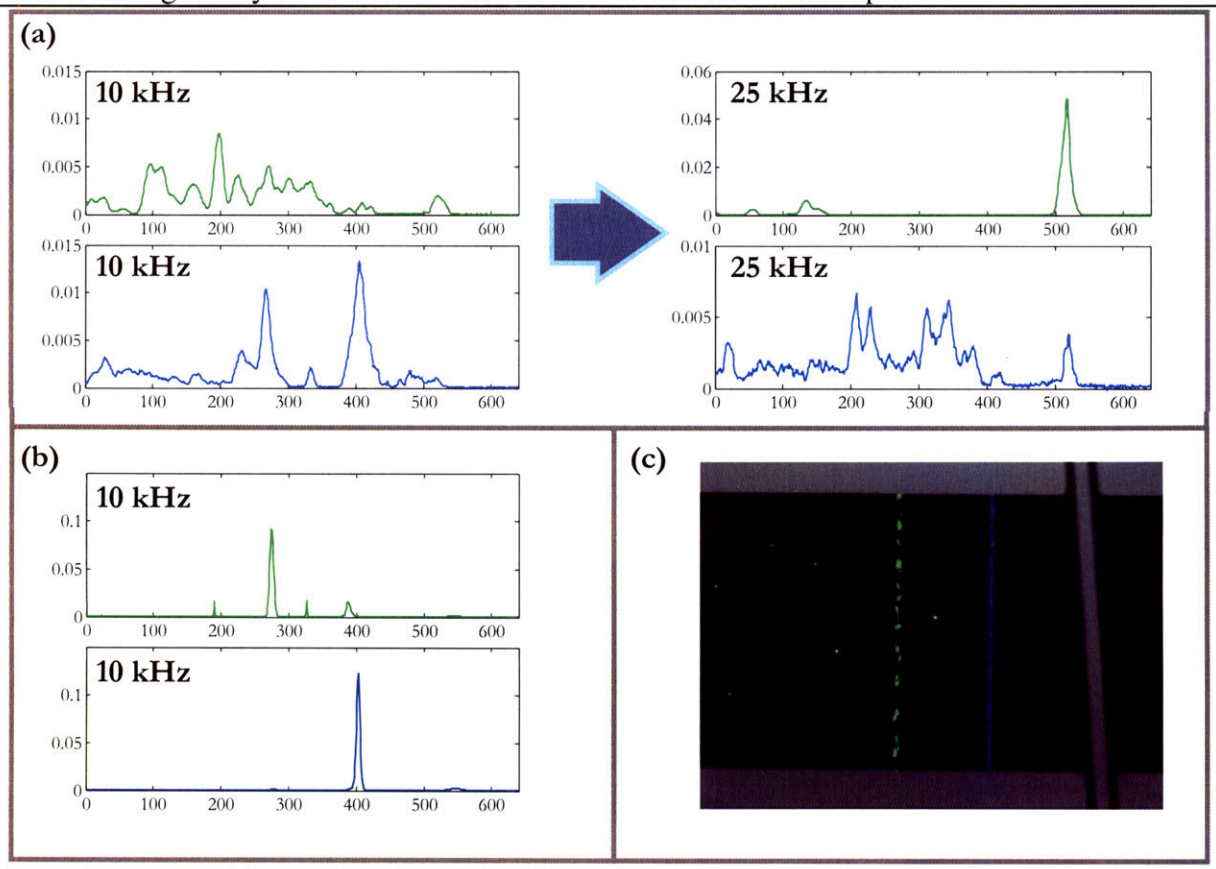

Figure 5-7: Separations using p-DEP

(a) At 10 kHz, the 1.6 μm beads (blue) are carried, on average, to higher conductivities than the 1.9 μm beads (green), though the purity is much worse than in Figure 5-6. (b) Increasing the frequency to 25 kHz causes the 1.9 μm beads (now undergoing n-DEP), to be carried across the entire width of the channel, while the 1.6 μm beads migrate less than in (a). (b) and (c) show the improvement in purity achieved by using lower concentrations of both beads, from the perspective of both the time-averaged image and the corresponding cross-section.

Having studied the behavior of one type of particle in the device, a natural extension is to add a second particle with a different DEP spectrum and try to separate them. This is complicated to some extent by the size-dependence of the particles' effective conductivities, as predicted by the R^{-1} dependence of the surface conductance model (equation 4-4). Larger polystyrene beads will generally have lower effective conductivities than beads with higher surface to volume ratios. Accordingly, we would expect that smaller particles would separate into higher conductivities than larger ones, and thus their IDPs would occur earlier in the channel. Indeed, this is what we observe (Figure 5-6). However, because of their difference in

size, the same behavior might be observed even if the two particles had identical conductivities, or perhaps even if the smaller one was *less* conductive. If a smaller particle is observed to pass over the DEP barrier earlier in the channel, it may be because it has a higher conductivity, but it may also just reflect the fact that the DEP force is volumetric, and thus weaker for smaller particles. Because of this underdetermined relationship between size, conductivity, and IDP, we decide that a more interesting separation of beads would use p-DEP, thus carrying the smaller particles further into the (increasing) conductivity gradient.

Operating the device using p-DEP is very similar to using n-DEP, except that the direction of the conductivity gradient is reversed, so that particles are initially suspended in low conductivities, and are carried by the electrodes into higher conductivities. For experiments involving 1.6- and 1.9-μm-diameter microspheres, we use a conductivity gradient ranging from 0.0004 to 0.003 Sm^{-1}, and frequencies around 10 kHz. Figure 5-7 shows some of the results. A point worth noting is that as we increase the frequency, we should eventually reach a point at which the larger beads experience n-DEP at all conductivities, while the smaller beads enter the separation chamber already suspended in roughly their iso-dielectric media. When this is the case, the smaller particles should pass over the electrode barrier unobstructed, while the larger beads should be directed across the entire width of the chamber. This behavior is observed when we switch from a frequency of 10 kHz to 25 kHz (Figure 5-7a). Smaller beads relax towards the right wall, while larger beads are carried across the width of the chamber.

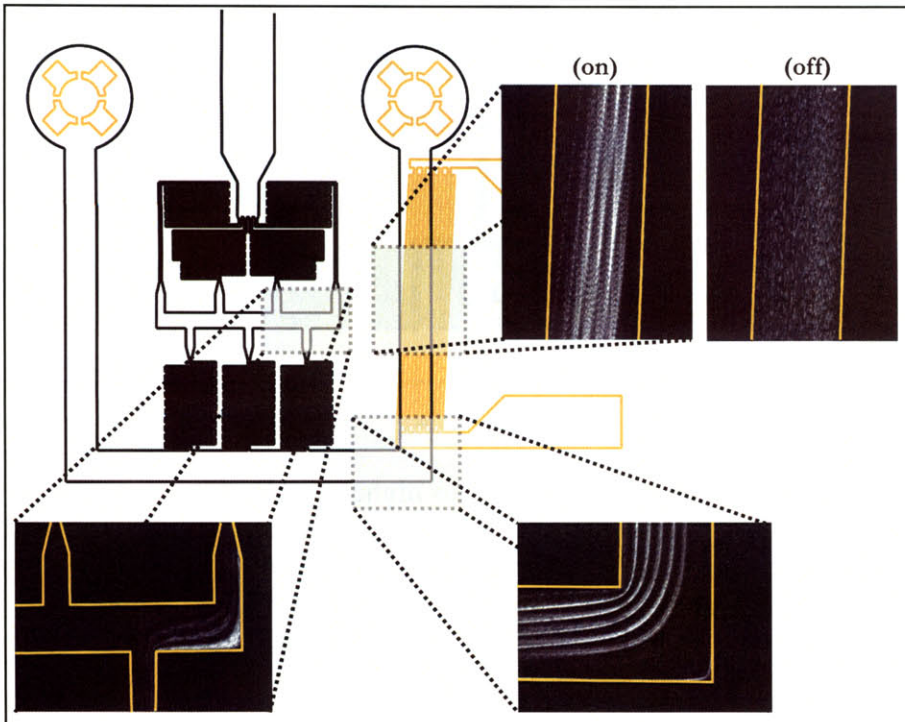

Figure 5-8: Prefocusing of polystyrene beads

Particles enter the separation chamber occupying a narrower range of conductivities than in the absence of this stage.

Using p-DEP to perform these separations introduces some new considerations. Because p-DEP brings the beads in contact with the electrodes, there are issues with sticking not present when n-DEP is used. As beads stick to the electrodes, they impede the path of subsequent beads, potentially causing them to pass through the barrier prematurely. As a result, the purity of the separation is degraded as compared to n-DEP separations, especially when higher concentrations are used (Figure 5-7a). Reducing the concentration improves the purity of the separation considerably (Figure 5-7b and c). Another consideration is that of additional electrokinetic phenomena associated with low frequencies;

such as AC electroosmosis. This refers to flow induced by the tangential component of the electric field acting on the screening charge at the electrode-fluid interface. At 10 kHz, we are well within the frequency range for which this phenomenon might be observed. Therefore, it is possible that the observed behavior is a combination of DEP and AC electroosmotic drag acting on the particles. Further investigation of p-DEP operation in this low-frequency regime would warrant inclusion of AC electroosmosis into our electrokinetic flow models.

Before continuing on to the other particles we have tested in the device, brief mention of the prefocusing stage is warranted. The idea behind this feature, introduced in section 3.1, is to deflect particles to one side of the channel, so that they enter the separation chamber as near as possible to one extreme of the conductivity gradient. Characteristic operation of this stage is shown in Figure 5-8. With the electrodes off, particles follow the fluid streamlines, and are distributed throughout one half of the channel volume. Turning the electrodes on deflects particles to the right with respect to the direction of flow. Because the particles have negligible diffusivity and inertia, they do not cross fluid streamlines except when acted upon by an external force, such as DEP. The result is that, at the entrance to the separation chamber, particles are confined to ~20% of the total chamber width.

Although this feature is functional, it was not included on all die, and for this reason was not used in all experiments (see, for example, the cross-sections in Figure 5-3, where particles occupy nearly half of the channel width with the electrodes off). It is likely that future designs will feature prefocusing more prominently.

5.3 Vesicles

The difficulty associated with separations of polystyrene beads follows primarily from the correlation between size and conductivity: more so than surface chemistry, we have found that the size of the bead determines its DEP spectrum. Vesicles offer a promising alternative to beads, in that they are polydisperse particles with conductivities that we are able to control precisely. The creation of these vesicles is discussed in section 4.2. For the experiment reported here, we performed electroformation using a ~10 μM fluorescein solution mixed with PBS to a conductivity of 0.0075 Sm^{-1}. We selected a conductivity range from 0.0156 to ~ 0 Sm^{-1} (DI water), with the expectation that the vesicles would separate into the center of the chamber. Prior to flowing the vesicles through the device, they are passed through a 10 μm filter to remove those

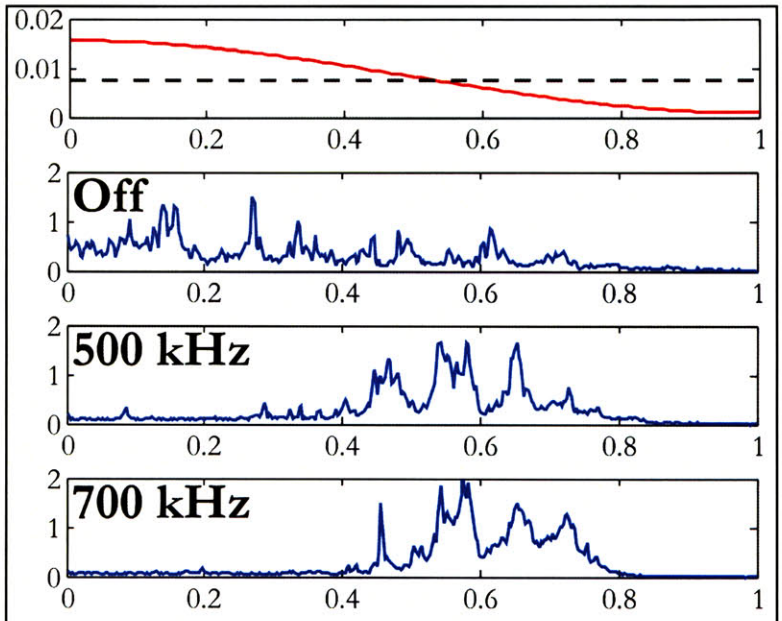

Figure 5-9: Observed behavior of vesicles in the device

The top plot shows the expected conductivity gradient, with a dashed line indicating the internal conductivity of the vesicles.

which are excessively large. Despite this precaution, some vesicles which exceed the chamber dimensions (in this case, a height of 18 μm) pass through the filter. To prevent the vesicles from sticking, the device is flushed with 0.1% BSA prior to use. This enables even the largest vesicles to flow through the chamber without sticking or rupturing. Results showing the observed position of the vesicles as well as the modeled conductivity gradient are shown in Figure 5-9. The roughness of the cross-sections is caused by the large vesicles that pass through the chamber very slowly and thus obstruct the path of other vesicles. This effect not withstanding, the majority of particles are seen to separate out close to the expected IDP. The observed bias towards lower conductivities may be attributable in part to the vesicle membrane decreasing the effective conductivity.

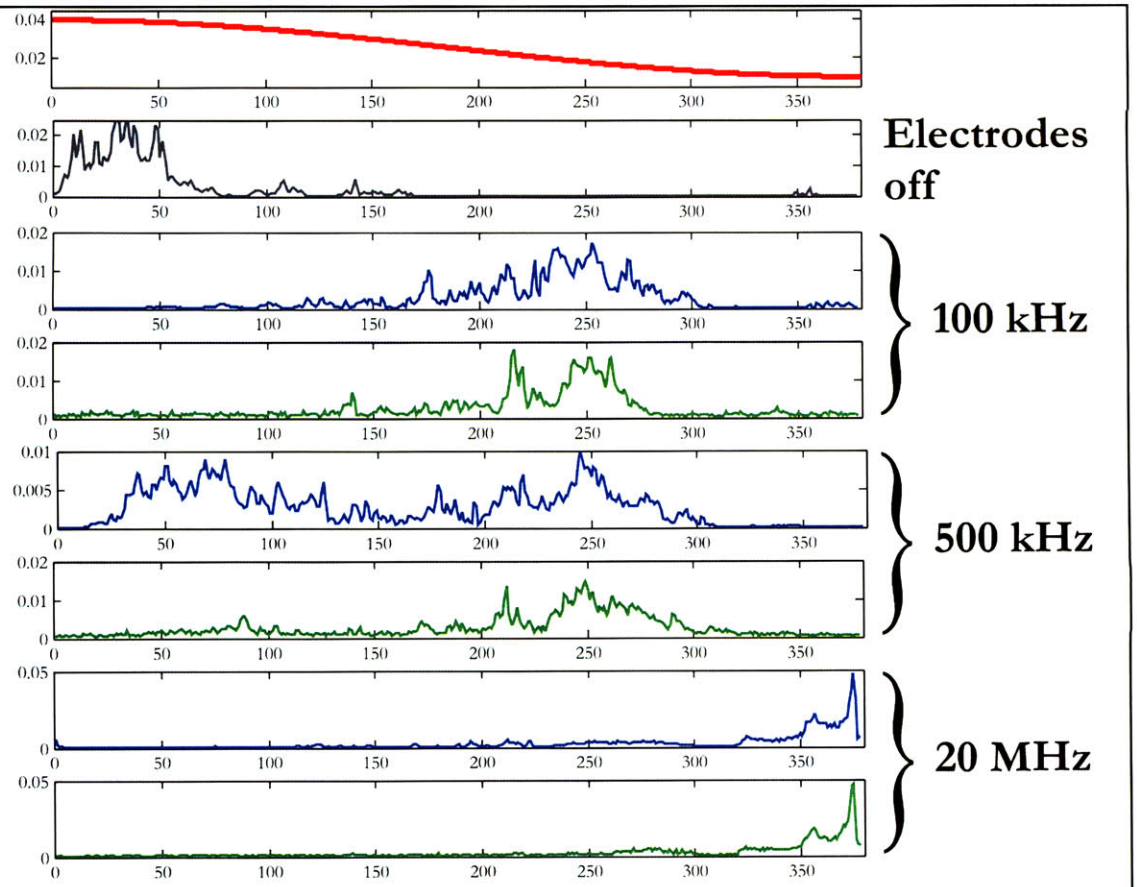

Figure 5-10: Separation of yeast based on viability

Blue curves represent (nominally) viable cells, while green curves show the spatial concentrations of non-viable cells.

5.4 Yeast

The first biological particle we use to test the device is yeast. Specifically, we attempt a viability assay, as outlined in section 4.3. The large size and high density of yeast relative to other particles we have considered leads us to increase the density of the media they are suspended in. Adding ~0.1g/mL of sucrose assures that cells are sufficiently buoyant to be

pumped into the device. We stain heat-treated cells with Syto 9 (Invitrogen, Carlsbad, CA) and viable cells with DAPI (Invitrogen, Carlsbad, CA). We use a conductivity gradient ranging from 0.04 S/m to 0.01 S/m, in keeping with measurements of cross-over frequencies (section 4.3). Figure 5-10 shows some of the results. At a frequency of 100 kHz, Re{*CM*} for both live and dead cells vanishes at a media conductivity of around 0.02 S/m. Accordingly, we observe their IDPs to be the same. As the frequency is increased to 500 kHz, the constant value of Re{*CM*} predicted for the heat-treated cells corresponds to a constant IDP. The viable cells, however, become subject to p-DEP at the lower end of the conductivity range we have chosen, and thus their IDPs shift to higher conductivities. If the frequency is increased further, the DEP force will become independent of conductivity, and both cell types (which have a lower permittivity than the media) should be deflected across the entire width of the chamber.

One feature of these results which warrants further discussion is the presence of two apparent peaks in the live cell population at 500 kHz. The correspondence of the second peak, at lower conductivity, with that observed for the dead cells at the same frequency suggests that the nominally live population contained a substantial number of non-viable cells. To estimate the percentage of the "live" population that may have been dead, we prepared yeast from the same dormant stock using the same protocol and suspending media. We then used Trypan Blue (Invitrogen, Carlsbad, CA) to stain cells in which the membrane had been compromised, and counted the stained and unstained cells. We observed that 55% ± 6% of the population were non-viable. This agrees well with estimates of the percentage of dead cells extracted from their IDPs at 500 kHz, from which we estimate that 60% ± 3% of the cells were non-viable. We expect that these challenges could most easily be overcome by culturing cells, rather than obtaining them from a dormant stock.

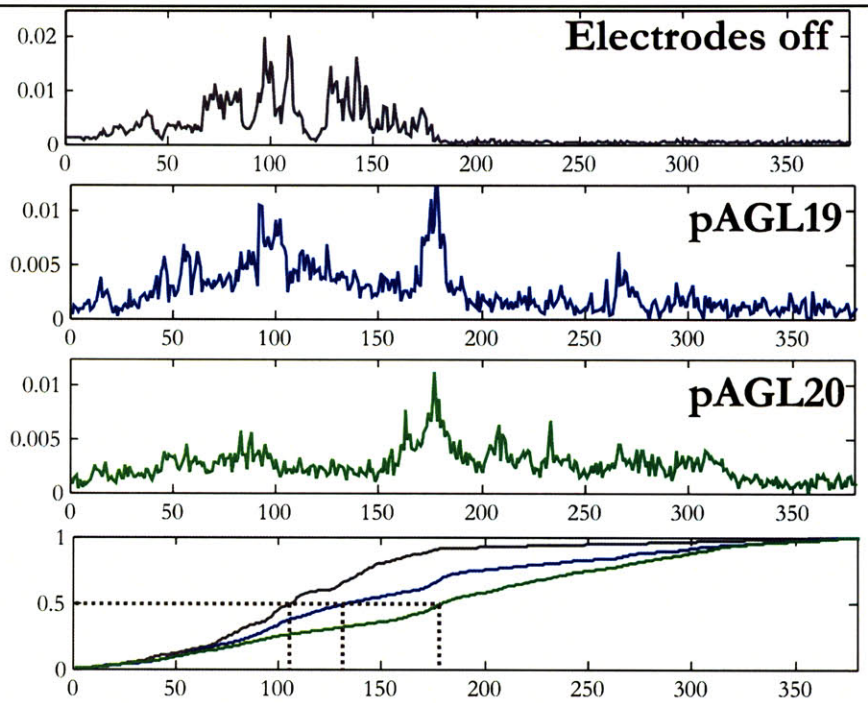

Figure 5-11: Representative observations for *E. coli* in the device

Observed behavior of +PHB (pAGL20) and –PHB (pAGL19) *E. coli* in a conductivity gradient ranging from 0.37 S/m to 0.05 S/m. Bottom plot integrates over the three cross-sections, with the average particle positions indicated. The voltage and frequency are 20 V_{pp} and 1 MHz.

5.5 E. Coli

In this section, we discuss our attempts to separate PHB-producing *E. coli* from wild-type. In all experiments, +PHB cells (pAGL20) are stained using Nile Red, while the control strain (pAGL19) is stained using DAPI. Figure 5-11 shows a typical result. With no applied voltage, cells are

restricted to the fraction of the channel at which they enter the separation chamber. When a 1 MHz signal with an amplitude of 10V is applied, both strains assume a very broad distribution over the width of the chamber, with a modestly higher concentration of the +PHB cells appearing at lower conductivities, as would be predicted by theory. The observed differences in behavior of +/-PHB *E. coli* in this and other similar experiments are very small, and we do not yet know if it is a consequence of inherent differences in the cells or some as yet not understood feature of the device.

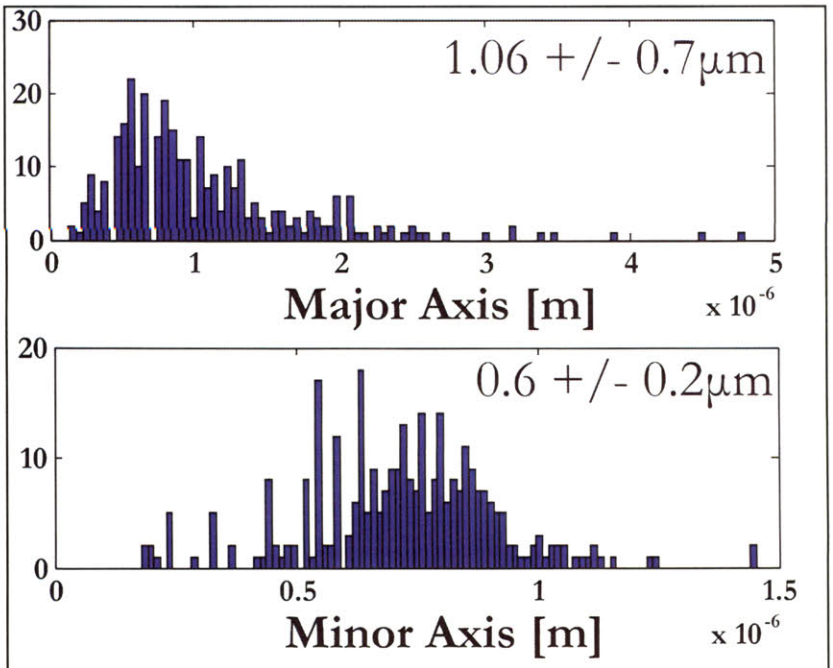

Figure 5-12: Size distributions of *E. coli*

Measurements were extracted by imaging cells aligned parallel and perpendicular to an applied electric field.

The broadness of the IDPs of *E. coli* as compared to those observed for beads, vesicles, and yeast, warrants some discussion. While we do not at this point know to what extent this is attributable to actual variations in electrical properties as opposed to variations in size, we suspect that it is largely an effect of the latter. To quantify size variations among the cells, we place them in a conductive suspension over interdigitated electrodes with a periodicity of 100 μm. Application of an electric field will repel the cells from the electrode edges (by n-DEP), leaving them only in regions where the field intensity gradient is low (i.e. in the centers of the electrodes and electrode gaps). Since the field in the electrode gap is oriented roughly perpendicular to that over the electrodes, and since torque on the induced dipoles in the cells tend to align them to the electric field, we are able to control the orientation of the cells. We use this to estimate the sizes and size distributions of the cells we are using for these experiments. Figure 5-12 shows the results, which are in good agreement with values reported elsewhere [29]. The variances we calculate in the lengths of the major and minor axes of the cells correspond to a variance for the volume of over 90%. This, combined with the small size of the average cells, suggests that any separation of *E. coli* by IDS will exhibit some size dependence.

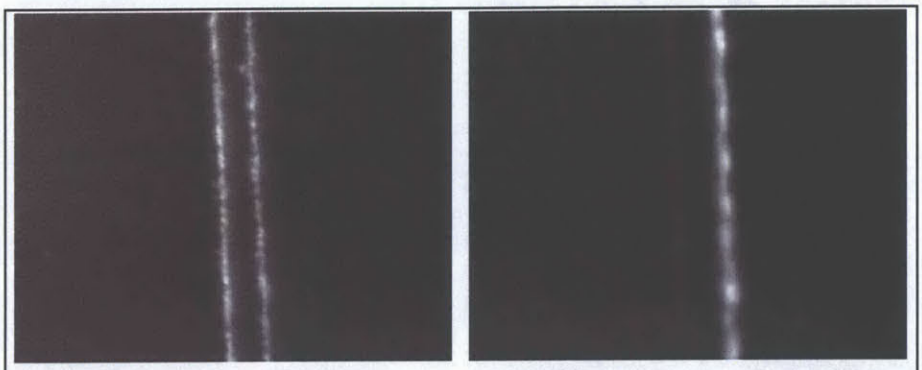

Figure 5-13: Behavior of *E. coli* at higher frequencies

Different responses of + and – PHB *E. coli* at 70 MHz and conductivities between 0.04 and 0.26 S/m. While -PHB cells undergo p-DEP at all conductivities, +PHB cells undergo n-DEP exclusively.

An additional interesting feature of these experiments is illustrated by the expected plots of the CM factor for *E. coli* given in Figure 4-10. At around 20 MHz, we expect the CM factor for *E. coli* to peak; therefore, if we wish to manipulate these cells via n-DEP at ~20 MHz, higher conductivities will be needed to assure that their DEP spectra will remain negative. Of course, higher conductivities are more problematic from the perspective of induced flows, so operating at these frequencies may be undesirable. An alternative approach is to keep the conductivity range lower but reduce the frequency to ~1 MHz. Now, however, the electric fields are not fully probing the cytoplasm, and +/-PHB cells are much less distinguishable. This produces the results we have already discussed, typified by Figure 5-11. Of course, we also have the option of increasing the operating frequency beyond 20 MHz, where the CM factor becomes negative again at lower conductivities. We have conducted experiments in this range, using relatively low conductivities (0.04 – 0.26 S/m) and high frequencies (50-80 MHz). In these cases, we observe very different DEP responses from the two strains (Figure 5-13); pAGL19 undergoes p-DEP at all conductivities, while pAGL20 undergoes exclusively n-DEP. This is likely attributable to the fact that we are at sufficiently high frequencies that the cells' electrical properties are now dictated predominantly by permittivity, and there may as well be no conductivity gradient at all. In order to perform optimal separations of +/- PHB *E. coli*, we suspect that it is necessary to increase the conductivity and operate at a frequency of around 10-20 MHz. In so doing, we would expect both cell types to undergo n-DEP, have sufficiently different electrical properties, and be sensitive to variations in the conductivity of their surroundings. We are currently pursuing one means of extending the range of conductivities we can operate at, discussed in section 2.5: decreasing the chamber height.

5.6 Scaling of thermally induced EHD flows

We believe that the relative effectiveness of our device in manipulating beads, vesicles, and yeast cells as compared to *E. coli* is explained by electrohydrodynamics and the arguments of section 2.5. In this final section of results, we discuss our efforts to experimentally verify some of our predictions for these flows.

We begin by considering the disturbances to the conductivity gradient produced by EHD flows. A natural way to investigate these effects is to superimpose a gradient in some fluorescent salt on a gradient in conductivity. Monitoring the shape of the fluorescence gradient offers direct insight into the shape of the conductivity gradient. Figure 5-14 shows the results of such an experiment, where we see that the gradient changes only very slightly upon the application of a 10V-amplitude signal, as would be used in most separations. In reality, convective mixing is likely even less significant than these results suggest; the fluorescein used to monitor the gradient has a temperature coefficient of intensity of around -0.36% per °C [44]. While this is much lower than other tracer dyes (roughly 8× lower than that of rhodamine), it is sufficient to produce an overall decrease in fluorescence intensity, an effect not taken into account in the accompanying figure, where we have subtracted out from each curve the mean value for the intensity. Based on these observations, even if the disturbance to the gradient is wholly attributable to convection, we may

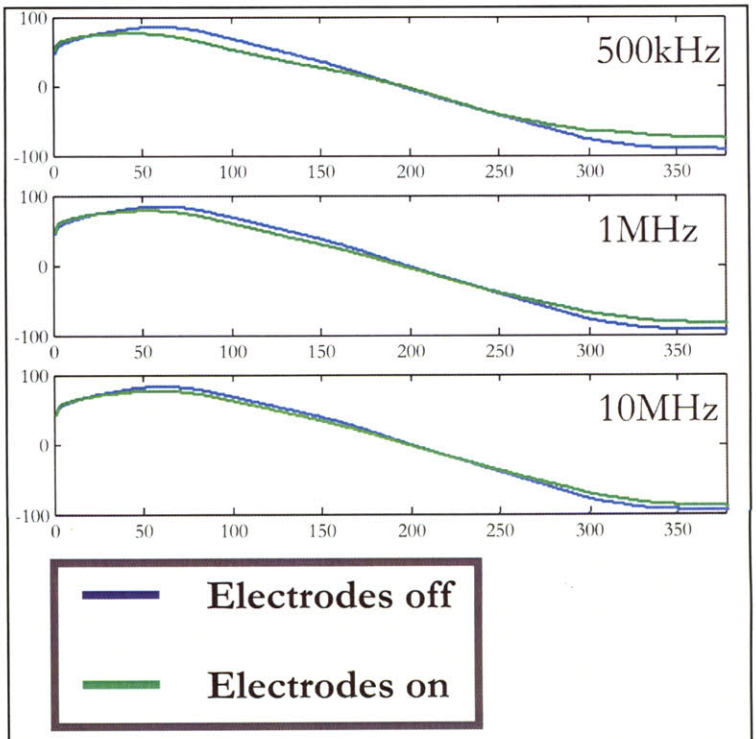

Figure 5-14: Observed changes in fluorescent intensity gradients under applied electric fields ($20V_{pp}$).

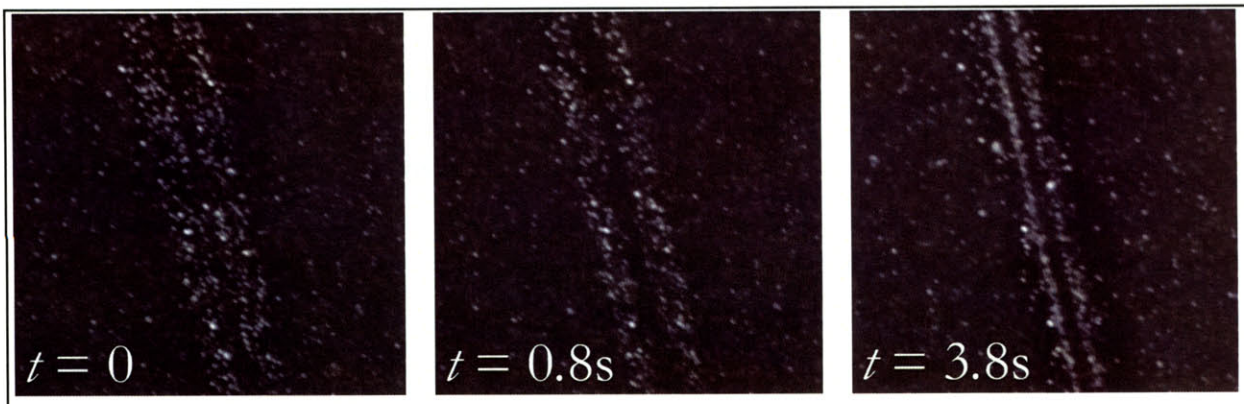

Figure 5-15: Flow visualization using polystyrene beads

Time series of beads subjected to thermal EHD flows. The brighter appearance of the beads on top of the electrodes is a consequence of the greater reflectiveness of gold relative to Pyrex.

conclude that this effect is not significant.

We turn now to the effects of EHD flows on *particles*, effects which we expect to matter greatly under some operating conditions (section 2.5). To visualize these flows, we use small (1 μm) tracer beads. Since these beads are acted upon by both DEP and EHD drag, they offer insight as to the conditions under which either of these forces dominate. By using smaller beads, we assure that drag ($\sim R$) will overwhelm DEP ($\sim R^3$) for a wider range of operating conditions than would be the case for larger particles. Figure 5-15 shows a case where induced drag completely overwhelms DEP. Before the electrodes are turned on (t = 0), the beads are distributed uniformly. Immediately after applying a 10V, 10MHz signal, beads evacuate the spacing between the electrodes (t = 0.8s) as they are entrained in the EHD vortices. The beads recirculate until they reach the center of these vortices, after about 3.8s. Note that the third image is *not* showing particles undergoing p-DEP; the media conductivity is sufficiently high (0.33 S/m) that Re{CM} for these polystyrene beads is exclusively negative. Rather, they are held near the electrodes *in spite* of the DEP force pushing them away.

It is possible to extend our analysis of electro-thermal flows somewhat further, and attempt to verify the scaling laws discussed in section 2.5. In modeling EHD flows, the large width of the chamber relative to the electrode spacing and channel height allowed us to neglect the fact that the electrodes are actually at an angle with respect to the chamber walls; since they are nearly always very far from the region in which the flows are strongest, these walls have little effect on the characteristics of the flow vortices our models predicted. The asymmetry of the electrodes with respect to these walls does, however, have an important effect in cases where no volumetric flowrate is imposed on the system (e.g. the inlet and outlet are left open) – the electrodes act as a pump [45]. Without working out the details of this induced net flow, we may use it to check the dependencies of EHD predicted by our modeling. Far away from the electrodes, induced drag is the *only* significant force acting on beads; by measuring the velocities at which these beads move, we can decouple the effects of drag from those of DEP.

We consider the effects of media conductivity, applied voltage, and chamber height on thermally induced EHD. We mold PDMS chambers with heights of 18, 12, and 8 μm to be used with each of three conductivities (0.11, 0.33, and 0.93 S/m). Separate chambers are used for each conductivity to avoid cross-contamination between the different experimental conditions. We open the inlets and outlets of these chambers to the atmosphere, and place the chamber (without bonding it) on one of the IDS chips. A suspension of tracer beads at one of the specified conductivities is carefully injected into the chamber. We then actuate the electrodes at different voltages, holding the frequency at 10 MHz, and record the motion of the beads.

To extract a characteristic velocity from this data, we use a crude method that nonetheless produces reliable results for a large majority (~80%) of the data files. Specifically, we apply a correlation filter to the same region of pixels in an earlier and later frame. This process produces (in most cases) a well-defined peak corresponding to the velocity with which most of the particles were moving. The position of this peak, divided by the number of frames between the two images used, gives a value which we interpret as proportional to the thermally induced EHD velocity. We use this to compare the significance of EHD under different operating conditions.

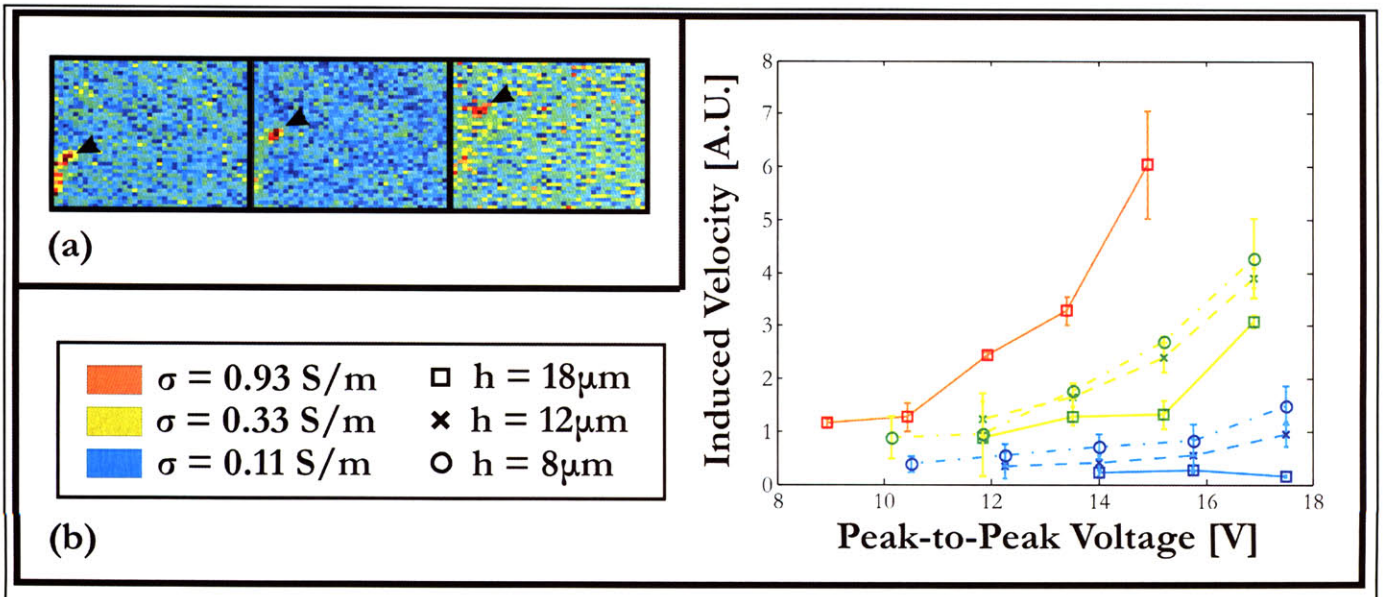

Figure 5-16: Measuring scales for EHD velocities

Inferred EHD velocities based on induced net flow from transverse electrokinetic effects using particle velocimetry. (a) depicts typical results of the correlation filter used to track average bead motion, applied to three successive frames. (b) shows dependence of EHD velocities on applied voltage, media conductivity, and chamber height.

Regressions of the four curves in Figure 5-16 obtained for the two highest conductivities suggest that the induced velocities depend on voltage to the powers of 4.04, 3.86, 3.81, and 3.26, as compared to a predicted scaling of V^4. We also observe an approximately linear scaling with conductivity. Interestingly, these observations even support the (somewhat counterintuitive) weak *inverse* dependence on channel height predicted in Figure 2-11. Of course, further refinement of the experimental set-up and data processing routines would be necessary to say anything conclusive regarding the observed scaling of EHD. These results nonetheless support that we are correct in predicting at least the underlying mechanism for these flows.

Chapter 6: Conclusions and Future Work

This thesis has described a new method for the separation of microorganisms, which we have called IDS, with emphasis on one particular implementation of this method. We have modeled, fabricated, and tested the device, and shown its performance to be largely commensurate with our predictions. In this final chapter, we will discuss improvements that could be made to all three of these major phases of the project to improve both our understanding of the device as well as its performance. We conclude with a brief discussion of alternate approaches to IDS, and how they might be expected to compare to the architecture presented in this thesis.

6.1 Modeling

The models we have developed for our device cover a broad range of physical phenomena. Specifically, we have considered heat, mass, and momentum transfer, in addition to electric fields and the forces they produce on particles and fluids. We have developed models that predict qualitatively and quantitatively, to reasonable accuracy, the failure modes of our device. Our efforts towards comparing the predictions of our models to direct experimental results, however, have been met with only limited success. One area in particular which I will focus on here are the effects of high local concentrations of particles on the performance our device (first mentioned in section 2.3).

The significance of this problem is thrown in relief when we consider the approximate magnitude of some of the terms we have ignored. The speed of a particle moving at a constant velocity along the axis of the electrodes is given by $U\cos(\theta)$, where U here denotes the velocity the particle would have if the electrodes were turned off, and θ denotes the angle of the electrodes with respect to the axis of the channel. This analysis is complicated by the fact that the imposed flow is not constant; it is not trivial to relate the unperturbed *particle* velocity (i.e. the particle's velocity in the absence of any DEP force) to an unperturbed *fluid* velocity (i.e. the fluid velocity in the absence of any particle), since the fluid velocity is a function of position along the channel's height. Nonetheless, we proceed by approximating the components of the disturbance velocity associated with any single particle as $U\cos(\theta)\sin(\theta)$ in x, and $U[1 - \cos^2(\theta)]$ in z. Since θ is 4° in a 1mm wide device, these disturbances are typically very small. Nonetheless, we believe that they can have significant consequences, especially when particles begin to move relative to one another, as happens when they approach their IDPs. We have observed phenomena that may be attributable to this coupling at low flowrates, where the stress induced on the surface of one particle by a second particle moving relative to it may be comparable to the stress induced by the fluid alone. Specifically, the motion of downstream particles seems in some cases to pull on upstream particles. As a consequence, we occasionally observe particles passing over the electrodes in a pattern analogous to a propagating wavefront (Figure 6-1). This type of coupling could have significant implications for the performance of our device when we are trying to separate particles. It seems possible that, at high enough concentrations and low enough flowrates, the particles could become coupled to the point that they migrate together, regardless of any differences in their electrical properties. We are thus motivated to try to better understand how particles in close proximity interact.

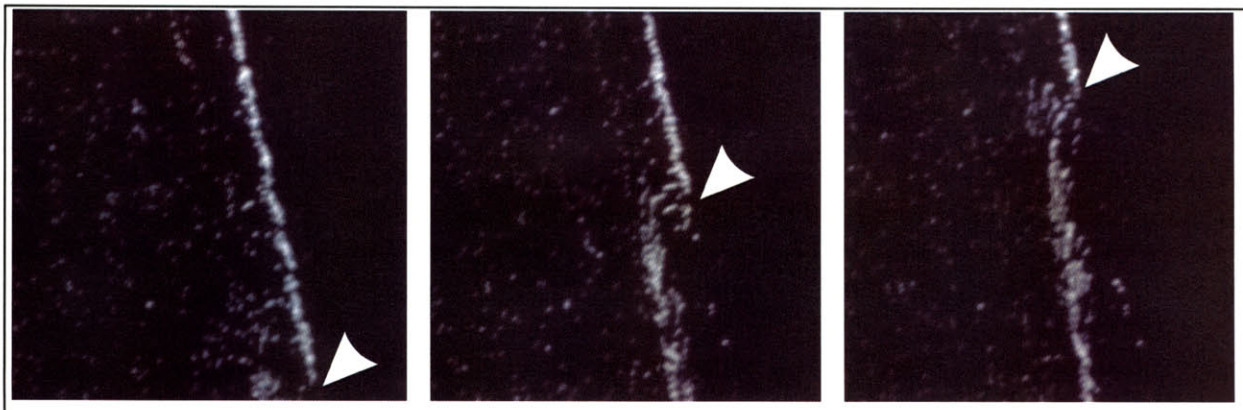

Figure 6-1: Possible hydrodynamic coupling between beads

Closely spaced beads passing over the electrodes under low imposed flowrate. We suspect that the beads are hydrodynamically coupled, so that beads in relative motion downstream "pull" on beads further upstream.

Beyond disturbances to the flow, we may also wish to consider the electrical coupling of particles. Figure 1-2 illustrates how a uniform applied electric field is disturbed by the presence of a spherical particle. The disturbance electric field, in this simplified case, decays as $(r/R)^{-3}$ as we move away from the particle's surface. We see, then, that particles need not be separated by a tremendous distance in order for their disturbance fields to decouple. Additionally, because the particles are moving parallel to the electrodes while their dipoles are aligned in a perpendicular direction, the electrical coupling should produce no force tending to push particles prematurely past the DEP barrier. Since the electrical coupling between particles in this configuration is repulsive, we do not expect it to cause particles to cluster together or move as a unit, as was predicted for hydrodynamical coupling. For these reasons, we view the fluid mechanics problem to have a more profound influence on the operation of our device.

6.2 Fabrication

Much of the rationale behind our choice of architecture and materials was ease of fabrication. In particular, we selected a planar electrode topology and a PDMS microfluidic chamber primarily for this reason, despite the fact that the device may have performed better or more reliably had we made alternate selections. In this section, I will outline some different fabrication schemes that may be worth pursuing in subsequent designs.

The use of PDMS in our device has been particularly problematic. At various times, we have had difficulty aligning the channel to the electrodes, observed staining of the chamber with fluorescent proteins used as surface treatments, and had concerns about small fissures in the SU-8 from which we pattern the chambers. An additional concern, though not one which we have encountered directly, is the diffusion of water and small solutes into the PDMS [46]. This could alter the characteristics of our conductivity gradient if a device is used more than once. Without changing anything in the design of our device, it would be possible to switch to an alternate fabrication scheme. Integrated electrical / microfluidic systems have been fabricated by bonding two patterned wafers together around an intermediate spacer (for instance, polyimide [47] or SU-8 [29]) defining the channel. Adopting a similar process would relieve us of the design constraints imposed by planar electrodes and deformation of the channel ceiling. Since bonded wafers would likely be able to withstand higher pressures and would be inert to a wider range of

chemicals and solvents than PDMS, this fabrication scheme might facilitate cleaning of the device without disassembling it. Of course, all of this is not to say that the use of PDMS in our device is without merit – it has greatly facilitated the removal of bubbles from the chamber, and gives us more flexibility in experimenting with different chamber heights. Rather than replacing the PDMS devices altogether, it may be advantageous to pursue alternate fabrication schemes in parallel. We could then use the device best suited to a particular application.

6.3 Testing

In our discussion of particle-particle interactions in section 6.1, we proposed extending our models to resolve the discrepancies we have seen between prediction of device performance and experimental observations. An alternate approach to resolving these discrepancies would be to design the experimental setup to better correspond with our models. This could be as simple as reducing the concentration of particles we flow through the device. Eliminating particle coupling in this way would determine if we are correct in our hypothesis that it is the primary source of disagreement between theory and experiment.

Most of the experiments in which we have sought to quantify the device's performance have used polystyrene beads as test particles. These are notoriously difficult to characterize electrically, and so it is possible that much of the disagreement between predictions and experiments is attributable to our incomplete knowledge of the particles, rather than incomplete knowledge of the device. This could be resolved experimentally as well, by focusing our attention on vesicles, which have much more well defined electrical properties. A series of experiments in which vesicles of different, known conductivities are prepared and passed through the device would help us to converge on a measure of sensitivity – how overlap between the distribution of IDPs (sample purity) varies with differences in particle conductivity, for instance.

Besides developing new experiments for device characterization, we also plan to further investigate applications. We are currently exploring measures to improve the sensitivity of our device for working with *E. coli*, by reducing the chamber height, for instance. By extending our protocols to the actual collection of sorted particles, we can also test to see if *E. coli* exhibiting IDPs at lower media conductivities exhibit higher production of PHB. The expertise of our collaborators in the Stephanopolous lab will be of great help to us with these assays.

6.4 Alternate Approaches

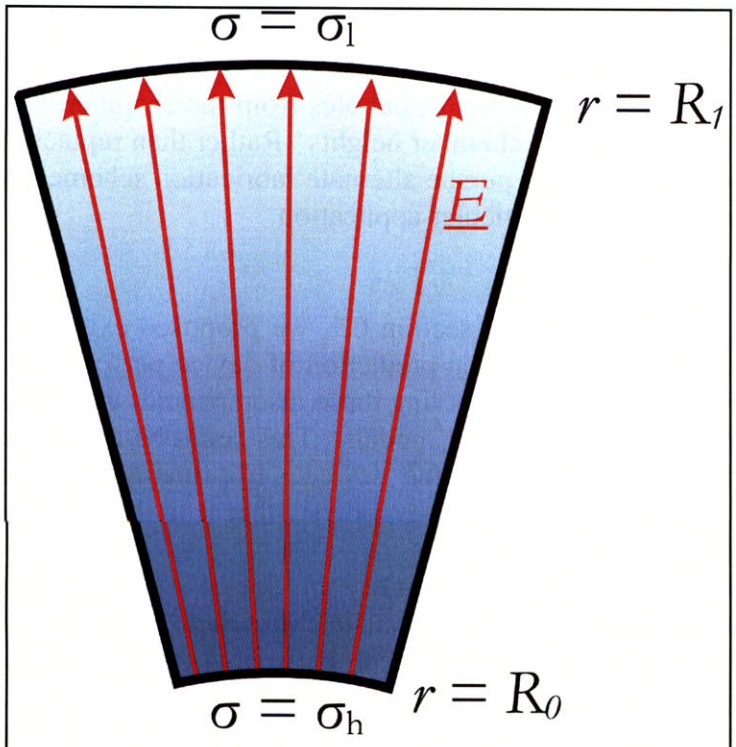

Figure 6-2: Batch IDS

Top view of a possible geometry for batch IDS. Conductivities at R_0 and R_1 are held fixed by large fluid reservoirs (not shown).

This thesis has focused on a particular implementation of an iso-dielectric separator, presented largely in the context of a particular application – separation of +/- PHB *E. coli*. It is worth mentioning what other implementations we might find worth pursuing. The suggestions made here are highly speculative, and have not been supplemented by any rigorous analysis. Accordingly, they are intended as general thoughts on how IDS may be implemented, rather than suggestions for specific architectures.

In section 1.5, we described our rationale for choosing a continuous implementation of IDS rather than a batch method, while still acknowledging that the batch method has the attractive feature of being, at least in theory, insensitive to variations in cell sizes. Figure 6-2 outlines a possible implementation of a batch IDS device. The geometry is essentially a cylindrical annulus, swept out by some small angle. Here, we have a single microfluidic chamber with an inlet and outlet that opens into two large reservoirs (not shown). Placing two solutions and waiting for the system to equilibrate would produce a conductivity gradient along the length of the channel. The channel is also designed to taper as it approaches the high conductivity reservoir; this is designed to shape an electric field, so that it is collinear with conductivity (section 1.5). We could create such an electric field by simply placing two (macro-scale) electrodes into each reservoir. Injecting cells into either of the inlets would cause them to be propelled into the channel, where they would migrate via DEP to their iso-dielectric points. Ignoring such non-idealities as disturbance of the gradient as the cells are injected or migrate down the channel, how well might such an implementation work?

For this geometry, we can solve for the conductivity exactly to obtain:

$$\tilde{\sigma}(\tilde{r}) = \frac{\sigma(r)}{\sigma_h} = \frac{(\sigma_h - \sigma_l)}{\sigma_h \ln(R_0 / R_1)} \ln(\tilde{r}) + \frac{\sigma_l}{\sigma_h} \qquad \textbf{(6-1)}$$

The curvature of the system prevents the conductivity from varying linearly. One consequence of this is that if the chamber diverges too much ($R_1 >> R_0$), the region of varying conductivity will be limited to a small fraction of the chamber length. We can learn more by solving for the electric field exactly:

$$\tilde{E}_r(\tilde{r}) = \frac{E_r(r)}{\Delta V / R_1} = \frac{(\sigma_h - \sigma_l)}{\sigma_h \ln(R_0/R_1)\ln(\sigma_l/\sigma_h)}\left[\frac{1}{\tilde{r}\tilde{\sigma}(\tilde{r})}\right] \quad \textbf{(6-2)}$$

We can conclude a few things from this result. First, we see that some care is necessary to assure that field intensity is collinear with conductivity; we can show that the condition for collinearity is:

$$\tilde{\sigma} > \tilde{r}\left|\frac{\partial\tilde{\sigma}}{\partial\tilde{r}}\right| \text{ for all } \tilde{r} \quad \textbf{(6-3)}$$

or, equivalently, for a monotonically decreasing conductivity:

$$\ln\left[\frac{R_1}{R_0}\right] > \frac{\sigma_h - \sigma_l}{\sigma_l} \quad \textbf{(6-4)}$$

Not surprisingly, we now see that creating collinear field- and conductivity gradients depends on both geometry and conductivity; if the conductivity changes too much or the channel's geometry is not sufficiently divergent, we will be unable to perform IDS.

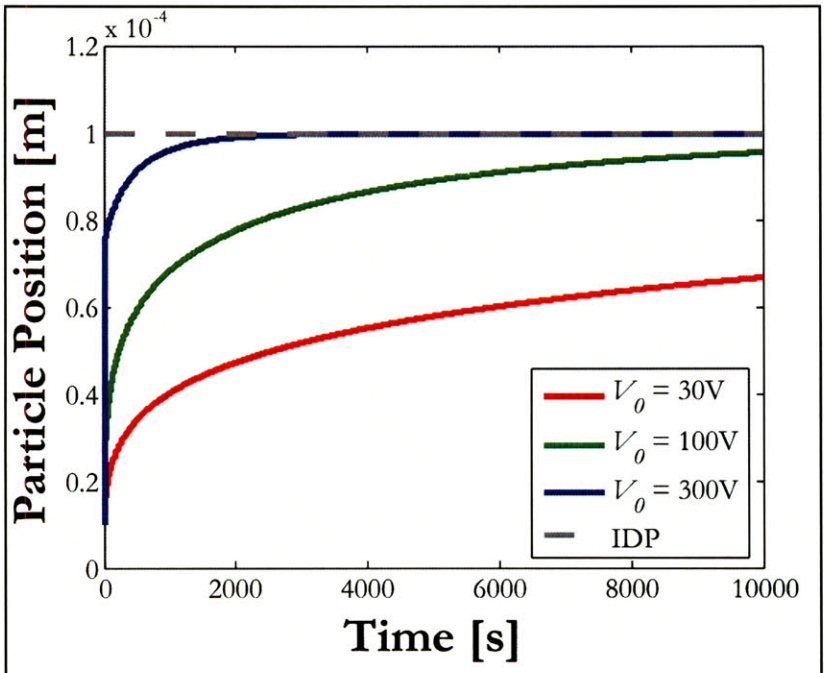

Figure 6-3: Dynamic response of cells in batch IDS

Convergence of particles (radius of 1 μm) on their IDPs over time, for the device shown schematically in Figure 6-2. We have taken R_0 = 10 μm, R_1 = 100 μm, σ_h = 1 S/m, and $\sigma_l = \sigma_p$ = 0.5 S/m.

These limitations aside, how long might it take to perform separations by this method, and what voltages might we need to do so? To address this, we once again balance drag with DEP to find the speed at which cells might be expected to migrate towards their IDPs. Using the dipole approximation for the DEP force, Stokes' Law for the drag force, and assuming the CM factor of the particles is determined by relative conductivities only (valid for low frequencies), we can solve exactly for the radial position of cells in the device as a function of time. If we take some reasonable values for system parameters, we can determine how fast particles will converge on their IDPs as a function of voltage, for instance (Figure 6-3). For a chamber with R_0 = 10 μm, R_1 = 100 μm, and a conductivity gradient that changes from 1 S/m to 0.5 S/m, we predict that the particles would migrate to their IDPs within about 30 minutes for a 300 V potential difference across the chamber. While not altogether unreasonable, this is not particularly encouraging. First, operating at such high

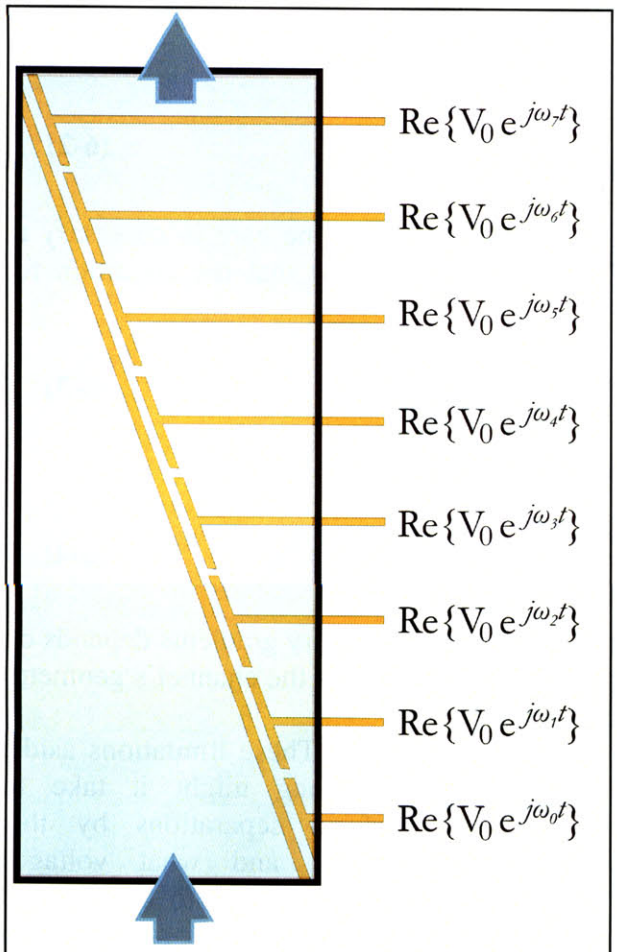

Figure 6-4: Frequency gradient IDS

Possible architecture for frequency-based IDS, chosen by analogy to the current conductivity-based implementation.

voltages would limit the range of frequencies we could use by purely instrumentation constraints. Second, it may be difficult to maintain a conductivity gradient over such a short chamber for this length of time, where diffusion is occurring 2-3 orders of magnitude faster than the cells are migrating. While the models presented here are by no means comprehensive or conclusive, they suggest that, while a batch approach would probably be feasible, any such implementation would have substantial enough limitations to preclude abandonment of the continuous approach described in this thesis.

The argument in favor of a batch method is the improved sensitivity that is gained when the separation must no longer compete with molecular diffusion. Of course, it is not the only way to achieve this effect. We have already observed the duality between frequency and conductivity described by the CM factor. By changing the frequency, our device forced particles to migrate to a new conductivity such that $\mathrm{Re}\{CM\}$ remained constant. We could, in theory, pose this problem from the opposite perspective, using a frequency gradient superimposed on constant conductivity to perform IDS. Although establishing a frequency gradient would require additional instrumentation commensurate with how finely we discretize the frequencies, we would no longer have to worry about attenuation of the conductivity gradient, and could thus operate at lower flowrates to improve sensitivity. An architecture similar to the cartoon in Figure 6-4 is one possible implementation, though almost certainly not the best one. As with a batch implementation, more work is needed to determine the strengths and weaknesses of this particular approach.

6.5 Scaling of IDS for Different Applications

One question we may wish to consider before concluding is how this particular implementation of IDS scales with particle size. As an example, we consider the implications of shifting our focus from prokaryotic cells (*E. coli*) to mammalian cells. We begin by considering the changes necessitated by the increase in the size of the cells. We found that we were able to successfully manipulate yeast (R ~ 2.5 μm) using a chamber that was (18 μm high)×(1mm wide)×(1.5cm long), and so we conclude that particles with diameters of as much as ~20% the channel height can be accommodated without clogging. The yeast radius will therefore serve as a reference for the following scaling analysis. For a cell with a radius a times larger than that of yeast, one approach is to scale the entire device by this same factor, so that the channel

dimensions and the electrode spacing are now larger by a factor of a. Since this larger device is still self-similar to the old ones, the relationships reported in sections 2.6 and 2.7 remain valid. Assuming the electrode spacing matches the channel height ($h/d = 1$) we found that the threshold value of the CM factor, K_0, was given by:

$$K_0 = \frac{\mu c D h^3}{0.3117 \varepsilon_m R V_0^2 w \tilde{z}_0} \qquad \textbf{(6-5a)}$$

The implications of this scaling depend on what we hold constant. If we wish to operate at the same voltage for the larger mammalian cells as we did with the yeast, then we see that K_0 *increases* by a factor of a, which suggests that IDS does not scale favorably for larger particles. Alternatively, if the electric field is held constant, a factor of h^2 is absorbed from the numerator and combined with V_0 in the denominator, and K_0 now *decreases* by a factor of a. While this may seem like a plausible argument, it excludes many important considerations. First, an electric field intensity that is not damaging to yeast or bacteria may be fatal to more physiologically sensitive mammalian cells. Second, at constant field intensity and larger channel heights, EHD flows become more significant (section 2.5), further undermining device performance.

Of course, all of these arguments are equally valid in reverse; decreasing particle and system sizes produce favorable scaling, *provided that the materials, fabrication processes, and operating protocols are able to keep pace.* This does not contradict our previous arguments that large particles are easier to work with than smaller ones, since for the work presented in this thesis, the channel height was held within a factor of ~2 (10-18 μm), while particle sizes varied by a factor of ~4 (0.7-2.5 μm). Only when h and w vary proportional to R do we conclude that IDS works better for smaller particles. How difficult might it be to adapt to smaller dimensions? We do not think that the constraints imposed by very shallow channels (~1 μm) on material selection and fabrication are likely to be prohibitive. It *is* likely, however, that our operating protocols would have to be substantially revised or extended. Some of the new challenges we would face include the greater importance of surface treatments (e.g. to prevent non-specific binding) and investigation of non-pressure-driven means of generating flow (e.g. electroosmosis).

6.6 Contributions

We have created a first-generation device for iso-dielectric separation, demonstrating the ability to control particles' positions using a conductivity gradient, as well as perform some simple separations. We have developed models for the device's operation which are reasonably predictive, and which define the limitations of our architecture. We have also characterized a battery of test particle for use in the device, and developed protocols for using these measurements to plan experiments in which we manipulate or separate these particles in our device.

More generally, we have demonstrated that it is possible to create a device in which spatially varying electric fields and conductivity gradients are superimposed without the coupling between these fields and media gradients overwhelming the intended purpose of the device. Viewing this as the central challenge of IDS, we hope to further develop the architecture discussed in this thesis as well as new architectures, better suited to a wide range of applications.

Iso-dielectric separation is a fundamentally new way to separate particles, which enables continuous, real-time separation of heterogeneous populations into, in theory, arbitrarily many

subpopulations. Because IDS exploits differences in electrical properties, it is capable of separating cells with widely varying phenotypes generically, whereas other methods (such as FACS or chromatography) require the development of a new assay for each unique phenotype of interest. We view the work presented in this thesis as a first demonstration and validation of this new way of performing separations.

Appendix: Fabrication Process Flow

Starting Materials:

- 150-mm-diameter, 762-μm-thick Pyrex wafers (Bullen Ultrasonics, Eaton, OH)
- 150-mm-diameter, 650-μm-thick Silicon wafers (WaferNet, Inc., San Jose, CA)

Step	Description	Machine (TRL)	Parameters
Electrode Pattern, on 6" Pyrex wafer			
1	Piranha clean	Acid hood	
2	Dehydration bake	HMDS oven	120°C, 30 min
3	HMDS	HMDS	Recipe 4
4	Photoresist coat	coater	AZ 5214E image reversal photoresist, 3000 rpm final speed
5	Prebake	pre-bake oven	90°C, 30 min
6	UV expose	EV1	Mask 1, 2.3 sec, hard contact
7	Post-expose bake	post-bake oven	95°C, 30 min
8	UV expose	EV1	Flood (60 sec)
9	Develop, rinse and spin dry	photo-wet-r	AZ 422 developer
10	Metal evaporation	e-beam	100Å Ti, 2000Å Au
11	Liftoff metal	solvent-Au	
12	Protective resist coat	coater	AZ 5214E, 500 rpm final speed
13	Bake	post-bake oven	95°C, 45 min
14	Dice wafer	Die saw	

Microfluidic Channel Pattern, on 6" Silicon wafer			
1	Dehydration bake	hotplate	200°C, 30min
2	SU-8 Spin	SU8-spinner	SU-8 2015 (20 μm thickness): Dispense ~6ml SU-8 (1ml per inch diameter) Ramp to 500 rpm at 100 rpm/sec accel and hold for 5-10 seconds Ramp to 2250 rpm at 300 rpm/second and hold for total of 30 seconds
3	Prebake	hotplate	Slow ramp from 60°C to 95°C, hold at 95°C for 2 min; cool to ambient
4	UV expose	EV1	Flow chamber mask, 12 sec, 30 μm separation
5	Post-expose bake	hotplate	Slow ramp from 60°C to 95°C, hold at 95°C for 2 min; cool to ambient
6	Develop	Solvent-Au	~3-5 mins soak in PM Acetate 30s spin while spraying with PMA 30s spin while spraying with IPA 30s spin dry
7	Silanize wafer	EML acid hood	Put 3-4 drops of HMDS into cup in vacuum jar. Lean wafer against wall of jar, exposing both front and back Close jar, turn on vacuum for 5-10 minutes, then turn vacuum off, let sit for some time (~30 minutes). Vent.

References

1. Stephanopoulos, G., *Metabolic fluxes and metabolic engineering.* Metab Eng, 1999. **1**(1): p. 1-11.
2. Brandl, H., et al., *Plastics from bacteria and for bacteria: poly(beta-hydroxyalkanoates) as natural, biocompatible, and biodegradable polyesters.* Adv Biochem Eng Biotechnol, 1990. **41**: p. 77-93.
3. Aldor, A.S. and J.D. Keasling, *Process design for microbial plastic factories: metabolic engineering of polyhydroxyalkanoates.* Current Opinion in Biotechnology, 2003. **14**(5): p. 475-483.
4. Pratt, G.J. and M.J.A. Smith. *The dielectric response of a commercial polyhydroxybutyrate biological polymer.* in *Sixth International Conference on Dielectric Materials, Measurements and Applications (Conf. Publ. No.363), 7-10 Sept. 1992.* 1992. Manchester, UK: IEE.
5. Foster, K.R. and H.P. Schwan, *Dielectric properties of tissues and biological materials: a critical review.* CRC Critical Reviews in Biomedical Engineering, 1989. **17**(1): p. 25-104.
6. Jones, T.B., *Electromechanics of Particles.* 1995, New York: Cambridge University Press.
7. Voldman, J., et al., *A Microfabrication-Based Dynamic Array Cytometer.* Analytical Chemistry, 2002. **74**(16): p. 3984-3990.
8. Rosenthal, A.D. and J. Voldman, *Dielectrophoretic Traps for Single-Particle Patterning.* Biophys. J., in press, 2005.
9. Voldman, J., et al., *Design and analysis of extruded quadrupolar dielectrophoretic traps.* Journal of Electrostatics, 2003. **57**(1): p. 69-90.
10. Pethig, R., *Dielectrophoresis: Using inhomogeneous AC electrical fields to separate and manipulate cells.* Critical Reviews in Biotechnology, 1996. **16**(4): p. 331-348.
11. Gascoyne, P.R.C., X.B. Wang, and J. Vykoukal. *A microfluidic device combining dielectrophoresis and field flow fractionation for partical and cell discrimination.* in *Solid-State Sensor and Actuator Workshop.* 1998. Hilton Head Island, South Carolina: Transducers Research Foundation, Inc.
12. Khanna, S. and A.K. Srivastava, *Recent advances in microbial polyhydroxyalkanoates.* Process Biochemistry, 2005. **40**(2): p. 607-619.
13. Herzenberg, L.A. and R.G. Sweet, *Fluorescence-activated cell sorting.* Scientific American, 1976(234): p. 108-117.
14. O'Farrell, P.H., *Separation Techniques Based on the Opposition of 2 Counteracting Forces to Produce a Dynamic Equilibrium.* Science, 1985. **227**(4694): p. 1586-1589.
15. Brakke, M.K., *Density-gradient centrifugation.* Methods in Virology, 1967. **2**: p. 93-118.
16. Huang, Y., et al., *Introducing dielectrophoresis as a new force field for field-flow fractionation.* Biophysical Journal, 1997. **73**(2): p. 1118-29.
17. Baygents, J.C. and F. Baldessari, *Electrohydrodynamic instability in a thin fluid layer with an electrical conductivity gradient.* Physics of Fluids, 1998. **10**(1): p. 301-311.
18. Hoburg, J.F. and J.R. Melcher, *Electrohydrodynamic Mixing and Instability Induced by Colinear Fields and Conductivity Gradients.* Physics of Fluids, 1977. **20**(6): p. 903-911.

19. Santiago, J.G., *Instability of electrokinetic microchannel flows with conductivity gradients.* Physics of Fluids, 2004. **16**(6): p. 1922-35.
20. Cummings, E.B. and A.K. Singh, *Dielectrophoresis in microchips containing arrays of insulating posts: theoretical and experimental results.* Analytical Chemistry, 2003. **75**(18): p. 4724-4731.
21. Deen, W.M., *Analysis of Transport Phenomena.* Topics in Chemical Engineering, ed. K.E. Gubbins. 1998, New York: Oxford University Press.
22. Kamholz, A.E., et al., *Quantitative Analysis of Molecular Interaction in a Microfluidic Channel: The T-Sensor.* Analytical Chemistry, 1999. **71**(23): p. 5340-5347.
23. Weidman, J.A.C. and S.C. Reddy, *A MATLAB Differentiation Matrix Suite.* ACM Transactions on Mathematical Software, 2000. **26**(4): p. 465-519.
24. Kreyszig, E., *Advanced Engineering Mathematics.* 8 ed. 1999, New York: John Wiley & Sons, Inc.
25. Albrecht, D.R., R.L. Sah, and S.N. Bhatia, *Geometric and Material Determinants of Patterning Efficiency by Dielectrophoresis.* Biophys. J., 2004. **87**(4): p. 2131-2147.
26. Voldman, J., *A Microfabricated Dielectrophoretic Trapping Array for Cell-based Biological Assays*, in *EECS*. 2002, Massachusetts Institute of Technology: Cambridge. p. 152.
27. Jones, T.B. and M. Washizu, *Multipolar dielectrophoretic and electrorotation theory.* Journal of Electrostatics, 1996. **37**: p. 121-134.
28. Ganatos, P., R. Pfeffer, and S. Weinbaum, *A strong interaction theory for the creeping motion of a sphere between plane parallel boundaries. Part 2. Parallel motion.* Journal of Fluid Mechanics, 1980. **99**: p. 755-783.
29. Muller, R., *A Microfabricated Dielectrophoretic Micro-organism Concentrator*, in *EECS*. 2004, Massachusetts Institute of Technology: Cambridge.
30. Green, N.G., A. Ramos, and H. Morgan, *AC electrokinetics: a survey of sub-micrometre particle dynamics.* Journal of Physics D-Applied Physics, 2000. **33**(6): p. 632-641.
31. Melcher, J.R., *Continuum electromechanics.* 1981, Cambridge, Mass.: MIT Press. 618 in various pagings.
32. Gadish, N., *A Combined Microfluidic/Dielectrophoretic Microorganism Concentrator*, in *EECS*. 2005, Massachusetts Institute of Technology: Cambridge.
33. Senturia, S.D., *Microsystem Design.* 2001, Boston: Kluwer Academic Publishers.
34. Xia, Y. and G.M. Whitesides, *Soft Lithography.* Annual Review of Materials Science, 1998. **28**: p. 153-184.
35. Arnold, W.M., *Surface Conductance and Other Properties of Latex Particles Measured by Electrorotation.* Journal of Physical Chemistry, 1987. **91**(19): p. 5093 - 5098.
36. Maier, H., *Electroroatation of Colloidal Particles and Cells Depends on Surface Charge.* Biophys. J., 1997. **73**: p. 1617-1626.
37. Seifert, U., *Configurations of fluid membranes and vesicles.* Advances in Physics, 1997. **46**(1): p. 13-137.
38. Langer, R., *New methods of drug delivery.* Science, 1990. **249**(4976): p. 1527-1533.
39. Angelova, M.I. and D.S. Dimitrov, *Liposome Electroformation.* Faraday Discuss. Chem. Soc., 1986. **81**: p. 303-312.
40. Markx, G.H., M.S. Talary, and R. Pethig, *Separation of viable and non-viable yeast using dielectrophoresis.* Journal of Biotechnology, 1994. **32**(1): p. 29-37.

41. Huang, Y., et al., *Differences in the AC electrodynamics of viable and non-viable yeast cells deteremined through combined dielectrophoresis and electrorotation studies.* Phys. Med. Biol., 1992. **37**(7): p. 1499-1517.
42. van der Pauw, L.J., *A method of measuring specific resistivity and Hall effect of discs of arbitrary shape.* Philips Res. Repts., 1958. **13**: p. 1-9.
43. Inoue, S., *Video microscopy: the fundamentals.* 1997, New York: Plenum Press.
44. Turner Designs Application Notes, *Fluorescein.* 2006: Sunnyvale, CA.
45. Ajdari, A., *Electrokinetic "ratchet" pumps for microfluidics.* Applied Physics A: Materials Science and Processing, 2002. **75**(2): p. 271-274.
46. Randall, G.C. and P.S. Doyle, *Permeation-driven flow in poly(dimethylsiloxane) microfluidic devices.* Proc Natl Acad Sci U S A, 2005. **102**(31): p. 10813-10818.
47. Hu, X., et al., *Marker-specific sorting of rare cells using dielectrophoresis.* Proc Natl Acad Sci U S A, 2005. **102**(44): p. 15757-15761.